DESIGN AND COMPARATIVE MATERIAL ANALYSIS OF A CAPACITIVE TYPE PRESSURE SENSOR FOR MEASUREMENT OF KNEE PRESSURE DISTRIBUTION OF RODENTS

by

Al Maqsudur Rashid

A thesis submitted in partial fulfillment
of the requirements for the degree

of

Master of Science

in

Mechanical Engineering

MONTANA STATE UNIVERSITY
Bozeman, Montana

December, 2013

APPROVAL

of a thesis submitted by

Al Maqsudur Rashid

This thesis has been read by each member of the thesis committee and has been found to be satisfactory regarding content, English usage, format, citation, bibliographic style, and consistency and is ready for submission to The Graduate School.

Dr. Ronald June

Approved for the Department of Mechanical and Industrial Engineering

Dr. Christopher Jenkins

Approved for The Graduate School

Dr. Karlene A. Hoo

ACKNOWLEDGEMENTS

I would like to express heartfelt gratitude to my supervisor and thesis committee chair Dr. Ron June for supporting me from the very beginning of his project with many encouragements and ideas and suggesting me a proper path to finish my degree. It was a wonderful learning experience for me during the work presented here with proper guidance and mentoring from him. Without his patience I wouldn't have finish this write-up any sooner. Then I would like to give a special thanks to my former supervisor Dr. Ahsan Mian for introducing me to MEMS at MSU and later presenting me this work which eventually gave the foundation of my thesis. I am thankful to Tom Rose who allowed me to cite his experimental data and updating me with experimental measurements from time to time during the ongoing project upon which this work was built on. I am grateful to Harris Mousoulis from Purdue University with whom I have shared and exchanged knowledge about various MEMS clean room process and steps. Also thanks to Donny Zignego for showing me quick tips on how to format this report easily. Lastly all of these would have never been possible if I wouldn’t have received support from my parents thousands mile away from here praying for me all the time.

TABLE OF CONTENTS

TABLE OF CONTENTS - CONTINUED

LIST OF TABLES

LIST OF TABLES - CONTINUED

LIST OF FIGURES

LIST OF FIGURES - CONTINUED

LIST OF FIGURES - CONTINUED

LIST OF FIGURES - CONTINUED

LIST OF FIGURES - CONTINUED

LIST OF FIGURES - CONTINUED

Figure Page

LIST OF FIGURES - CONTINUED

LIST OF FIGURES - CONTINUED

ABSTRACT

Rodents are commonly used in biomedical and biomechanical research because of their genetic and biological characteristics closely resemble those of humans. Rodents have similar knee joint structures to human beings, and are commonly used as models for human osteoarthritis. Biomechanical factors influencing the patterns of pressure distribution within the joint are very important in the pathogenesis of osteoarthritis at the knee joints. The pattern of pressure distribution of the femoral condyles of weight bearing knee joints is therefore of great interest.

A flexible and biocompatible Polymer based Micro-Electromechanical (MEMS) pressure sensor was designed for this purpose with capacitive sensor array embedded inside the structure. The sensor structure comprises of a 4x16 arrays of sensors embedded inside the Polymer structure with air gaps and insulation layers to provide a suitable dielectric medium to achieve better capacitive sensitivity. A three dimensional model of the sensor was created using *ANSYS Workbench Design Modeler* and analyzed with two different types of polymers and metals as potential structural materials of the sensor.

A suitable clean-room fabrication process was proposed and analyzed for the sensor and corresponding mask designs were created with a CAD (Computer Aided Design) program. Residual stresses due to mismatch of thermal coefficient of expansion were calculated along with proposing a schematic readout circuitry for high gain and signal to noise ratio and failure analysis of the sensor.

INTRODUCTION TO MEMS BASED PRESSURE SENSOR

Mems Pressure Sensor Overview

Micro-electro mechanical systems (MEMS) is the technology of very small devices which merges at the nano-scale into nano-electromechanical systems (NEMS) and nanotechnology (1). MEMS are widely used to miniaturize sensitive devices like pressure transducers, accelerometers, strain gauge etc. for specialized applications. Over the past few years there has been increased interest in fabricating miniature absolute pressure transducers using silicon integrated circuit technologies with the expectation that silicon technology can reduce size, improve performance and minimize cost (1) . Several types of MEMS sensors have been studied to detect pressure including capacitive, piezoresistive, resonant and fiber optic (2). Among them capacitive pressure sensors are one of the most widely studied devices for various types of applications such as biomedical, automotive and aerospace etc.(2). MEMS capacitive sensors provide high pressure sensitivity, low noise, low power consumption and low temperature sensitivity (2). The critical constrains for MEMS capacitive sensors are nonlinearity for large displacement and the low signal level; therefore a parallel plate structure with small displacement (within the pressure range of interest) and noise suppression would be an optimal solution (2) .

There are generally two types of pressure sensors which function mainly on the principle of mechanical deformation and stresses of thin diaphragms induced by the input pressure (5). The two types are absolute and gage pressure sensors (5). The absolute pressure (absolute pressure is a summation of gauge pressure and atmospheric pressure) sensor has an evacuated cavity on one side of the diaphragm and the measured pressure is the “absolute “value with respect to vacuum as the reference pressure (5). The pressure is applied on the diaphragm by either back-side or front-side pressurization (5). The sensing element is usually made of thin silicon die and a cavity is created from one side of the die by means of a microfabrication process (5). Figure 1 shows the cross section of a typical pressure sensor diaphragm.

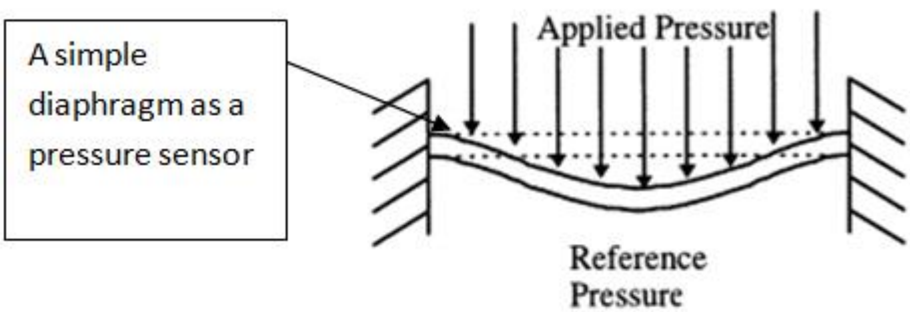

Figure 1: Cross section of a typical sensor Diaphragm and the Dotted line represent un-deflected state. Image modified from (5)

The shape of the diaphragm is arbitrary but generally takes the form of a square or circle. For the case of a both end fixed circular plate with small deflections (i.e. less than half of the diaphragm thickness) the deflection is given by equation found in (6):

$$w(r) = \frac{P \cdot a^4}{64 \cdot D} \cdot \left[1 - \left(\frac{r}{a}\right)^2\right]^2 \qquad \text{Equation 1}$$

Where w,r,a and P are the deflection, radial distance from the center of the diaphragm, diaphragm radius and applied pressure respectively. D is the flexural rigidity which is given as in (6):

$$D = \frac{E \cdot h^3}{12(1 - v^2)} \qquad \text{Equation 2}$$

Here E, h and ν are young's modulus, thickness and Poisson's ratio of the diaphragm respectively. From equation 1 we can clearly see that the amount of deflection is directly proportional to the applied pressure. So in ideal case it is advantageous to use a pressure system which is linear due to simplicity of the calibration and measurement (6). The deformation of the diaphragm is later transduced into electrical signals by different transduction methods and both are later packaged into a robust casing made of metal, ceramic or polymer with proper passivation layer (5).

Piezoresistive and Capacitive MEMS Pressure Sensor

Certain crystals in nature can generate electric voltage upon deformation due to applied force and this phenomenon is known as piezoelectric effect (5). Piezoresistance is defined as the change in electrical resistance with applied stress fields (5). The discovery of piezoresistivity enabled production of semiconductor based sensors. In this type of pressure sensors there are piezoresistors mounted on or in a diaphragm (6). Silicon is one of the widely used piezoresistors in micro sensors and actuators. Doping the boron to silicon lattice produce p-type silicon crystal and doping with arsenic or phosphorus results in n-type silicon and both p-type/n-type silicon exhibit excellent piezoresistive effect (5). The piezoresistors convert the stress induced in the silicon diaphragm by the externally applied pressure into change in electrical resistance which in turns converted into voltage output by whetstone bridge circuit (5) shown in Equation 3.

The basic operating principle of this type of sensor is that piezoresistors are deposited or diffused on top of the membrane and the resistors are usually connected to a whetstone bridge configuration to compensate for temperature effect (7).Those piezoresistors are essentially miniaturized semiconductor strain gauges which results in change of electrical resistance induced by mechanically applied pressure (5).

Figure 2 demonstrates a typical piezoresistive pressure sensor assembly where four piezoresistors (R1, R2, R3 and R4) are implanted beneath the surface of the silicon die. The resistors R1 and R3 are subjected to a stress field by the applied pressure which results in an increase of electrical resistance in these resistors (5). On the other hand the resistors R2 and R4 experience a decrease in their electrical resistance because of their orientation.

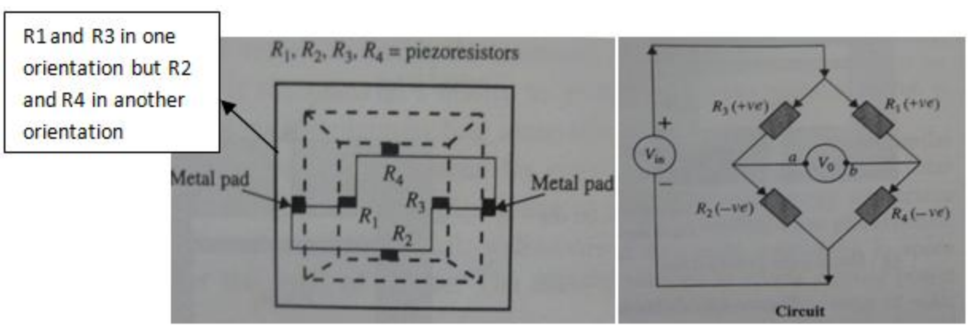

Figure 2: a) Typical Piezoresistive Sensor Assembly b) Wheatstone bridge; Image modified from (5)

The output voltage Vo and the input voltage Vin to the whetstone bridge are related by the following equation and the changes of resistance as induced from applied pressure is measured using the equation found in (5) which is:

$$V_o = V_{in} \cdot \left(\frac{R_1}{R_1 + R_4} - \frac{R_3}{R_2 + R_3}\right) \qquad \text{Equation 3}$$

The main advantage of piezoresistive pressure sensors are the simple fabrication process, high linearity and the output signal is conveniently available as a voltage (5). However these sensors have very large temperature sensitivity and drift (5). Because of the low sensitivity these sensors are not suitable for very low pressure differences (5).

There is another type of micro-pressure sensor that utilizes the change of capacitance measurements. Two electrodes of thin metal films are deposited on bottom and top of the diaphragm and parallel to each other (5). Whenever pressure is applied on the diaphragm the gap between the two electrodes will narrow which leads to change of capacitance across the electrodes (5). The simplest structure of a capacitive sensor can be described by two flat parallel plates with area A and distance d as shown in Figure 3

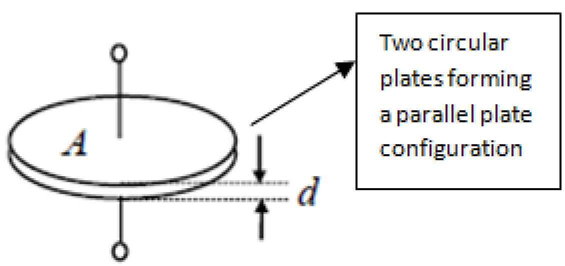

Figure 3: A Parallel plate Capacitor, Image modified from (7)

The capacitance value C in a parallel –plate capacitor can be related with the gap distance d by the following equation:

$$C = \varepsilon_o \cdot \varepsilon_r \cdot \frac{A}{d} \qquad \text{Equation 4}$$

Where εr is the relative permittivity of the dielectric medium, ε_0 is the permittivity in the vacuum where $\varepsilon_0 = 8.854x10^{-12}$ (Farad/meter) and A is the overlapping area between the parallel plates (5). The capacitance value increases with the increase in either effective area A or permittivity of the dielectric medium εr and decreases as the gap distance increases. Based on the parameters on the above equation a capacitive sensor can be of 3 types: a) ε-type where the capacitive sensors has a fixed value of A and d but the dielectric properties are variable; b) D-type where the sensors has a fixed value of A and ε but the distance is variable and c) A-type where the sensors has a fixed values of d and ε but the area is variable.Since relative permittivity is not a fundamental variable and can be temperature dependent, inhomogeneous or anisotropic for certain materials ε-type sensors are generally not common (7). The D-type capacitive sensors are very effective for small displacement measurements and most common type of capacitive micro-pressure sensors usually used. However non-linearity in the measurement might be caused by fringe fields or parasitic capacitance. The accuracy of A-type sensors highly depends on the mechanical accuracy, flatness of the electrode surface, obliqueness, deformation, frayed edges and gaps (12).

Capacitive based sensor mechanisms are inherently less sensitive to the variations in the operating temperature and very low power consumption can be obtained from these devices. However the capacitance to be measured is usually very small range so an effective readout circuit interface needs to be constructed which can be either integrated in the sensor die or at least to be positioned very close to the sensor chip (7).

Motivation

Osteoarthritis (OA) also known as degenerative arthritis is a group of mechanical abnormalities involving degradation of joints including articular cartilage, limited intraarticular inflammation with synovitis and subchondral bone (3). Some of the Major symptoms of this disease are joint pain, stiffness, functional impairment, loss of mobility and sometimes inflammation (3). A variety of other causes like developmental, hereditary, metabolic disorders and mechanical deficits may initiate processes leading to loss of cartilage. The integrity and quality of cartilage cell covering the knee joint plays an important role in the development of Osteoarthritis.

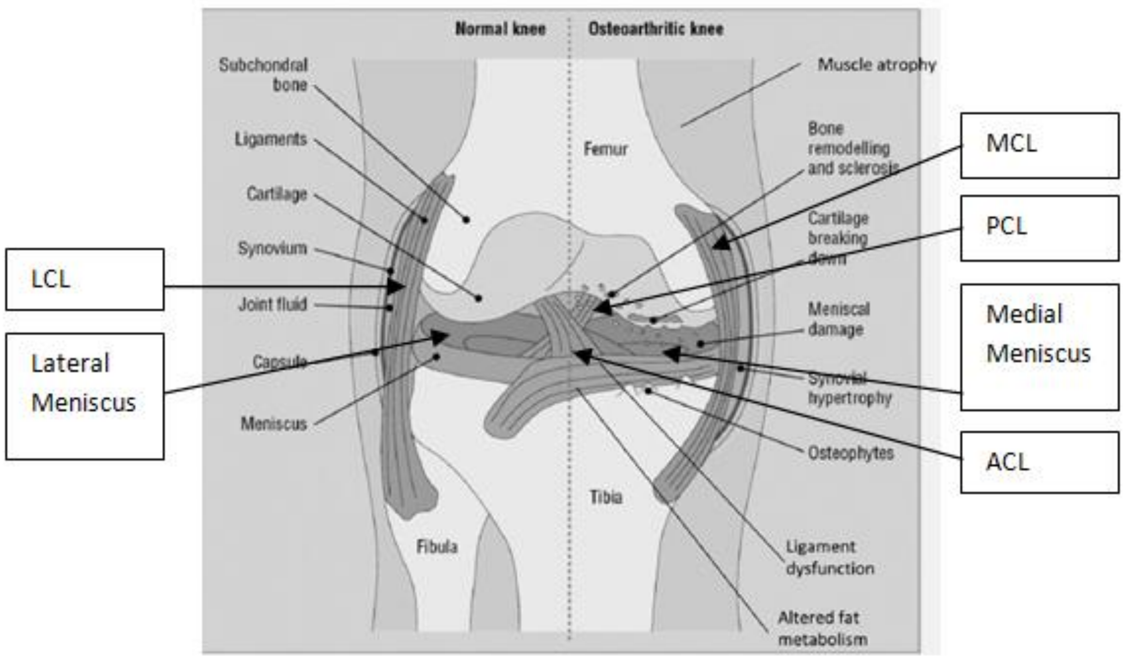

Figure 4 : Schematic diagram of the knee joint showing synovial joint tissues affected by OA; image modified from (8)

Biomechanical factors that influence the patterns of pressure distribution within the joint are very important in the pathogenesis of Osteoarthritis. There are two fundamental mechanisms that are related to the risk factors for development of OA which are adverse effects of “abnormal” loading on normal cartilage or of “normal” loading on abnormal cartilage (3). One of the main reasons that contribute to the “abnormal” state of articular cartilage is “Aging”. Those persons who are vulnerable to development of OA, some local mechanical factors such as abnormal joint congruity, joint misalignment, muscle weakness, meniscal damage, ligament rupture etc. can aggravate the possibility of OA progression (8). Also genetic factors can cause disruption of chondrocyte and influence the composition and structure of the cartilage leading to abnormal biomechanics (3). Conditions that produce increased load transfer and/or altered patterns of load distribution can enhance the initiation and progression of OA (3).

Articular cartilage is subjected to a range of static and dynamic mechanical loading in human knee joints (9). The ability of cartilage to withstand these different types of compressive, tensile and shear loads depends on the composition and structural integrity of its extracellular matrix (ECM) (9). Articular cartilage provides lubrication and load bearing functionality during motion of synovial joints (9). Mechanical stresses play an important role in the pathogenesis and progression of Osteoarthritis (10). Structural failure due to mechanical stresses in OA can involve all tissues of the joint, including the capsule, synovial membrane and subchondral bone, ligaments, fibrocartilaginous menisci in joints such as knee and the articular cartilage (10).

Abnormal mechanical stress can cause the structural failure of articular cartilage in OA, damaging initially normal tissues from the failure of pathologically impaired articular cartilage (10). Articular cartilage injuries might occur due to either traumatic mechanical destruction or progressive mechanical degeneration. As the loss of articular cartilage lining continues the bone underneath becomes unprotected from mechanical wear and tear and begins to break down which will eventually lead to osteoarthritis. The pattern of contact pressure distribution of the weight bearing knee joints therefore is of great interest.

Osteoarthritis and Contact Pressure

Recent studies have found that contact stress is a potential indicator of subsequent symptomatic osteoarthritis development in the knee joint. The results of the study in (11) indicated that higher tibiofemoral contact stress increased the risk of both worsening of cartilage morphology and BMLs (Bone marrow lesions). These studies were consistent with the hypothesis that excessive loading within tibiofemoral joint compartments longitudinally contributes to pathology articular cartilage and subchondral bone (11). It was evident from the studies done in (11) that contact stress estimation can predict the mechanical degradation of a knee whether it is a normal or Osteoarthritis affected knee. Contact stress has previously been shown to be efficient and accurate means of predicting the risk of development of incident symptomatic knee Osteoarthritis which may also be useful for predicting anatomic degradation (11).

Estimation of contact pressure may also guide development of specific therapies to positively change the direction of knee OA and guide decisions regarding which patients might benefit from surgery or prescribing a surgical or non surgical therapy therefore planning to optimize reduction of contact stress (11).

Role of Knee Loading in Osteoarthritis

Joint alignment influences to the distribution of load on the articular cartilage and other tissues of weight bearing joints. The external knee adduction moment is generated while walking and this moment pushes the knee into the varus which results in a compression of the medial joint compartment (10). It has been found that the magnitude of the baseline adduction moment is a good indicator of progression of medial compartment knee osteoarthritis (10).

In order to understand knee contact pressure mechanism and its relation to osteoarthritis we need to study the interior of the knee joints. The anatomy of the knee describes as it has 3 bones which are Tibia, femur and patella as shown in Figure 4. There are three compartments which are medial, lateral and patellofemoral (Figure 3) and four ligaments which are MCL, LCL, ACL and PCL (Medial, lateral, anterior and posterior cruciate ligaments). Also there are 2 menisci and articular cartilages as shown in (Figure 4).

For knee osteoarthritis the most relevant and widely studied load is the external knee adduction moment generated by ground reaction force vector passing medial to the joint center as shown in Figure 5. This adduction moment forces the knee laterally into varus (When a knee is perfectly aligned it has its load bearing axis on particular line that goes through middle of the leg, hip, knee and ankle, but when the knee is not aligned perfectly it is known as varus (bow legged) or valgus alignment (knock-kneed)) resulting

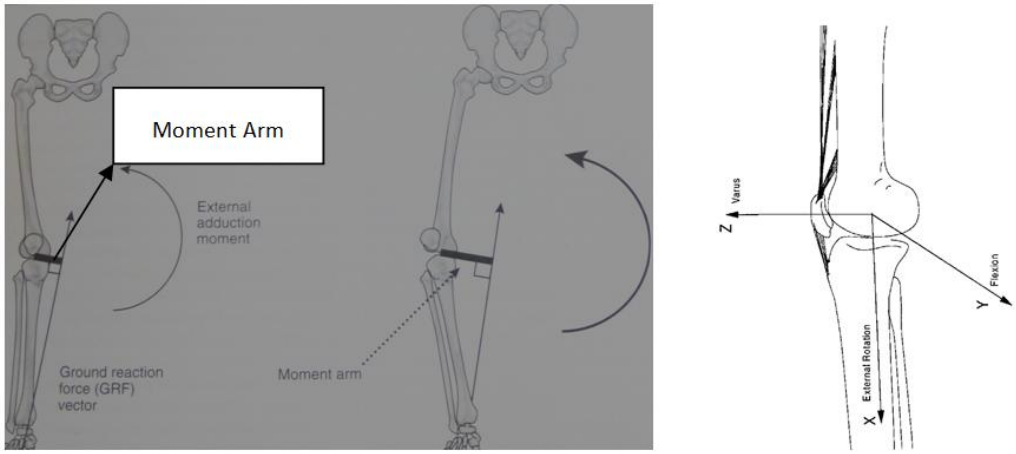

Figure 5: a) Ground Reaction force vector (GRF) which is at a distance from rotation center of the knee joint producing an external adduction moment of force with knee co-ordinate system (Medial view of Right knee) where The x-, y-, and z-axes correspond to the tibial rotation, flexion extension, and varus-valgus axes, respectively; image modified from (15)

in compression of the medial joint compartment causing the stretching of the lateral structure (10). The adduction moment has a great influence on the load distribution between medial and lateral plateau (10). The higher the adduction moment the greater the load on the medial plateau relative to the lateral plateau and adduction moment is higher in knee with osteoarthritis than in a normal knee (10).

Knee adduction moment could be measured during gait with laboratory based measurement system or laboratory free settings like Ambulatory movement analysis systems including instrumented force shoes (IFS), inertial and magnetic measurement systems (IMMS) etc.(43)The mechanical alignment of the lower limb plays a vital role in the distribution of load across the medial and lateral knee joint compartments. Sometimes there could be preexisting mal-alignment that can contribute to the development of OA or the mal-alignment could be a result of osteoarthritis process due to cartilage loss, bonny attrition and meniscal damage (10). In a neutral knee position the ground reaction force vector shown in Figure 5 slightly passes medial to the knee joint center (10). In a varus position the ground force vector is medially more displaced to the knee joint center thereby increases the knee adduction moment and compressive load across the medial compartment (10). In a valgus knee the ground reaction force vector passes more laterally with increasing valgus thereby increasing the load across the lateral compartment (10). Varus mal-alignment is common in people with medial tibiofemoral joint OA (10).

Table 1: Comparison of Contact stress between control knees and Symptomatic OA case Knees found in (4)

Variable	Control Knees (Mean±SD, N=30)	Incident Symptomatic OA Case Knees (Mean±SD, N=30)	p-Value
Age	65.5±7.8	67.8±7.5	0.210
Sex (% Women)	73%	87%	0.197
Weight (kg)	79.7±15.0	79.5±12.5	0.198
Height (cm)	166.5±7.9	163.6±9.5	0.204
BMI (kg/m^2)	28.6±4.4	29.9±5.3	0.953
Knee Height (cm)	52.2±3.0	51.7±3.3	0.531
Contact Area (mm^2)	1122±228	1220±255	0.076
Maximum Contact Stress (MPa)	3.38±0.58	3.92±0.55	0.001

The maximum contact stress was 0.54 ± 0.77 MPa higher in case than in control knees ($p = 0.0007$), with a nearly equal number of knees in each group experiencing the maximum contact stress in the medial versus the lateral compartment (M/L proportion = 53.3% and 53.6% for the control and case knees, respectively).

In Summary the development of tibiofemoral OA is strongly influenced by contact geometry and loading factors that can alter the cartilage microstructure and vitality. The combination of mal-alignment and altered anatomy are most likely responsible for higher contact stress in the knees which in turn leads to OA (4).

Identifying the maximum contact stresses and distribution between a tibiofemoral OA case and control knees are extremely important for the prediction of incident and progressive knee OA. Contact stress is a stronger predictor of OA than demographic or anthropometric measures which is evident from the above Table 1.

Mouse as Experiment Model

Animal modeling of Osteoarthritis is performed inorder to controllably reproduce the scale and progression of joint damage so that opportunities to detect and modulate symptoms and disease progression can be identified and new therapies be developed (12). An ideal animal model is the one with relatively low cost and exhibits reproducible disease progression with a magnitude of effect large enough to detect differences within a short period of time and replicate human OA (12).

Although risk factors of OA were identified by various epidemiologic studies limited to age, trauma history, occupation and gender, large contributing casue of OA is accumulated mechanical stress (13). Due to rapid progress of mouse genomics and the availability of transgenic and knockout mice it is the most ideal animal model to study osteoarthritis progression and development by producing instability of joints through surgical intervention (13). These genetically modified transgenic knockout mouse will develop premature cartilage degeneration to observe the effect and prognosis of OA (14). Surgically induced models are used where the meniscus of the specimen is removed which will allow mechanical wear and degradation of the cartilage within the knee (14). These knockout mice have permitted the validation of many mechanisms associated with risk factors of OA such as biomechanical instability, injury, inflammation etc. These mouse models will develop spontaneous or accelerated OA due to altered biomechanics which might not have been possible with human as test subjects from research perspective (15).

The pressure sensor for this report was designed based on the mouse dissection data received in courtesy of the author of the work in (14). It was intended to be used for measuring contact stress distribution in the tibiofemoral joint of mouse knee in order to distinguish between a control knee cartilage contact stresses with a degenerated cartilage. Thus mouse was an ideal model to perform osteoarthritis quantification as a disease in the laboratory environment.

DESIGN AND MODELING

Array Configuration

Capacitors can be built in various ways with MEMS technologies. A distributed array of capacitors in rows and columns of a matrix configuration was chosen in order to map the pressure distribution inside knee joint. Each intersection of rows and columns constructed from conductive strips of metal layers known as Electrodes were separated by a suitable elastic dielectric medium and forms a single cell of coupling capacitor or a unit sensor. These unit cells are the core sensing elements of the pressure sensor and the higher the spatial density of the cells the higher the spatial resolution of the total sensor will be.

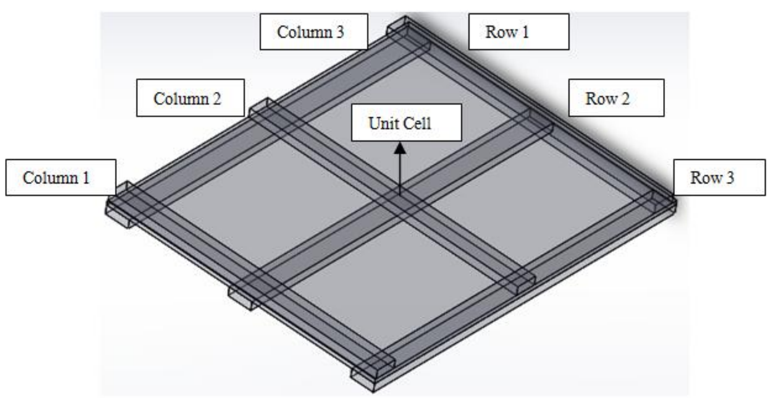

Figure 6: Row and Column configuration

The unit cell is analogous to the 'Pixel' of an electronic display monitor where higher pixels usually results in sharper and smoother images on the screen. Figure 6 displays a grid structure of rows and columns of electrodes and each intersection have formed a coupling capacitance between the electrodes. When the dielectric layer between the electrodes is squeezed due to pressure being exerted on the corresponding area of the sensor the capacitance between the two overlapping area will change.

The sensor was designed based on an array configuration and it consisted of high density capacitive cells in a grid format that will enable us to map the distribution of the pressure inside the knee joints. The distribution will be based on location wise output from each unit cell. The location of the output (capacitance or voltage change) can be traced from relative position of column and row intersection when the scanning circuit will scan the columns and rows sequentially. The values of the change of capacitance will be inserted in a computer programming code to construct a matrix whose dimension will be same as the sensor grid configuration. From there intensity of the pressure can be easily distinguished based on location to form a complete pressure map of the desired area.

Some previous works that were based on capacitive pressure sensor array could be mentioned in this regard. Hyung-Kew, Sun-Il et al. 2006(16) worked on a fexible polymer based tactile sensor which utilized a total of 16x16 of cell array made of copper electrodes embedded in PDMS (Polydimethylsiloxane) with a spatial resolution of 1mm and utlized the theory of capacitance change between the copper elctrodes separated by 12 microns gap (6 microns by a spacer creating air gaps in the middle and 6 microns by insulation layer)with an initial capacitance of a single cell being 171 femtoFarad. Their cell size and electrode size were 600 x 600 µm2 and 400 x 400 µm2 respecively.

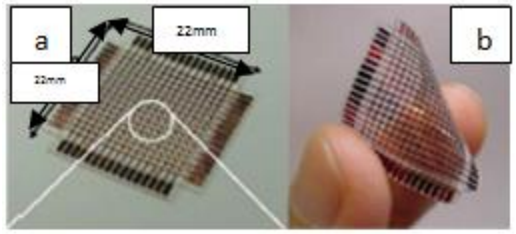

Figure 7: Work of Hyung-Kew, Sun-II et al. (16) a) The 16 x 16 arrays of capacitive cells b) Flexibility of the sensor structure due to PDMS; Photo modified from reference (16)

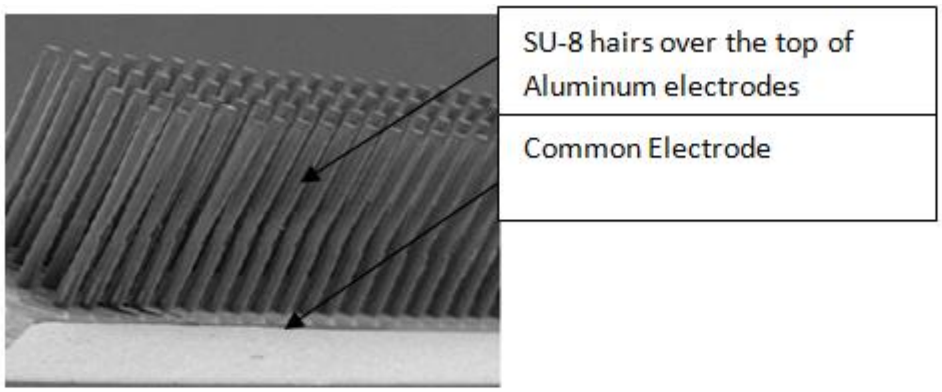

Figure 8: Work of Dagamseh, Wiegerink et al. (17); 128 SU-8 hairs on top of array of parallel plate capacitors; Photo modified from reference (17)

Dagamseh, Wiegerink et al. 2012(17) created an artificial hair sensor arrays for flow pattern observation. Their sensor was based on the capacitance changes between two electrodes deposited on top of a silicon Nitride membrane and a common underlying electrode which was the silicon substrate and implanted SU-8 hairs on top of the membrane. They used two aluminum electrodes with the SU-8 hair in the middle as upper electrodes and a conductive silicon substrate with deposited silicon nitride as bottom electrode separated by 600 nm poly-silicon which defined the capacitors gap. They connected 124 parallel hairs in this way and formed the array of capacitive sensors.

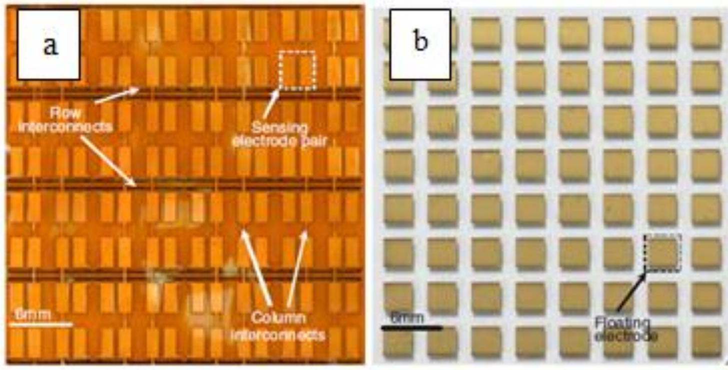

Figure 9: Work of Cheng, Huang et al. 2009 (18), capacitive sensor arrays a) Both sensing electrodes at the bottom b) The floating electrodes with no interconnections act as top electrodes

Another impressive implementation of capacitive type sensor arrays were demonstrated by the work in (18). They fabricated a tactile sensor where the sensing row and column electrodes made of copper (30 microns) were printed on a flexible printed circuit board (FPCB) with the interconnects being printed on either side of the FPCB having 100 microns thickness and the floating gold electrodes of 0.16 microns thickness were patterned in to PDMS along with chromium as the bonding substance. They improvised a solution to reduce the parasitic capacitance due to overlapping between the row and column interconnects since the row and column interconnects were printed on either side of the FPCB. In this way they were also able to avoid long and thin metal interconnects which are usually vulnerable to bending. Their flexible tactile sensor consisted of 8 x 8 arrays of sensing elements.

Pressure Sensor for Rodents: Initial Design

This pressure sensor was primarily designed to measure pressure intensity and mapping of pressure distribution inside tibia-femoral interaction of a mouse knee joint. The design was based on various dissection data on laboratory mouse (14).

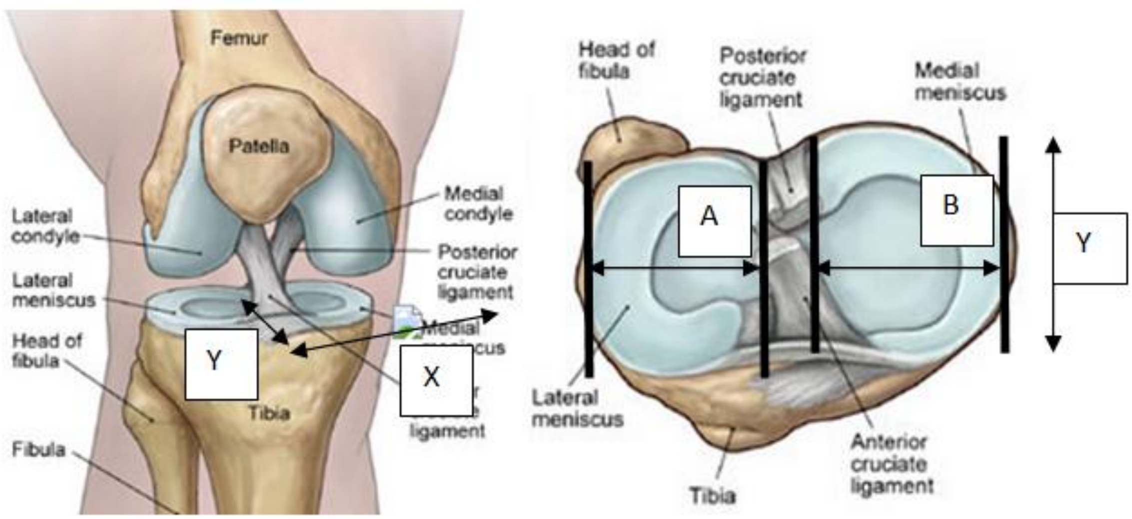

Figure 10: The Anatomy of Knee joint and view of Tibial Plateau; Image modified from Reference (19)

The average data received from experiment of various mouse dissections from (14) are tabulated below:

Table 2: Experimental Measurements of Tibial Plateau area of Mouse Knee (14)

Tibial Plateau Horizontal Span (X) mm	Tibial Plateau Vertical Span (Y) mm	Tibial Plateau, Lateral Span (A) mm	Tibial Plateau, Medial Span (B) mm	Gap Between A and B, mm	Average Between A and B, mm	Average Weight of Mouse, grams	Area of Tibial Plateau, mm^2
3.84	2.85	1.18	1.24	0.61	1.21	28.46	4.57

The Femoral condyles are going to interact with Tibial Plateau during various angles of Knee movements. So the geometric measurements of Femoral Condyle area were also included in Table 3.

Table 3: Experimental Measurements of Condyles area of Mouse Knee (14)

Condyles Horizontal Span (X), mm	Condyles Vertical Span(Y), mm	Condyles Area (2D square) mm^2
2.89	1.93	5.56

The anterior and posterior cruciate ligaments restrict movement of tibia and femur from sliding backward over each other and the lateral and medial ligaments prevents the femur from sliding side to side as well as lateral joint bending.

To perform loading on the mouse knee, the author in (26) fabricated a special type of loading apparatus where a single mouse leg could be mounted and external force could be applied along tibial axis to the femur. Based on experimental calculation of tibial area, percentage of tibiofemoral contact area, amount of preload from the loading apparatus and ranges of externally applied load the pressure range of our desired pressure sensor was established.

Here is a sample calculation of pressure in the tibiofemoral contact zone based on the above information:

From Table 2, Total area of Tibial Plateau = 4.57 mm^2= 4.57x10-6m^2

For externally applied mass of 50 gram, weight= $\frac{50}{1000}$Kg* 9.8 $\frac{m}{s^2}$= 0.49 Newton

Preload Pressure from the Loading apparatus= 34.473 kPa

For 75% contact area, Effective area of Tibial Plateau = $(0.75*4.57*10^{-6})$ m^2= $3.4275*10^{-6}$ m^2

So Total Pressure due to 75% contact = Preload Pressure+ (Weight/Effective area) = $\{34.473+(\frac{0.49}{3.4275\cdot10^{-6}}*\frac{1}{1000})\}$ kPa = 177.43 kPa

Table 4: Numerical Calculation of Total contact Pressure in the Tibial Plateau zone of Mouse Knee at different Percentage of contact (14)

	Pressure (kPa)			
Externally Applied Mass(grams)	At 25% Contact Area	At 50% Contact Area	At 75% Contact Area	At 95% Contact Area
0	34.474	34.474	34.474	34.474
5	77.381	55.927	48.776	45.765
10	120.287	77.381	63.078	57.056
15	163.194	98.834	77.381	68.348
20	206.101	120.287	91.683	79.639
25	249.008	141.741	105.985	90.930
30	291.915	163.194	120.287	102.221
35	334.821	184.648	134.590	113.513
40	377.728	206.101	148.892	124.804
45	420.635	227.554	163.194	136.095
50	463.542	249.008	177.496	147.386

Based on above information's of the anatomy and geometric measurements of mouse knee, the following sensor design specifications were developed:

The sensor should be flexible enough to conform to femoral condyle when pressed against the tibial plateau. So the sensor structural material has to be flexible enough to bend and conform to the geometry of tibial plateau. Then the sensor width should be no more than 1.21 mm according to Table 2 where we can clearly see the average horizontal span from center of tibia (average of A and B) to the edge is 1.21 mm. Finally the length of the sensor was decided to be 4 mm since the Vertical span of the tibia was 2.85 mm, it was decided to leave some space for the sensor interconnecting terminals and for the convenience of routing the wires to the end of the sensor. The sensor was designed to measure pressure distribution in either lateral or medial side of Tibial plateau so this single sensor will work on both ‘A’ or ‘B’ region (Figure 10) equally.

The working principle of the sensor was to measure the capacitive change to estimate the applied pressure. When there will be no pressure on the sensor the capacitance read out the sensor should be zero. When a pressure will be applied the distance of the dielectric layer would be reduced and the capacitance among the sensing electrodes will increase. Our pressure sensor design consisted of an upper polymer layer, upper electrodes embedded inside the upper polymer layer, an insulation layer, a lower polymer layer and lower electrodes embedded inside the lower polymer layer in general. There have been some chronological improvements and changes that were made in the sensor design based on the experimental data received from further mouse dissection results. The sensor dimensions and configurations were modified time to time according to the feedback received from the lab experimental data of mouse dissections performed by the author of the work in (14).

There were several trial designs of the pressure sensor during the ongoing effort to make a contact stress distribution measuring sensor for rodents. Each trial was later adjusted carefully considering structural point of view as well as possible complexity of readout circuitry, interconnectivity and ease of data acquisition from the sensor. Several design changes were made to the sensor following the above approach. The final trial was considered to be eligible to be fabricated as a prototype sensor but the implementation was depended on the decision of proper material selection. In this thesis an effort was also made for comparative material analysis of the sensor both from structural and sensing material perspective so that an optimum material could be recommended before moving onto actual fabrication of the sensor. A generalized micro-fabrication protocol and mask designs based on those fabrication steps were recommended at the later chapter of this work.

The following trial designs of the sensor were able to finally recommend and establish an optimum dimension suitable to be used inside the knee joint. Description and changes of each trial is given below:

First Iteration of Design

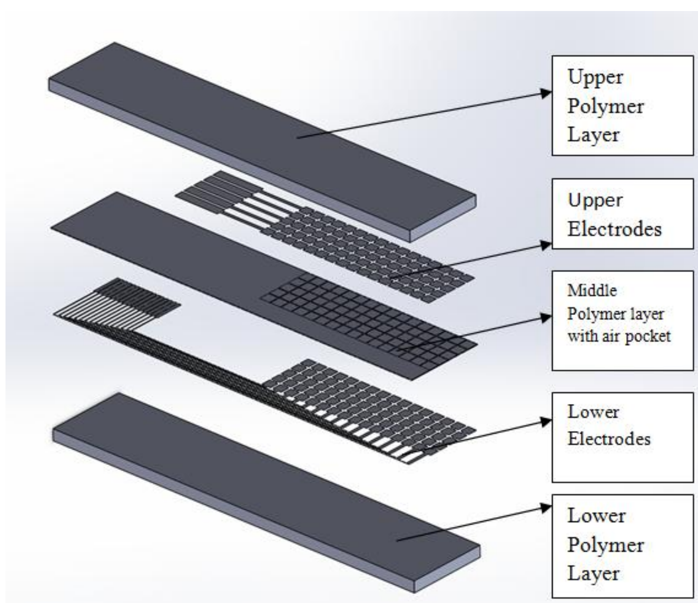

Figure 11: Exploded View of the different layers of the very first trial design of the Pressure sensor

Upper and Lower Polymer Layer

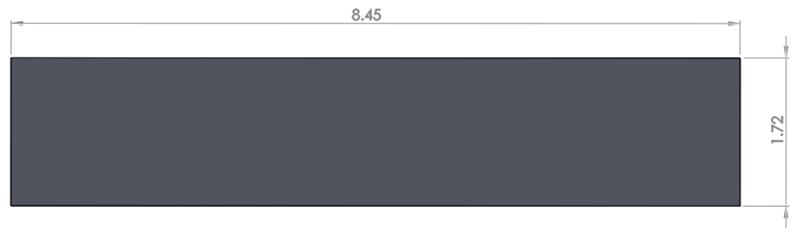

Figure 12: Upper and Lower Polymer Layer of the sensor, Units in ‘mm’

The two identical upper and lower polymer structures constituted the total sensor which encapsulated the metal electrodes inside the structure. The polymer structure would also ensure the required flexibility of the sensor as well as structural rigidity. The width of the polymer layer would define the total width of the sensor, which was estimated to be 1.72 mm according to the preliminary studies (14) who was working on the dissection of the mouse knees. Later it was found that the width that was initially estimated was not convenient enough for the insertion of the sensor inside the knee joint and readjusted later. The initial thickness of the upper and lower polymer layers were decided to be 0.24mm each.

Upper Electrodes

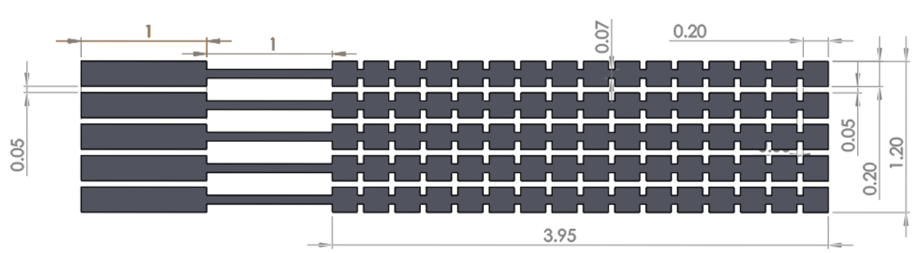

Figure 13: Upper Electrodes with dimensions; all units in mm

The sensor was designed based on an array of parallel plate capacitors running vertically and horizontally in two parallel planes but separated by a dielectric medium . There were 4 upper electrodes that would be electroplated in the silicon wafer and then polymer material would be casted on top of the electroplated electrodes with a sacrificial coating that will act as bonding and adhesive material between the polymer and the metals so that when the polymer was being peeled from the silicon wafer, the metal electrodes would still adhere with the polymer surface. Each upper electrode extended vertically straight downward to the sensing area and after the sensing area the interconnecting metal wires extended with longer aspect ratio with metal pads at the end having larger width to accommodate wire bonding/soldering electrical wires to be connected with the readout circuit later as shown in Figure 14. The dimension of each square plate was 200x200 microns and the pitch between each vertical electrode was 250 microns with 50 microns air gap both vertically and horizontally.

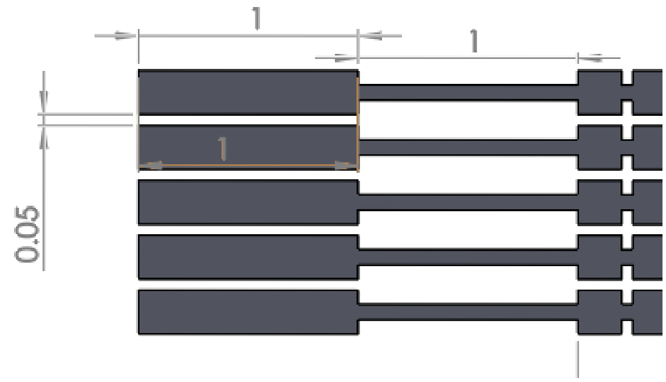

Figure 14: Interconnecting wires for Upper Electrodes; Dimensions in mm unit

<u>Lower Electrodes</u>

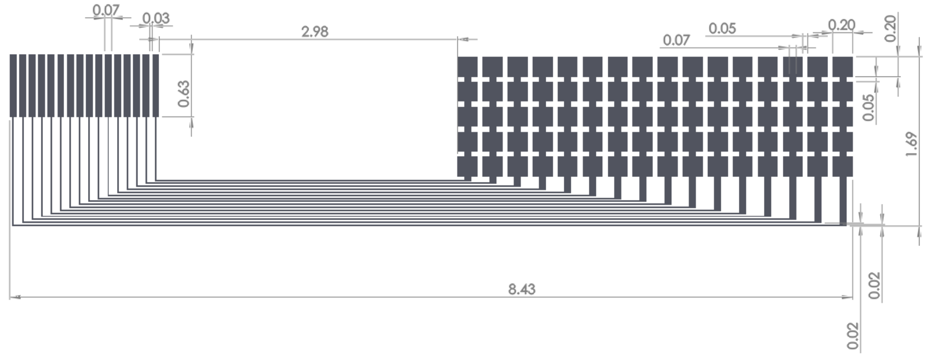

Figure 15: Lower electrodes with interconnecting wires sideways; all units in mm

The initial design contained 16 horizontal electrodes embedded in the lower polymer layer and the metal deposition process was similar to upper electrodes mentioned above by electroplating process. This array of lower electrodes produced high density metal traces with minimum trace size of 20 microns with 20 microns air gap between the high density interconnecting wires. The interconnecting wires were designed to be routed from any one side of the sensor since that area of the sensor will be buried under the gap between A and B region (Figure: 10) where least contact between tibial plateau and femoral condyles would occur.

Due to space limitation of 1.72 mm width the routing of the interconnecting terminals were very closely populated within spatial constraints. The square electrodes had exactly the same dimension as the upper electrodes and the projection of the area were similar. The actual sensing area was 3.95 mm for both upper and lower electrodes and their overlapping state looked like the same as shown in figure 10 which constituted the actually sensing area of the sensor.

Thin Insulation Layer With Air Pocket

A thin insulation layer was designed to be placed in between the upper and lower electrodes which would provide a better dielectric coefficient (A composite dielectric medium of air and polymer) and prevent the electrodes coming into direct physical contact with each other. The insulation layer had a total thickness of 12 microns and it contained a 6 microns air pocket inside the structure as shown in Figure 16 and 17.

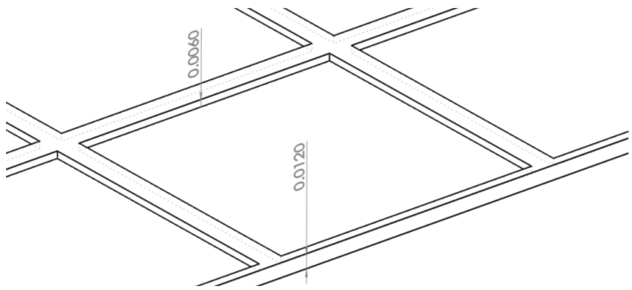

Figure 16: Insulation layer with a single Air Pocket; All units in mm

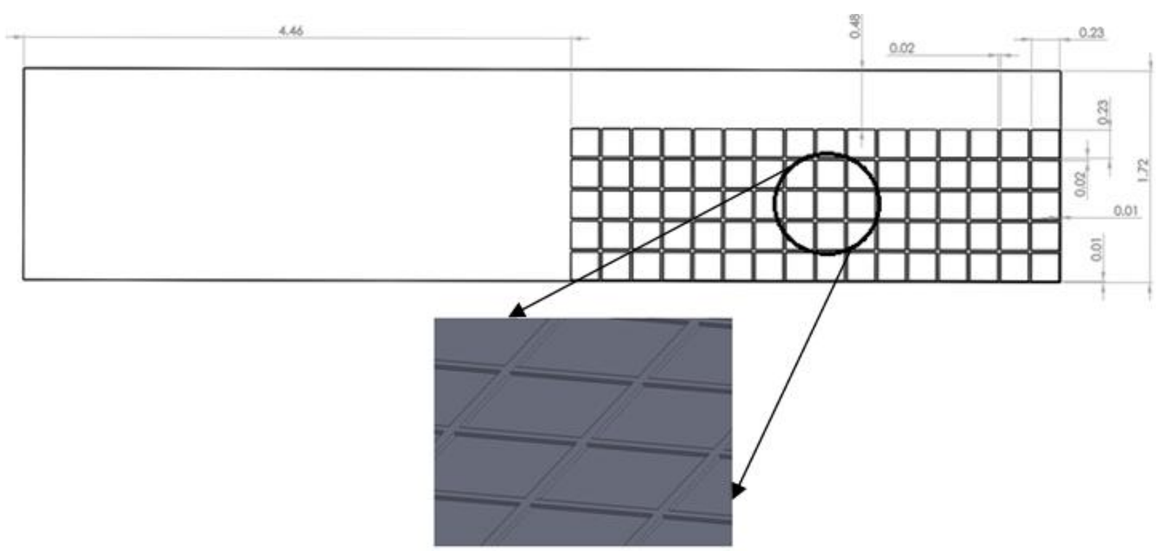

Figure 17: thin insulation polymer layer containing air pocket, zoomed out view; Units in mm

The 16 X 5 arrays of cells required 80 corresponding air pockets to be created inside the thin insulation layer of polymer. Due to gap provided by this insulation layer, electric charge will build up in the parallel plates between their projected overlapped area once a source voltage will be applied to any one row or column of electrodes.

Finally the view of upper and lower electrodes sandwiching the insulation layer with air pocket is demonstrated in Figure 18 below:

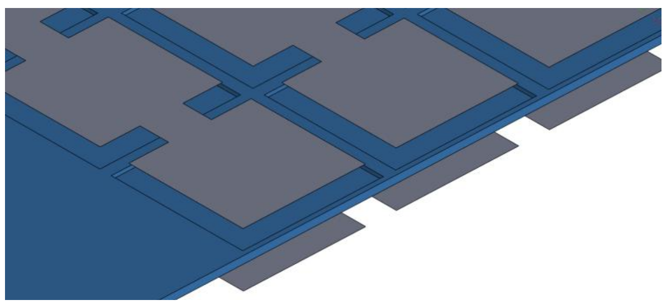

Figure 18: Upper and lower electrodes floating over insulation layer

The preliminary thickness of the upper electrodes, lower electrodes, insulation layer and the two identical polymer layers were designed as 1 micron, 1 micron, 12 microns with 6 microns air gap and 240 microns respectively. But later we adjusted our design in response to finite element analysis along with parallel plate capacitance equations to achieve an optimum thickness of the metal layers, proper polymer material selection and total thickness of the sensor as well.

Second Iteration of Design

The next design changes were solely based on the fabrication steps that were decided for the fabrication of the pressure sensor. The circuit connectivity would require more space compared to the previous design and ease of handling was another priority . The sensor dimensions were adjusted once again and a tentative final estimation was reached based on the laboratory experimental data of dissection of mouse knee's courtesy of the author in (26). The optimum dimension of the sensor part was decided to be 1.2 X 4 mm width and length respectively. Any sensor dimension beyond 1.2mm would not fit within the tibiofemoral interaction zone and the rest of the dimensions outside the knee joint interaction were flexible to choose. To allow this change of width, the total number of vertical electrodes were reduced from five to four and total number of effective capacitive cells were reduced from 80 (5X16) to 64 (4X16) in the second iteration of design. The other changes that were made in the sensor structure were the insulation layer containing the air pockets described later in this chapter.

<u>Full Sensor</u>

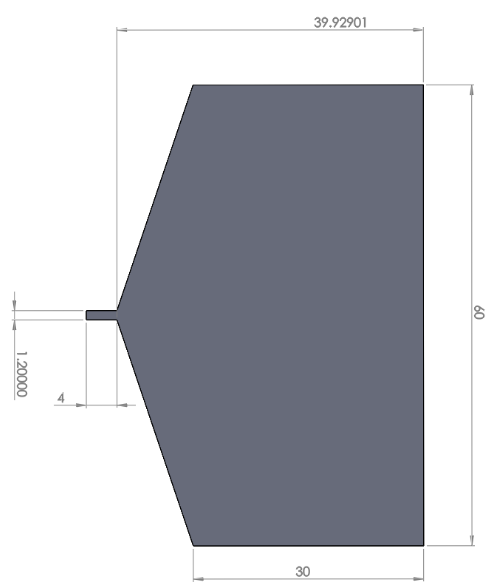

Figure 19: Full sensor design changes; All units in mm

The final optimum dimension of the sensor area containing the capacitive cells were determined to be 1.2 mm by 4 mm as shown in the Figure 19 and it was introduced since second iteration of design changes of the sensor. The dimensions were once again set on the basis of previous experimental mouse dissections results received courtesy of the author in (14). It was realized that the sensor electrical circuit connectivity would demand more space which would result in ease of handling, calibration and data collection after the completion of the sensor. As a result the lower part outside the original capacitive sensing area was determined to be 30 mm by 60mm polymer structure to house all metal wirings and connecting pads. The ratio of the length and width of the sensor outside knee joint to inside knee joint (main sensor part) was approximately 10:1 and 50:1 respectively.

Upper and Lower Polymer Layer

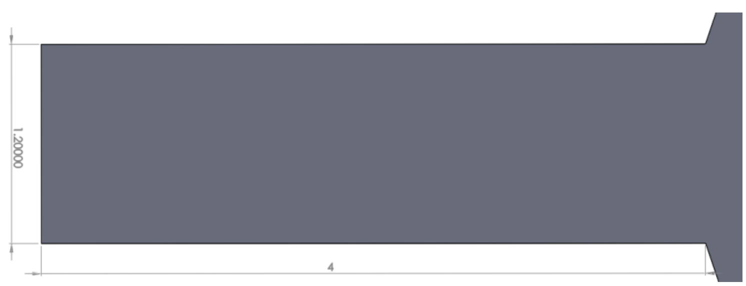

Figure 20: Original Area of the sensor; All units in mm

As shown in Figure 20, the new optimum dimension of the sensor was determined to be 1.2 mm by 4 mm since the new width would allow to provide more space for routing the side wirings of the lower electrodes as well as fit inside the knee joint more conveniently.

Upper and Lower Electrodes

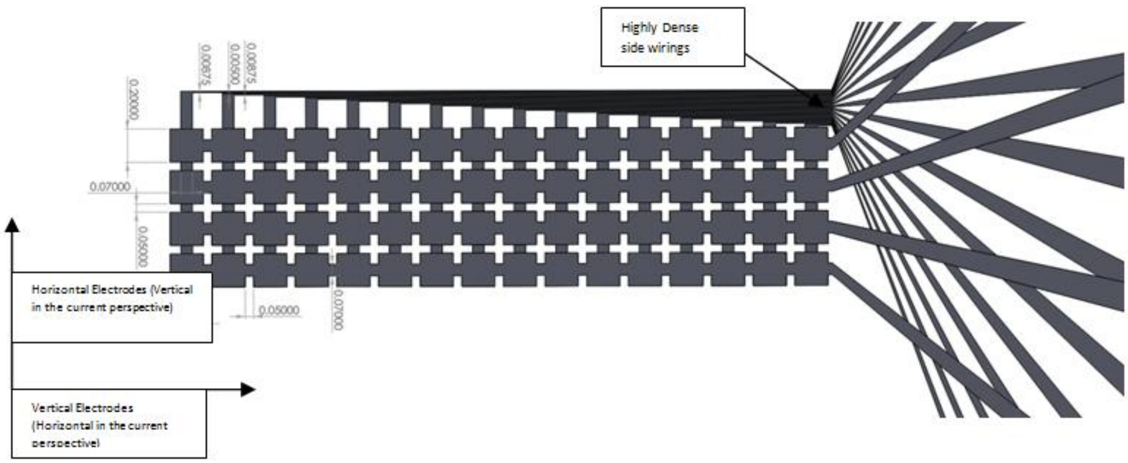

Figure 21: Upper and Lower Electrodes Side wirings: All units in mm

Dimensions of the Upper and lower electrodes, air gaps and pitch were kept exactly the same as first design except the dimensions of the side wirings and the wirings projecting from the vertical electrodes. As shown in Figure 21 and 22, the trace size in the high density side wirings of the horizontal electrodes were 8.75 microns and air gap between the side wirings were 5 microns. For vertically running upper electrodes the size of the wires was easier to solve since only four extended wires need to be accommodated in this regard. The wirings non-uniformly extended at the end of the sensor (4mm) and projected into a larger geometry with gradual increment in width of the wirings shown in Figure 21. The width of the vertical wires started with 70 microns within knee joint and extended to a final width of 1mm (1000 microns) outside of the knee joint. The initial width ratio of horizontal side wires to vertical wires was 1:8 and final width ratio was

1:1. Both upper and lower electrodes were parallel to each other as before and lay in two parallel planes with 12 microns gap between them.

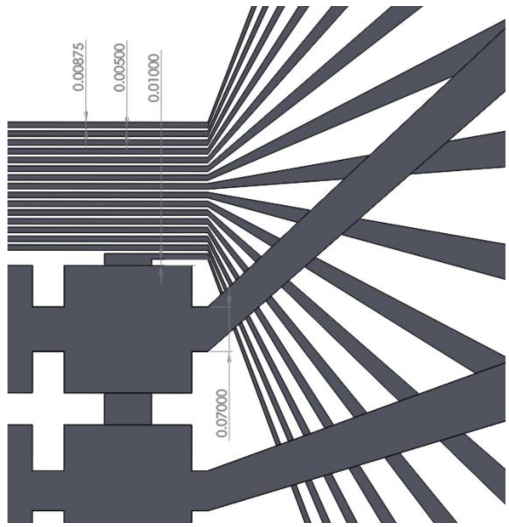

Figure 22: High Density wiring part; All units in mm

Insulation Layer

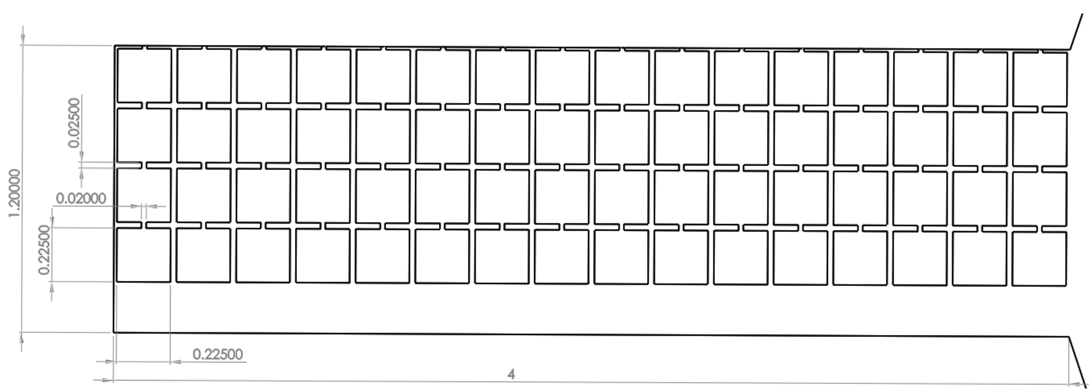

Figure 23: Insulation layers with Modified Air Pocket; All units in mm

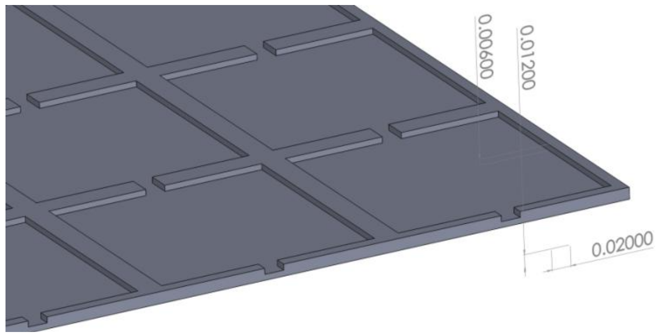

Figure 24: Air Pockets with Connected Air Channels; All units in mm

Due to reduction of one vertical electrode, the size of each air pockets were adjusted to a new dimension of 225X225 microns with horizontal gap of 25 microns and vertical gap of 20 microns shown in Figure 23. This time the air pockets were not isolated but connected by tiny air channels of 20 microns width with each other and the entire air channel finally opens to atmosphere at one end shown in Figure 24. As a result of these micro-fluidic channels, when the insulation layer would be deformed under pressure, the trapped air would be able to pass through these channels towards open atmosphere and the pressure inside the sensor would initially remain atmospheric before deformation starts.

Connecting Pads

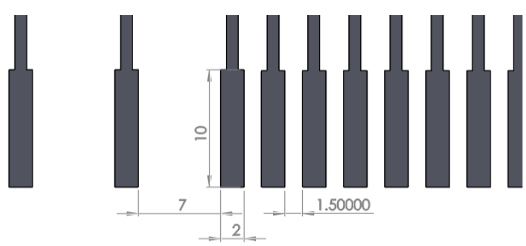

Figure 25 Continued: Pads for All Electrodes; All units in mm

One of the primary aspects of this second iteration of design for this sensor was, the features were made as big as possible especially the part located outside the knee joint and not so much space were left in the first design of the sensor compare to second design. To be consistent with those criteria the sensor lower part was designed with larger surface area to be accommodated in a single 100mm silicon wafer easily. Based on this design it would be possible to fabricate a single sensor at a time over a 100mm silicon wafer in the clean-room environment. The terminal pads of both 16 horizontal and 4 vertical electrodes were kept at 2mm width and 10 mm length. The air gap between terminal pads of the vertical and horizontal electrodes were 7 mm and 1.5 mm respectively as shown in Figure 25.

<u>Drawbacks of This Design</u>

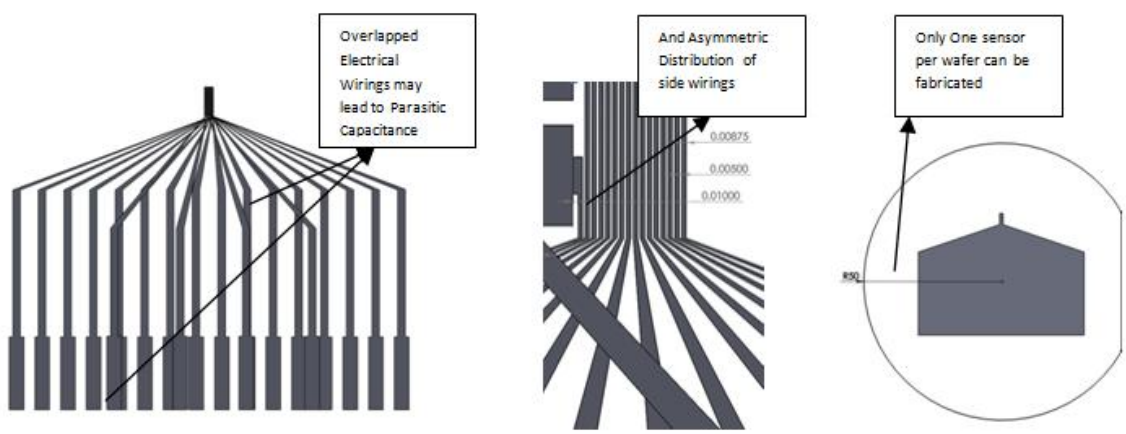

Figure 26: Design Drawbacks

One of the major Drawbacks of the second iteration of the design for this pressure sensor was overlapped wires for both Vertical and Horizontal electrodes in multiple locations. As a result of overlapping there could be parasitic capacitance growing among wires and connecting terminals which would be counted as gain and offset errors that cannot be suppressed by auto calibration (7). Also because of the asymmetric distribution of the side wires of the horizontal electrodes all 16 wires were routed in the same direction which resulted in a high density metalized features of very small size. Since they were not overlapping and all the 16 side wirings would be in same potential so there were less chances of developing parasitic capacitance among the high density metal parts. But asymmetric nature of the design could produce too much stress concentration in one side of the sensor thereby leading to failure of the delicate metal layers. Also to accommodate the big dimensions of the lower part of the sensor, only one sensor could be fabricated on a wafer size of 100mm diameter which would not be so efficient and cost effective considering the expensive nature of such clean-room micro fabrication. These shortcomings were attempted to overcome in the third and final iteration of the design.

Third Iteration of Design: Micro-Fabrication Steps

The Next iteration of the design parameters such as sensor width, number of electrodes, thickness of metal layers, and total width of the sensor was modified according to initial clean room micro- fabrication process steps. The sensor was designed to be fabricated on a standard cleanroom environment over a silicon wafer following micro-fabrication and photo-lithography techniques. A short description of different Micro-fabrication terminologies before describing the sensor Micro-Fabrication steps is given below:

Photolithography

Photolithography is one of the most significant steps in Micro-fabrication where patterns are created in substrates with sub micrometer resolutions (5). It encapsulates all the steps involved in transferring a pattern from a mask to the surface of the silicon wafer (20). The basic steps in Photolithographic process are discussed below:

Cleaning Wafer

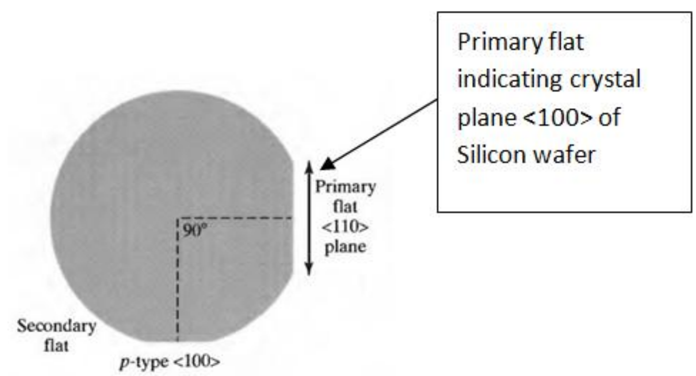

Figure 27: Silicon wafer with Primary and Secondary Flat and Orientation; Image Modified from (5)

Micro-fabrication starts with n- or p- type silicon wafers with 1 to 8 inch diameters are being widely used in the IC fabrication industry. They are indentified by a standard straight edge known as wafer flats in their geometry. The wafer flats indicate the wafer type (n-type or p-type) and the surface orientation (<100> or <111>) as shown in the Figure 27. The cleaning of the wafer is mostly done by deionized water (DI) and a solution of hydrofluoric acid removes any oxide that may have formed in the wafer surface (20).

Barrier Layer Deposition

After the wafer is cleaned it will be covered with some barrier layer that will either provide insulation or act as a etch mask during photo lithography. Some common barrier layers are Silicon Dioxide, Silicon Nitride, Polysilicon, photoresists and metals etc. The processes that are used to deposit these barrier layers are chemical vapor deposition, physical vapor deposition, thermal oxidation, sputtering and vacuum evaporation etc. (20)

Photoresists Layer

Once the barrier layers have been formed the silicon wafer is coated with some light sensitive material known as photoresist. The wafer surface needs to be cleaned to ensure good adhesion between the photoresist and surface. Photoresists are typically applied over silicon wafer in liquid form by spin coating the wafer on a chuck at 1000-5000 rpm resulting in 2.5 to 0.5 microns thickness respectively. The actual thickness of the resist depends on its viscosity and is inversely proportional to the square root of the speed. (20)

Soft Baking

This is a drying step used to improve adhesion and remove any solvent from the photoresist and usually done from 5-30 minutes in an oven from 60 to 1000C in air or nitrogen atmosphere following manufacturer specifications closely (20).

Alignment of Mask

Mask alignment is used to transfer any pattern to the wafer sequentially in case multiple patterns are present. For that purpose special alignment marks are used in the mask design to keep track of the reference point and orientation. Mask alignment could be controlled by computer or manually depending on the accuracy requirement of the alignment tolerances. The basic manual alignment equipment uses an adjustable x-y stage to move into the position below mask and the mask is spaced 25 to 125 μm above the wafer surface (20). The Figure 28 shows alignment marks in a mask design.

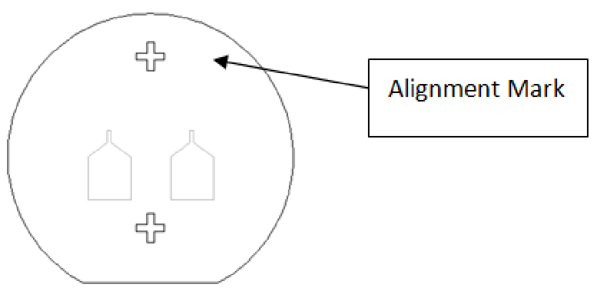

Figure 28: Mask Alignment Marks

Photoresist Development

After the mask alignment is done the photoresist is exposed to high intensity ultraviolet light (20). Wherever the resist comes into contact with UV light that part of the resist will be washed away by the developer solution thereby exposing bare silicon or silicon oxide area (20). As a result when the surface is exposed to etching solution the etchant will react with the unprotected part of the wafer. This type of photo- resist is the most common type and known as positive photo resist. There is another type of resist which stays intact after developing when exposed to UV light and they are known as negative photoresist (20).

Etching

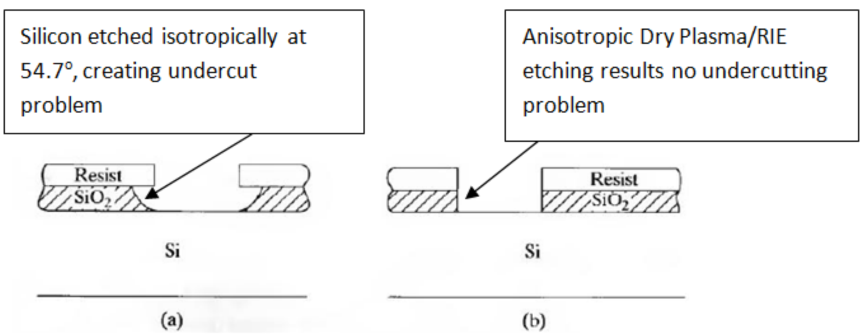

Figure 29: a) Isotropic wet etching of silicon by KOH results occurs in 54.7 degrees b) Dry anisotropic etching in a plasma or reactive ion etching environment

Etching is one of the most important processes in Microfabrication which involves removal of materials in desired areas by chemical or physical process (5). This is the way any permanent pattern can be developed at any substrate by photolithography. Physical etching is usually referred to dry etching or plasma etching and chemical etching refers to wet etching. Chemical etching is used in the form of diluted chemicals to dissolve material like HF (Hydrofluoric) solution is used to dissolve Si3N4, SiO2 etc whereas KOH (Potassium Hydroxide) is used to etch the silicon substrate (5). The etching rate depends on the concentration of the etching solution, type of the material to be etched and temperature of the solution. Dry etching is suitable to achieve highly anisotropic profile like avoiding undercutting problem involved in wet processes shown in Figure 29. Plasma dry etching system uses a stream of positive charge carrying ions of a substance with large number of electrons diluted by inert carrier gas like argon, and it can be generated by high voltage electric charge or RF in vacuum (5). Reactive ion etching (RIE) is a combination of plasma and sputter etching processes where plasma systems are used to ionize reactive gases and the surface is bombarded by the accelerated ions. Both Plasma and RIE etching results in highly anisotropic etching process whereas chemical etching results in isotropic etching (5).

Recommended Fabrication Steps

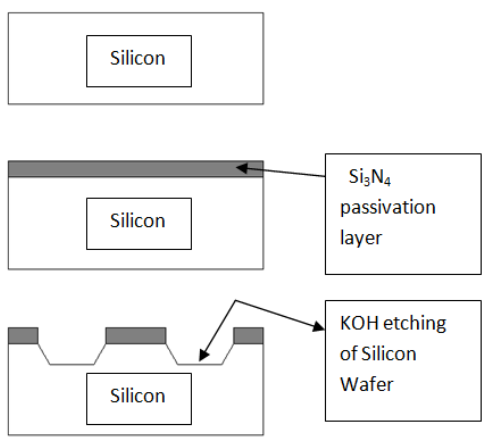

Figure 30: Step 1 of the Fabrication process

Step 1. a) Silicon Nitride (Si3N4) passivation layer would be used to act as barrier layer or etch Mask shown in Figure 30.

b) After the Silicon Nitride layer has been formed the surface of the wafer would be coated with Photoresist which is a light sensitive material

c) Then Proper mask would be applied to create the mold to cast polymer bumps. For that the Photoresist would be exposed to high intensity Ultraviolet light wherever the silicon nitride is needed to be removed so that the etching solution could come into contact with the wafer and etch the desired area.

d) In this way the mold for casting Polymer bumps would be created by using KOH etchant.

e) Finally the Remaining Si3N4 and any remaining Photoresist would be removed.

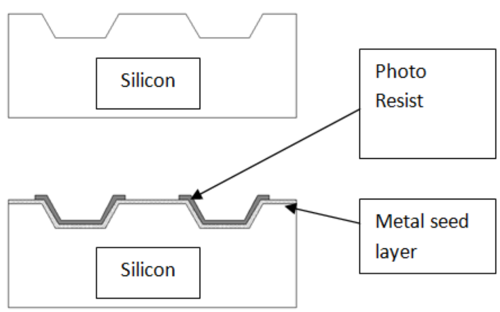

Figure 31: Step 2 of the Fabrication process

Step 2.a) a sacrificial Layer or Surface treatment layer would be applied prior to the electroplating process.

b) Titanium/Metal seed layer would be deposited where Titanium would be used for adhesion between polymer and metal layer

c) Photoresist would be applied for masking and later the electrodes pattern would be transferred to the silicon wafer. The UV light would transmit through the transparent part of the mask and react with the Photoresist which would be later developed with the help of developer solution and eventually expose the metal seed layer.

Step 3a) Metallization by electroplating technique would Produce Upper and lower electrodes layer

b) Then Polymer material would be casted by spin coating technique on top of the metal layers in silicon wafer as shown in Figure 32.

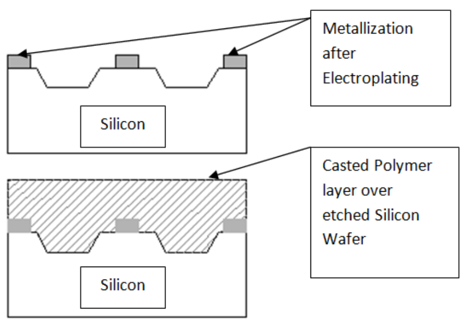

Figure 32: Step 3 of the Fabrication process

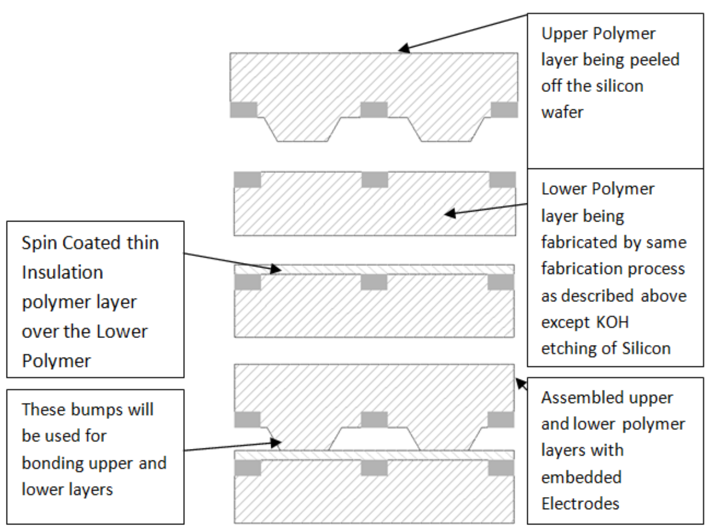

Figure 33: Step 4 of the Fabrication process

Step 4a) Removal of sacrificial layer if necessary

b) Following the same fabrication steps, lower polymer layer would be fabricated in Planar Silicon Substrate i.e. without the KOH etch. Then a thin insulation layer on top of Lower Polymer layer would be spin coated or deposited by oxygen Plasma activation.

c) Then Peeling both the devices from silicon wafer and assembling the upper and lower Polymer layers with the help of bumps acting as bonding substance.

The Bumps looked prism shaped because they would be casted on silicon wafer pockets created by anisotropic KOH etching of Silicon (<100> plane) which would take place at an angle of 54.74 degrees (21)

Final Design Parameters

Total Sensor

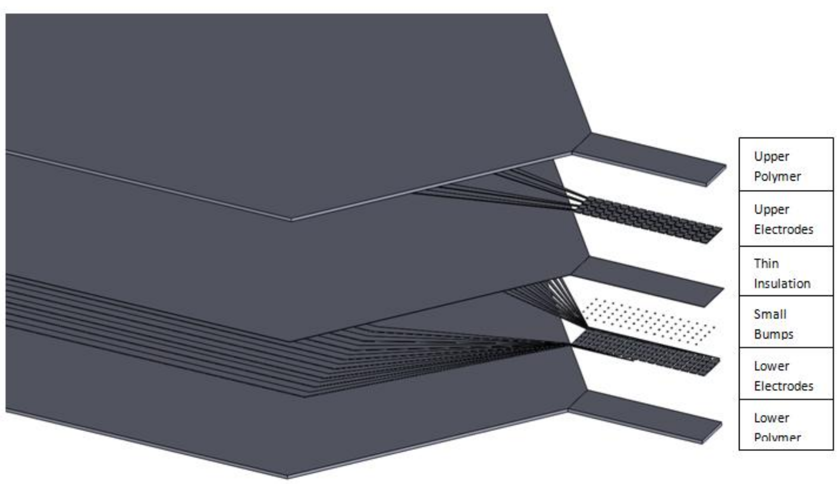

Figure 34: Exploded View of the Pressure sensor; Third and Final Iteration

The Pressure sensor was modified for the third times based on the above fabrication steps and later it was tweaked based on some recommendations. The dimensions of the sensor were again modified to optimum values although the original dimension of the main sensor area was unaltered from the second design iteration which was 1.2 by 4 mm. The description of each layer is given below:

Upper and Lower Polymer Layer

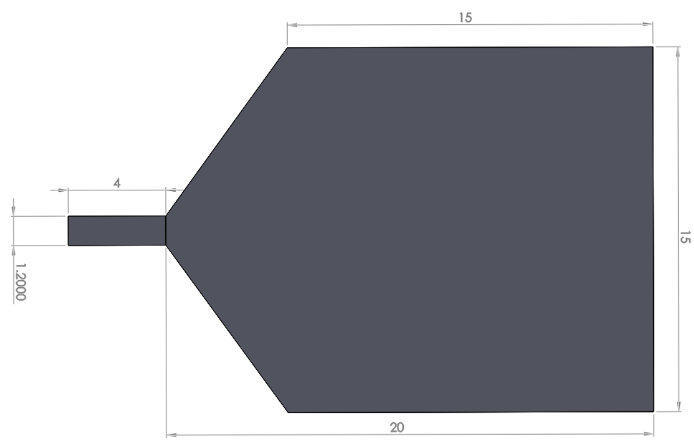

Figure 35: Upper and Lower Polymer Layer Final Version; All units in mm

The dimension of the original capacitive sensing area was kept as before but the area where it would encapsulate all the circuit wirings and connection terminals were adjusted to an optimum dimension of 15X15 mm with the top edges at an inclined position to coincide with the lower end of the rectangular sensor shown in Figure 35. The ascending nature of the edges would allow the sensor to be inserted in the mouse knee joint more conveniently without interference. The reduced dimension compared to the 2nd iteration of design would allow at least two of these sensors to be fabricated on a

100mm silicon wafer which would yield two sensors instead of one with the same amount of resources like masks, chemicals for etching, metal deposition for electroplating, polymer material during spin coating deposition and reduced waste of materials during fabrication process.

Upper and Lower Electrodes

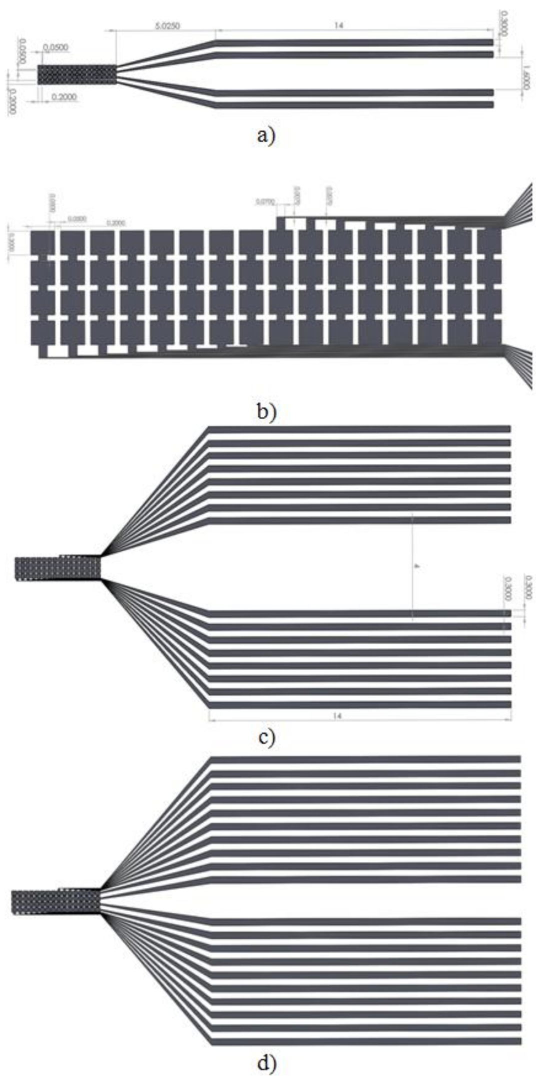

Figure 36: Four Upper Electrodes with dimensions in mm unit; b) Sixteen lower electrodes with Dimensions in mm unit c) Side wiring distribution of lower electrodes d) both upper and Lower Electrodes in parallel position

In the third iteration of design the most notable changes were the redistribution of the side wirings for both upper and lower electrodes. This time connecting terminals for the upper electrodes were much more concise and compactly located and projected at the middle of the polymer housing symmetrically as shown in Figure 36(a). On the other hand the side wirings for the lower electrodes were projecting from both sides of the sensor at equal number this time shown in Figure 36(b). As a result it was possible to avoid overlapping of connecting terminals of upper and lower electrodes completely as shown in Figure 36(d) and the distance between the parallel wires were large enough to avoid any substantial build up of parasitic capacitance. The dimensions of the parallel plate capacitors were unchanged (200 X 200 microns) but the size of the connecting terminals were changed. Both upper and lower electrodes had the same width and length of their straight connecting terminals which were 14mm and 0.3mm respectively in Figure 36(c) and the inclined lines were at 5.0250mm height vertically from the base of the sensor projecting out symmetrically (Figure 36: a and c). The air gaps between the electrodes were similar to their width which was 0.3 mm and the distance between the symmetric electrodes located at the middle and the center line were 0.8mm and 2mm for upper and lower electrodes respectively.

Bump Layer Initial and Final Design

Figure 37 Continued: Bump layers for bonding process; All units in mm

According to the estimated fabrication steps it was discovered that bonding between different layers of polymers might not be very convenient process. That's why the rectangular bump layers were introduced in the design instead of just thin insulation layer containing air pockets. These bump layers would provide dual functionality in the sensor structure. First was creating the desired air gap between the electrodes and second was creating physical bonding between the upper and lower polymer layers. The bonding process would occur when the lower polymer layer containing the rectangular bumps would be squeezed with the upper polymer layer with a thin layer of spin coated insulation layer on top of it. Initially there were 75 small bumps incorporated in the design of the sensor design. The middle 45 bumps about the center line bumps of the bump layer were equidistant from each other (0.208 mm) and the 30 small bumps at the edges were also equidistant from their neighboring bumps by 0.2460mm shown in Figure 37. The geometric shape of the bumps were similar to a three dimensional trapezoid since the anisotropic potassium hydroxide (KOH) etching of silicon <100> wafer occurs at 54.740 (21). The Figure 38 shows how an individual small bump would look due to nature of anisotropic etching rate of silicon.

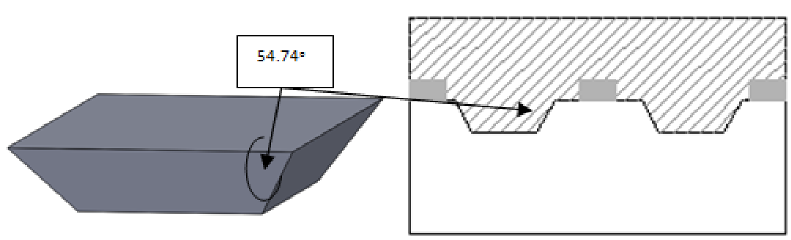

Figure 38: created by casting polymer on silicon mold created by etching

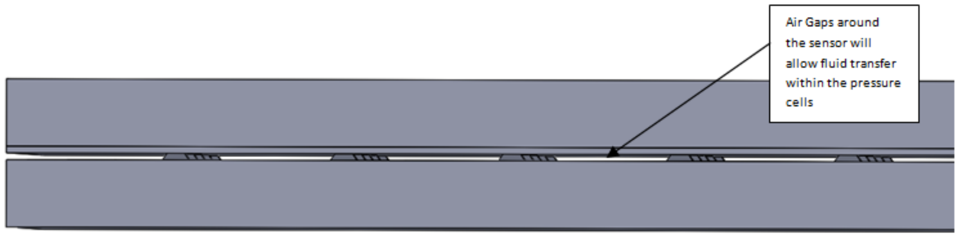

Figure 39: Bumps layer created around the edge of the sensor

Here would be a technical difficulty due to these bump configuration which was the pressure chambers were open on either side of the sensor as shown in the figure. During pressure measurement inside mouse knee joint, the dissected knee needed to be sprayed over time to time to keep it from getting dried out. Because of the spraying the knee joint area would get wet and the sensor might also get wet when it would come into contact with wet knee joint area. If liquid particle would get inside the capacitive cells it would greatly alter the functionality and charge storage ability of those cells. So the sensor surroundings needed to be insulated from any transfer of liquid. As a result a solid continuous bump layer was designed all around the sensor structure to prevent any liquid particle entering inside the pressure chambers except the very end where the circuit connection terminals situated were kept open shown in Figure 40. The open end would be located far away from the spray zone at the fixture part of the sensor. Trapped air inside the pressure cells would travel to atmosphere through this open channel at the end of the sensor and this would keep the pressure cells in atmospheric pressure under no load condition. The modified bump design is shown in Figure 40.

As a result of the solid continuous bump, total numbers of small bumps were reduced from 75 to 45 located within the matrix of capacitive cells. The solid bump would seal the boundary around the edge of the sensor which was necessary for proper functioning of the capacitive cells and it served as a good bonding media between the wide parts of the polymer layers.

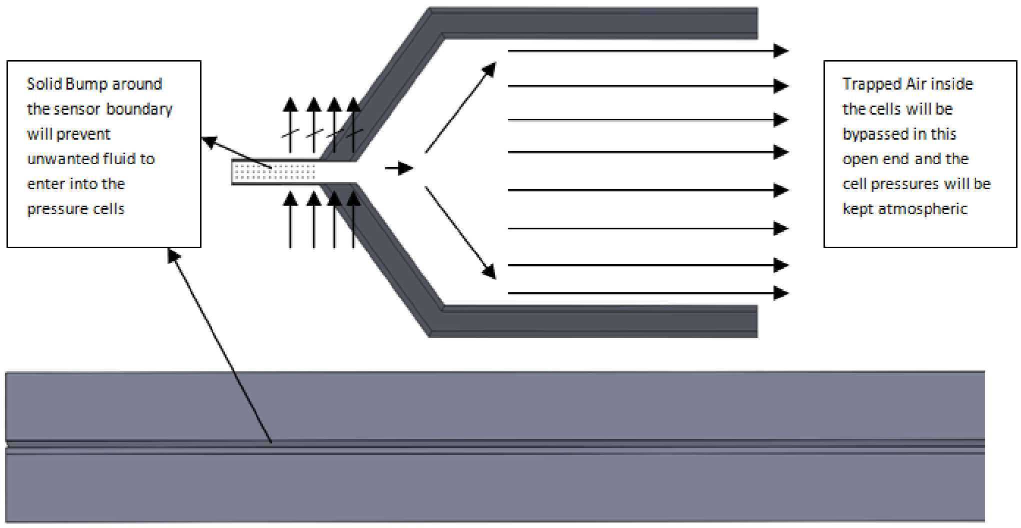

Figure 40: Solid Continuous bump around the edge along with small bumps

The 45 small bumps would provide the necessary air gap for proper operation of each capacitive cell and the solid insulation layer will provide the dielectric medium as well as prevent a pair of electrodes from coming into physical contact with each other which would have greatly reduce the charge holding capacity of the electrodes.

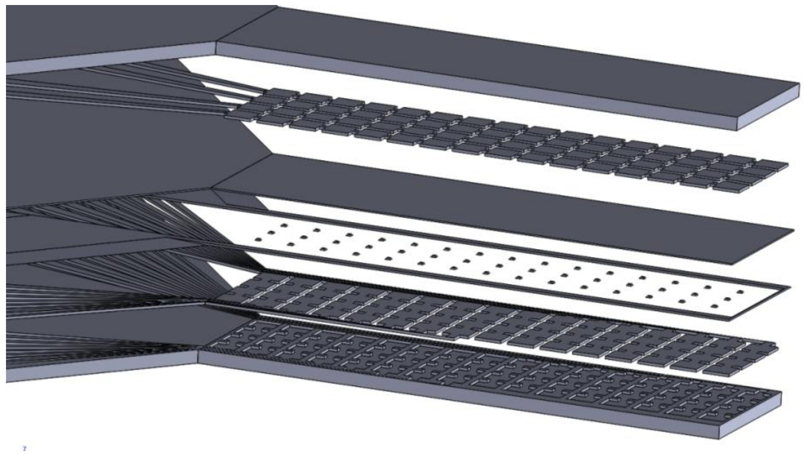

Figure 41: Exploded view of the final configuration of different layers of the Sensor

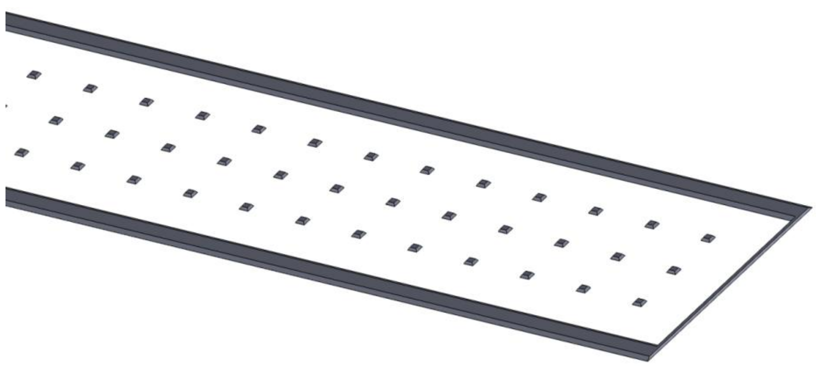

Figure 42: Modified bump Layer with Continuous Solid bumps

Mask Design

The dimensional accuracy of the fabricated parts and in order to be able to maintain that accurately through photolithography and etching processes is very important (20). The micro patterns that we have designed would be created by photolithography through using Photo-masks and masks are used for etching in both surface/bulk micromachining and thin film deposition. These photmasks are physical devices that would also need to be fabricated in order to perform photolithography. Mask fabrication requires a series of photographic process and it begins with a large scale drawing of each mask. The original mask could be 100 to 1000 times larger than the actual feature size on the silicon wafer. The image of the desired mask would be first created in the computer graphics system. Later an optical pattern generator would expose the mask image directly onto a photographic plate known as reticle and an electron beam projection system would draw the pattern directly over electron sensitive material. Reticle images could be 1 to 10 times to its final size and a camera lens would reduce the reticle image size to its final feature size and expose the two dimensional array of images on a master copy of the final mask (20). The outline of mask fabrication process and the optical exposure system is given in Figure 43 and 44 below:

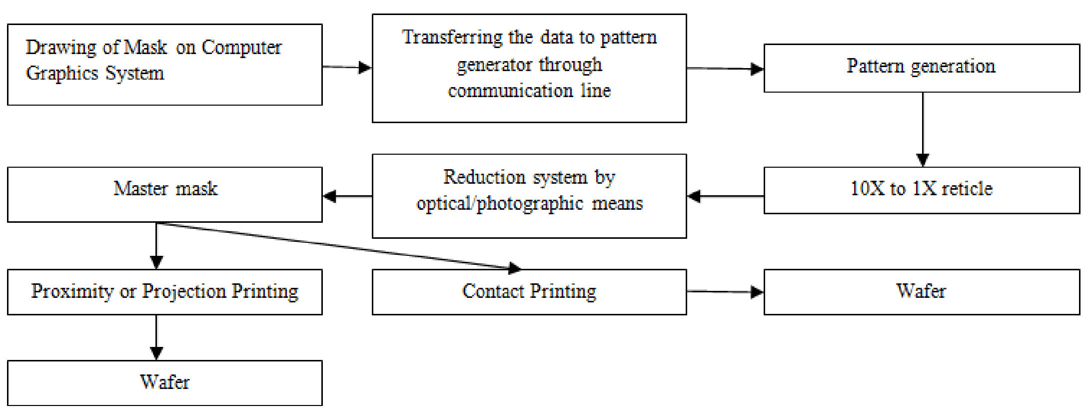

Figure 43: Fabrication process outline (20)

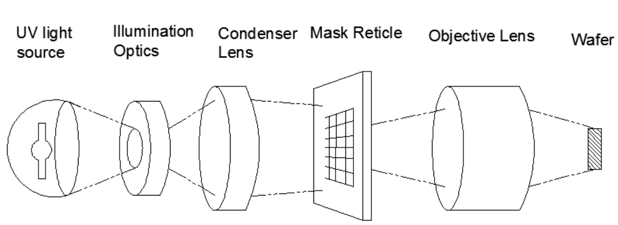

Figure 44: Optical Exposure system of Mask to wafer: Image redrawn from textbook (20)

The preparation of mask is an essential step for the micro-fabrication procedure. In order to transfer the desired pattern into the silicon wafer it would need the process-steps and designs to be fixed at first. After the finalization of the design the pattern could be optically transferred and projected onto the surface of the wafer as shown in figure: . The minimum feature size that can be produced by photolithography would depend on the wavelength of light used in the exposure (20). The exposure system could be of two types which are contact printing and proximity/projection printing (20). Contact printing might yield high resolution pattern transfer economically in terms of research and prototyping but the projection printing on wafer is still most widely utilized and practiced (20). Contact printing could damage the surface of the mask and wafer both. On the other hand the mask would be brought into very close proximity of the wafer in projection printing method but no contact would be made with wafer during exposure thereby preventing damage to the mask (20). When designing the mask in the computer graphics system it would need some rules to be followed like alignment marks, trace size, dimensional consistency, repeatability, reusability and cost effectiveness.

From the fabrication steps of the third and final design it was evident that it would require two masks for the metallization process and one mask for the bumps layer by etching cavity on the silicon wafer. For the structural encapsulation with polymer material it would not require a mask since we would not be etching any polymer material instead it would be deposited by spin coating method over the etched cavity on silicon wafer which would create bumps layer. Later with the help of alignment marks the outside geometry would be cut according to the pattern dimension. The thickness of the spin coated polymer material would be controlled by controlling the RPM (Revolution per minute) of the platform of spin coating machine and time of spin coating process according to the manufacturer specifications of the material.

The designed masks created in the CAD system would be presented based on the fabrication steps for the micro-pressure sensor. The following rules were followed when the masks were designed in the computer graphics system:

- The scale of the whole drawing layout was kept in “Microns”.
- All the features were drawn with respect to a 100 mm wafer system.
- Whole wafer was centered with respect to the origin (zero co-ordinates) of the layout.
- All the patterns in the drawing were continuous line and closed polygon system.
- The wafers were containing alignment marks so that the different masks could be placed on the same spot and alignment marks were close to the center of the wafer.
- Both the metallization masks and bump layer mask were aligned (i.e. the devices were on the same spot on each mask)

Metallization Masks

The metallization masks contained the pattern of upper and lower electrodes layer. They were situated side by side on the silicon wafer so that both the upper polymer layer containing the upper electrodes and the lower polymer layer containing the lower electrodes would be fabricated at the same time by photo-lithography technique.

Moreover both patterns were located on the same mask so that only one mask would be needed for the whole metallization process. In this way it would save fabrication cost for additional masks for each individual pattern and this approach would yield cost effectiveness. From the Figure 45, it is evident that the clear part (transparent part) of the masks is the pattern we would like to print on the silicon wafer and anything outside the transparent part would remain under photoresist since the photoresist that would not come into contact with UV (Ultra violet) ray would remain intact and un-developed. Therefore the geometry below the photoresist would not have any metallization process except the clear part where the photoresist would come into contact with UV ray and later developed and removed exposing the seed layer. As a result the transparent exposed part of the wafer through the mask would undergo deposition of metals through electroplating process with the help of exposed seed layer. The Figure 45 and 46(a) shows the upper and lower electrodes Mask on the same wafer with the solid hatch line being applied to indicate which part of the mask would be opaque and which part would remain clear.

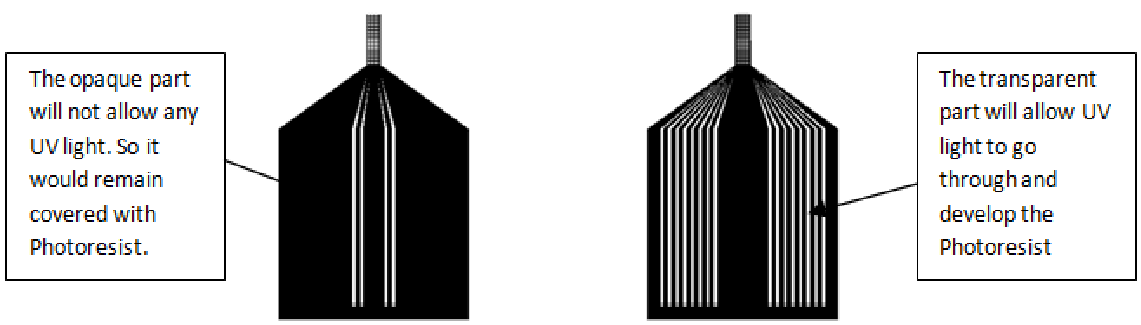

Figure 45: Illustration of opaque and transparent part of the metallization masks Left one for Upper and Right one for lower Electrodes

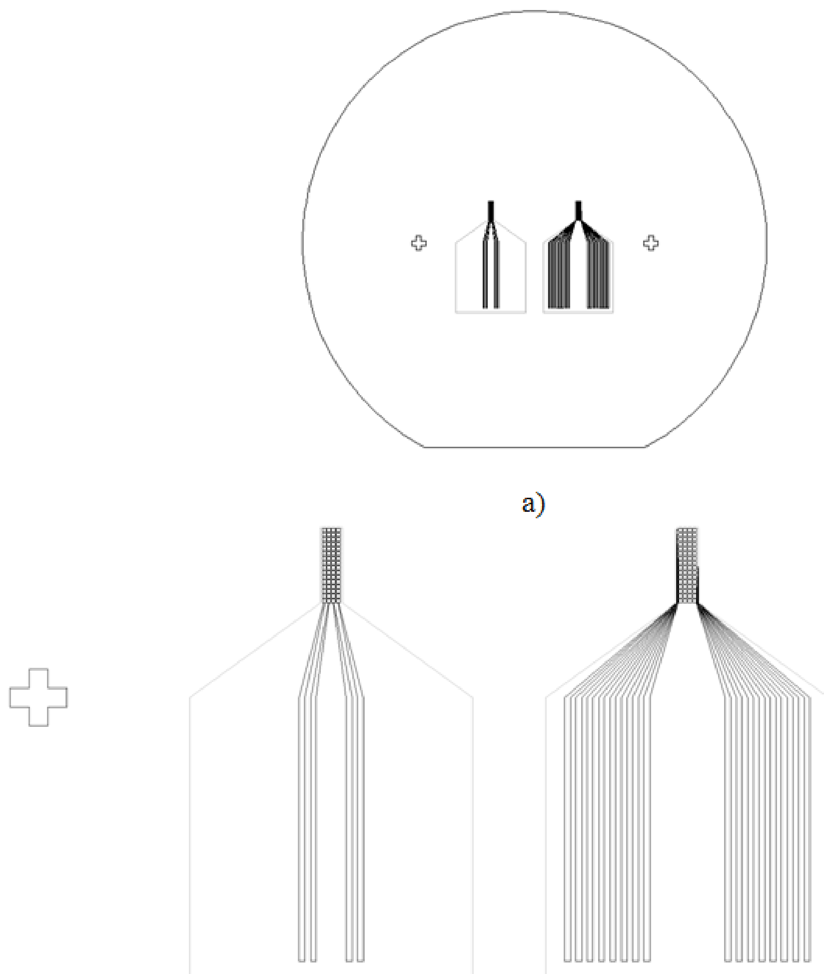

a)

b)

Figure 46: Electrodes layer Mask with the alignment marks a) wafer view b) zoomed in view

The solid black hatch line in Figure 45 was to indicate which part will allow UV light to remove photoresist during lithographic process. But in the original drawing files of the mask the hatch lines were not used instead they were removed from the drawing and all the features were drawn with closed polygon without any open ended lines (Figure 46 (b). The reason of not using any hatch lines were the closed polygon system would be considered filled by default with the GDSII database system of the mask making machines. That's why the masks were designed as a bright field since it would be inverted at the mask making machine which would create dark filled zones in the mask.

Bump Extrusion Mask

The bump layer mask contained only a single feature in contrast to two features in the metallization mask. In this case the bump layout was closer to the right alignment mark which would make the feature exactly aligned with the traces of lower electrodes as shown in figure: . The bumps would be created by anisotropic etching of silicon wafer with KOH solution so UV light needed to be passed through wherever we wanted the holes to be created on the silicon wafer defined by the mask. The clear zone will allow UV light according to the pattern of the continuous solid bumps and forty five small bumps to react with the photoresist applied on silicon wafer shown in Figure 47. After reaction with the PR it will be developed and removed by developer solution thereby exposing those locations on the silicon wafer to be etched and bump shaped holes to be created. The dark zones would not allow any UV light thereby the PR on that region would be undeveloped and silicon surface under the PR would stay intact and not be exposed.

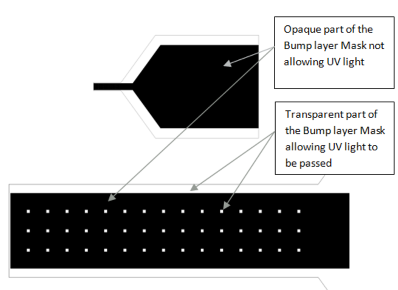

Figure 47: Illustration of opaque and transparent zone of the bump layer Mask

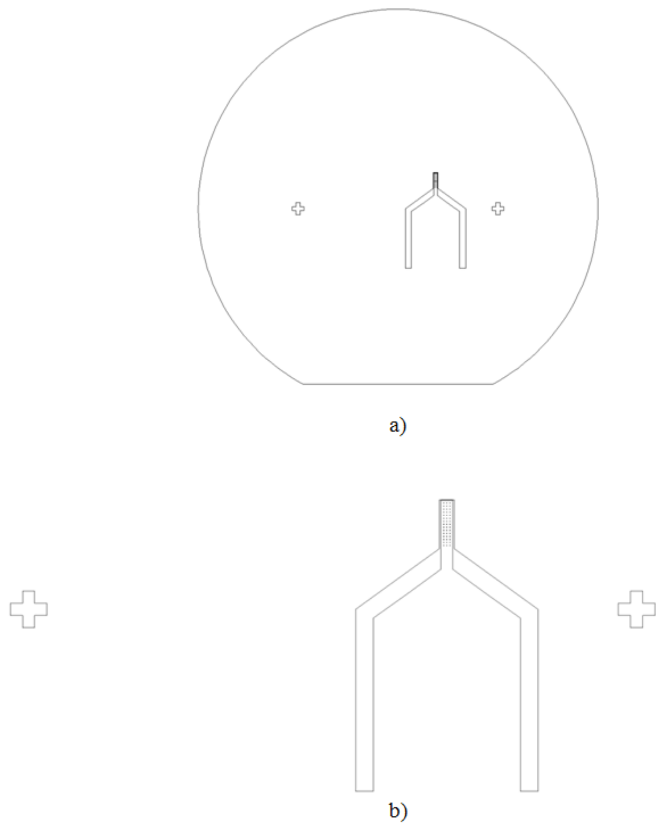

Figure 48: Layer Mask with the alignment marks a) wafer view b) zoomed in view

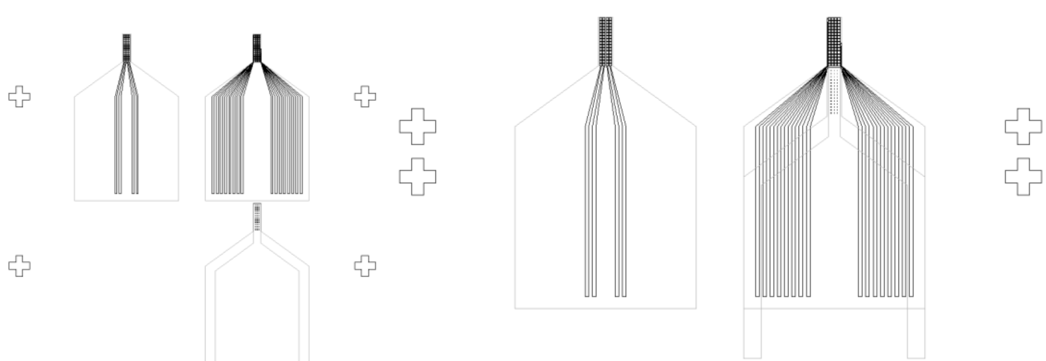

Figure 49: Mask Alignment in progress: a) The bump layer mask is brought near metal layer mask b) the alignment marks are about to be overlapped on each other

The features in the bump layer mask were kept close to the right alignment mark shown in Figure 48(a) and (b) in such a way that it was exactly in the same position as the lower electrodes feature were located on the metallization mask. As a result the bumps could be easily created below the lower electrodes according to the designed fabrication process steps. The bump mask could have been easily accommodated on the metallization mask but it was designed separately as an individual mask because the creation of the bump layer involved separate process steps compared to the electroplating and metal deposition process. According to the profile of the features on these masks it could be easily estimated that the process steps would yield at least two fully functional identical sensors (shown in Figure 46(a)) after the end of each individual fabrication process.

MATERIAL SELECTION

There are different types of materials that can be used in building Microsystems. But selecting the appropriate material based on proper application is paramount. One major criteria for selecting the right material is to follow the process flow designed for the particular requirements such as etchants, thin film deposition etc (5). Since our photolithography process for the fabrication of micro-pressure-sensor involved polymer as the passive substrate material and metals as the active substrate material as well as sensing component in the Microsystems we will be concentrating mainly on those two categories. We will also consider a composite polymer structure in our material selection process of the pressure sensor.

Polymers

Polymers have become increasingly popular material for Microsystems and MEMS in diverse application such as micro fluidic systems, biomedical devices, pressure sensors, tactile sensors and so on. Polymers have been conventionally used as insulators, sheathing, and capacitor encapsulation in electronic devices and die pads in IC's (5). Few advantages of polymers as structural material are light weight, electrical non conductivity, high corrosion resistance, high flexibility in structures and ease of processing. Thin polymer films are also used as electric insulators in micro-devices and as a dielectric substance in micro-capacitors. They are ideal material for shielding against electromagnetic and radio frequency interference and widely used for packaging of other Microsystems (5).

The primary features that we were looking for during our material selection process were: flexibility, ease of fabrication process, ease of availability, economical feasibility, ease of machining, chemically inertness or non-reactive, good insulation and dielectric properties, good adhesiveness and ease of bonding or good bonding characteristics and above all biocompatibility. For our micro pressure sensor we primarily considered two types of polymer materials from the perspective of above mentioned characteristics. We considered Polyimide and PDMS (Polydimethylsiloxane) as two possible candidates for the structural material as well as insulation and dielectric medium of the sensor.

PDMS

It is an acronym for Polydimethylsiloxane which is a silicone elastomer: is primarily used for embedding electronic components through casting in order to prolong lifespan (22). It acts as a dielectric insulator and protects the components from influences of environment, mechanical shock and vibration within a large temperature range (-50 to 2000C). It has been used in Micro and nanotechnologies since 1995 due to its good contour accuracy (<10nm) (22). It has become one of the most popular materials in micro Total analysis system (μ TAS) and polymer MEMS due to its attractive features such as flexibility, elasticity, transparency and biocompatibility (23). Flexible and elastic features are utilized effectively in pneumatic balloon actuator (PBA), piston mirror array device (PMA), micro pump for μ TAS devices, fluidics (valves, pumps, fluidic circuits) (23) and optical systems such as adaptive lenses, tilting mirrors, (22) and other sensors such as acceleration sensors, tactile sensors, chemical sensors and medical sensors (22).

The dielectric constant and elasticity of the dielectric layer as well of the embedding structure determines the sensitivity of the pressure sensor and they influence the mechanical and electrical properties of a micro-sensor (25). The attractive flexibility, good dielectric property and linear elastic behavior might be suitable for the construction of the capacitive type micro-electronic pressure sensor. Some analysis based on elastic properties of PDMS, relative capacitive changes in the PDMS based structure, stress analysis simulation of the designed sensor with PDMS as the structural material would be presented in the later chapters. The mechanical properties of PDMS found in various journal articles would be discussed and capacitive characteristics under applied pressure would be analyzed.

The structural properties of polymer networks are highly dependent to the reaction by which they are formed (24). It is essential to know about the imperfections in the network structure of polymers caused by cross linking in order to interpret their modulus of elasticity properly (24). The elasticity of PDMS is tunable by different mixing ratios of the PDMS pre-polymer and the curing agent during formation (25). The ideal property of PDMS for our micro pressure sensor would be to have linear modulus of elasticity and Poisson’s ratio. The PDMS stress-strain characteristics have been investigated in (25) in-order to select a suitable mixing ratio for the insulation layer of the sensor (25). The characterization procedure of the PDMS involved making cylindrical PDMS samples by degassing the pre-polymer and curing agent in a vacuum chamber and pouring into pre-fabricated cylindrical mold described in (25).Then each specimens made by different mixing ratios were baked at 70 C for around two hours (25). The cylindrical

PDMS samples were subjected to uni-axial tensile test to find out stress-strain relationship of five mixing ratio samples in (25). The five mixing ratios of the PDMS pre-polymer and the curing agent performed in (25) resulted in different stiffness values of PDMS and the stiffness increased as the portion of the PDMS pre-polymer increased in the mixture (25). The stress-strain relationship acquired in (25) were non linear for the mixtures containing high PDMS pre-polymer (25). The stress strain data of five different mixtures of PDMS pre-polymer and curing agent will give the selection of the proper mixing ratio based on the operating pressure range of our micro-pressure sensor. The graphical representation of the summary of the stress-strain relationship published in (25) is given in Figure 50 below:

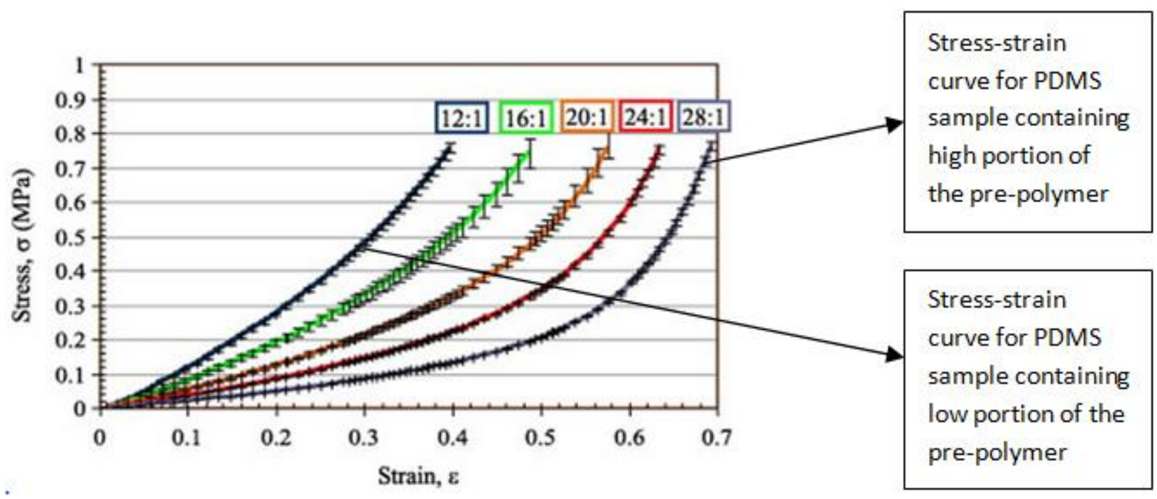

Figure 50: The stress vs. strain curves of PDMS specimens with five different mixing ratios of the pre-polymer and curing agent (12:1, 16:1, 20:1, 24:1, and 28:1); image modified from (25)

Based on the operating pressure range of the sensor, It can decided on selecting the proper mixing ratio of the PDMS that would yield highest linearity and highest elasticity from the above graph. From Table 4 and free body diagram as well, it was clearly evident that our maximum external applied pressure on the mouse knee would result at 25% contact area for 50 gm load which was equivalent to 464 kPa (rounded figure) or 0.464 MPa of pressure (Force over area). Since the interested range of pressure was between 0.4 and 0.5 MPa the optimum highest linearity of stress-strain relationship within this desired pressure zone could be found by 12:1 mixing ratio of PDMS pre-polymer and curing agent. The capacitance vs. pressure characteristic graph would be plotted for PDMS as the structural material. A certain gap between the parallel plate capacitor was considered, started with zero loads and the initial capacitance between the parallel plates sandwiching PDMS as dielectric material was calculated as well as PDMS as embedding material in the top and bottom layer. Then the gaps were descended step by step until it was completely closed. The capacitances as well as change of capacitance with respect to initial capacitance at each step of gap changes and final capacitance value at closed condition were calculated.

The article in (22) has discussed and characterized the mechanical properties of PDMS elastomer. The mixing ratio of PDMS in (22) was 10:1 for two most commonly used silicones: RTV 615 and Sylgard 184 with hardener solution. According to the experimental work in (22) they have found a larger linear behavior of room-temperature-vulcanized (RTV) silicones up to a strain of 100%. The experimental stress-strain diagram obtained from (22) is given in Figure 51. From the graph it is clearly discernible that both silicone polymers exhibit a linear stress-strain relationship up to a strain of 45% which corresponded to a constant elastic modulus of 1.76 MPa for Sylgard 184 and 1.54

MPa for RTV 615 (22). It is also visible that 0.45% strain for both types of silicone corresponded to a stress of 0.5 MPa which is well between the maximum operating pressure ranges of our pressure sensor. Beyond the linear region the stress-strain relationship went nonlinear but the non linearity is not prevailing until the applied stress exceeds 1.5 MPa which could be safely assumed to be non applicable and higher in comparison to our operating pressure range of 0.464-0.5 MPa.

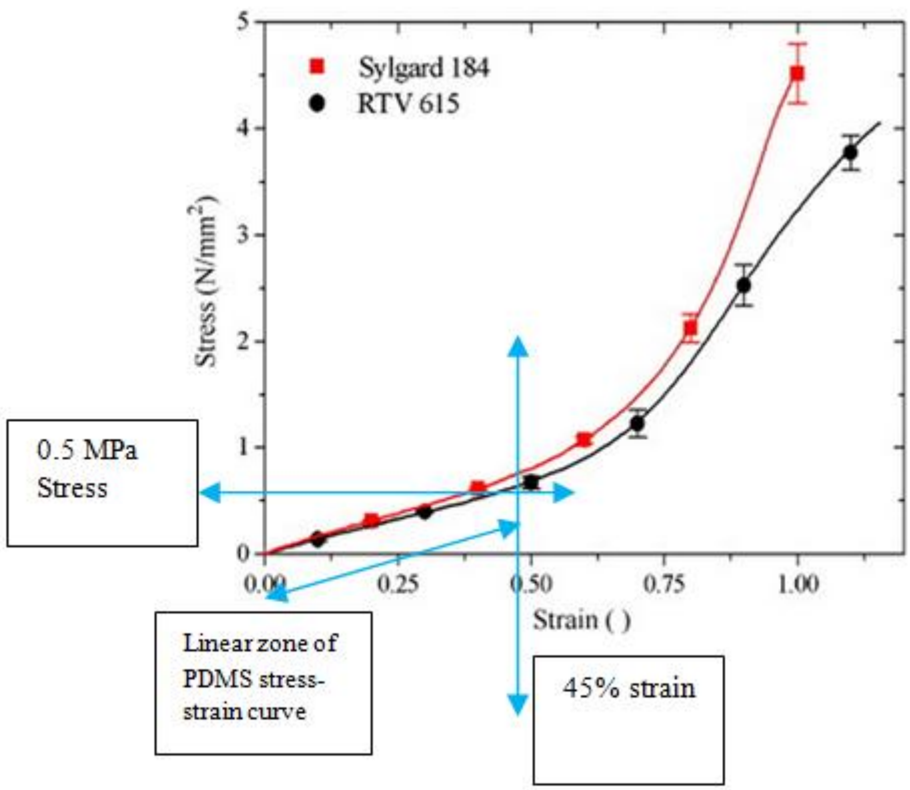

Figure 51: Stress Vs Strain plot of two different types of PDMS elastomer: RTV 615 and Sylgard 184; image modified from (22)

Based on the above literature findings it could be safely assumed about the persistence of linearity of material properties of PDMS specific to the application of pressure sensor during stress and structural analysis using finite element method and during comparisons with other polymer materials for material selection.

It was required during the fabrication process to spin coat the structural polymer over silicon substrate to achieve a desired thickness of the upper and lower polymer layers of the pressure sensor. The thickness largely depended on viscosity and the spin curve which is a rotational frequency dependent layer thickness (22). In a typical spin curve for PDMS the relation between the thickness and rotational frequency is hyperbolic which typically indicates that a thicker layer will result with small RPM (Revolution per minute) and a thinner layer will result through higher rotational frequency (22). The spin curve of RV 615 and Sylgard 184 is illustrated in the Figure 52 below.

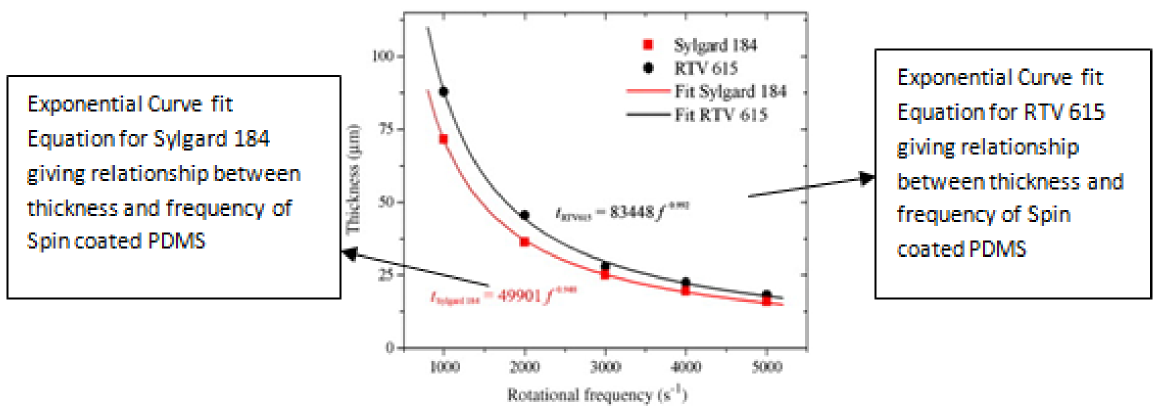

Figure 52: The exponential curve fit of Thickness Vs frequency of two PDMS silicone polymer; image modified from (22)

The dielectric constant of PDMS ranges from 2.3-2.8 (26). So compared with same dimension of two parallel plates with same gap distance PDMS would generate more capacitance compare to air (25) if it was filled as dielectric material in between the parallel plates since the dielectric constant of air is 1 (25). The Poisson's ratio and tensile (fracture) strength for standard PDMS was found in (26) as 0.5 and 2.24 MPa respectively.

Polyimide

Polyimide is another widely used material in micro-electronics fabrication originally developed by the DuPont chemical company in 1950's as high temperature polymers (commercially known as kapton polyimide)(30) used as multilevel interconnect technologies and flexible circuit board substrates due to its various attractive properties (27) like biocompatibility, electrical insulation, thermal stability and magnetic permeability (27). It offers a low residual structural stress and offers a dynamic Microsystems fabrication due to its durability (27). Polyimide films (Abbreviated PI) are also used on wafers as passivation layers, stress buffer layers, dry etch masks, structural layers and re-distribution layers for chip scale and wafer level packaging (28). Polyimide films are cured at very high temperature (350-400^{o}C) to ensure proper mechanical and electrical properties (28). Polyimide film deposition can be done by conventional micro-fabrication techniques like spin coating method and curing at 300^{o}C in nitrogen atmosphere for certain amount of time (27). The tensile stress-strain relationship of polyimide film is given in Figure 53:

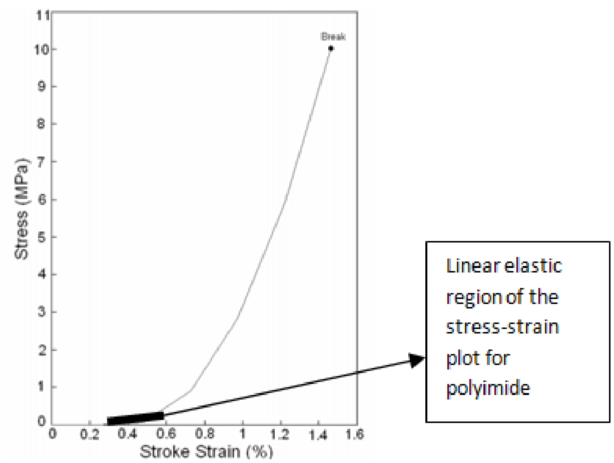

Figure 53: Stress Vs Strain plot of polyimide(containing m-catenatedphenylene rings) tensile test (29); image modified from (29)

The elastic modulus from the above stress-strain diagram for polyimide film received was 1.46 GPa with tensile strength of 10.02 MPa (29). The mechanical properties found for polyimide from the original manufacturer of this product is given below:

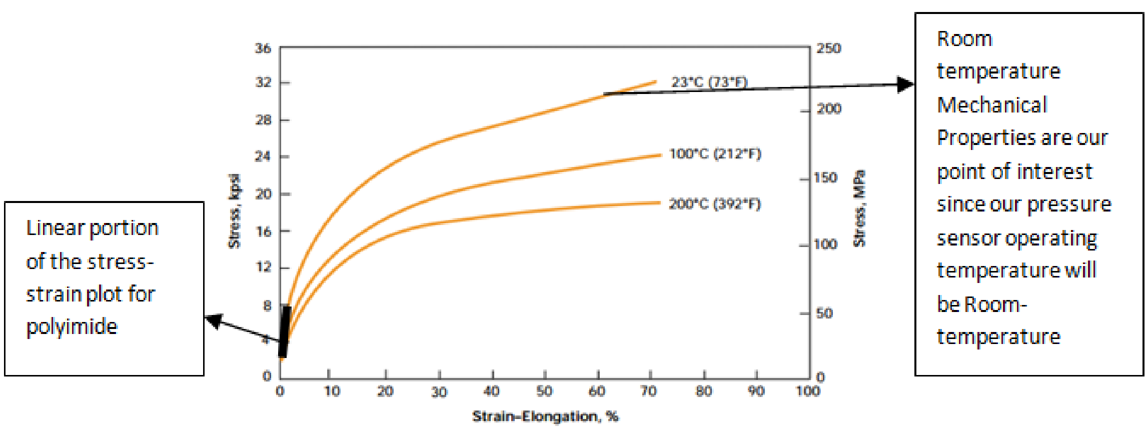

Figure 54: Stress-strain Diagram of Dupont kapton polyimide from the data sheet of original manufacturer (31); image modified from (31)

From the above stress-strain diagram for Dupont Kapton polyimide it can observed that the linear portion of the diagram is situated within the range of approximately 2% mechanical strain and the rest of the region is quite non linear. But the stress-strain plot will stay linear within 0-6 MPa as evident from Figure 54 which is conveniently within the operating range of the pressure sensor which is 0.463-0.5 MPa. The modulus of elasticity from the manufacturer data could be found as 2.5 GPa (at 23 ^{o}C) (31) and yield strength of 231 MPa (at 23^{o}C) with Poisson's ratio of 0.34 (at 23^{o}C) (31). The dielectric constant for kapton polyimide of thickness ranging from 75-125 μm was found to be 3.5 (31). Polyimide film thickness could be easily controlled during micro-fabrication process by controlling speed of the spin chuck and time according to manufacturer (Dupont) specifications found in (32).

Sample calculation of Sensitivity of the sensor with PDMS as structural and insulation Material:

From equation 4 of Parallel plate capacitors: capacitance C is given by

$$C = \varepsilon_o \cdot \varepsilon_r \cdot \frac{A}{d}$$

Where C is capacitance in the parallel plate capacitor, ϵo is permittivity of free space (vacuum); ϵ_o = 8.854 picoFarad/meter; and ϵ_r is the relative permittivity of the dielectric medium (5).

In our pressure sensor, Overlapped area between the parallel plates, A= (200X200) μm^2 = 40000 μm^2, Initial Gap d_o = 12 μm, relative permittivity for PDMS as dielectric medium, ϵ_r = 2.8, for initial gap of d_o, Initial Capacitance,

$C_o= \epsilon_o \epsilon_r A/d_o = (8.854*10^{-12}$ Farad)* 2.8* (40000*10^{-12} meter^2)/ (12*10^{-6} meter)

= $(8.263*10^{-14})$ Farad

= 82.63 femtoFarad

For PDMS polymer, Average Elastic Modulus, E = 1760 kPa with an initial knee pressure of 34.474 kPa; Linear Strain, $\varepsilon = (\sigma/E) = (34.474/1760) = 0.0195875$

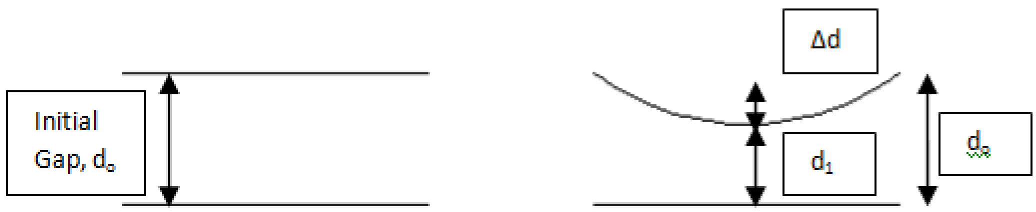

Figure 55: Change of Capacitance in a Parallel Plate capacitor

As a result, Change of Gap between the parallel plates after applied pressure of 34.474 kPa, $d_1= d_o-\Delta d=12-(12*\varepsilon) =11.764$

So, final capacitance after the applied pressure of 34.4745 kPa, C1= $(8.854*10^{-12}$ Farad/meter)* 2.8* $(40000*10^{-12}$ meter^2)/ $(11.764*10^{-6}$ meter)

=84.295 femtoFarad

So, Change of capacitance, $\Delta C = C_1- C_o = 1.665$ femtoFarad.

The sensitivity of the sensor was calculated using Equation 5 found in (5) :

$$V_o = \frac{\Delta C}{2 \cdot (2 \cdot C + \Delta C)} \cdot V_{in} \qquad \text{Equation 5}$$

Where V_{in} is a constant supplied voltage and Vo is output voltage corresponding to the change of capacitances, C is a known capacitance value and ΔC is the change of capacitance in the micro-pressure sensor. In this way the theoretical change of capacitances with respect to our applied range of pressure from 34.474 kPa to 463.543

kPa was calculated to observe sensitivity of the sensor (V_o/V_{in}) and for both PDMS and Polyimide as structural material and tabulated the data in Table 5 and 6 and graphs in Figure 57 to 61.

Table 5: Calculation of Change of Capacitance and Sensitivity of the Sensor for PDMS

Dielectric Material Name	Young's Modulus(Kpa),	Relative Permittivity(ϵ_r)	Initial Gap d_o(μm)	Projected Plate area(μm^2)	Applied Knee Pressure (KPa)	Permittivity in vacuum,ϵ_0	Initial Capacitance(C_o) (FemtoFarad)	Strains in PDMS, ε	Gap after applied stress,d_1(μm)	Final Capacitance(C1)(FemtoFarad)	Change of capacitance(C_1-C_o)(FemtoFarad)	Voltage Ratio V_0/V_{in}
	1.76E+03	2.8	12	40000	34.474	8.85E-12	82.6373	0.0196	11.7650	84.2883	1.6510	0.0050
	1.76E+03	2.8	12	40000	45.765	8.85E-12	82.6373	0.0260	11.6880	84.8435	2.2062	0.0066
	1.76E+03	2.8	12	40000	48.776	8.85E-12	82.6373	0.0277	11.6674	84.9928	2.3555	0.0070
	1.76E+03	2.8	12	40000	55.927	8.85E-12	82.6373	0.0318	11.6187	85.3495	2.7121	0.0081
	1.76E+03	2.8	12	40000	57.056	8.85E-12	82.6373	0.0324	11.6110	85.4061	2.7687	0.0082
	1.76E+03	2.8	12	40000	63.078	8.85E-12	82.6373	0.0358	11.5699	85.7092	3.0718	0.0091
	1.76E+03	2.8	12	40000	68.348	8.85E-12	82.6373	0.0388	11.5340	85.9761	3.3388	0.0099
	1.76E+03	2.8	12	40000	77.381	8.85E-12	82.6373	0.0440	11.4724	86.4377	3.8003	0.0112
	1.76E+03	2.8	12	40000	79.639	8.85E-12	82.6373	0.0452	11.4570	86.5538	3.9165	0.0116
	1.76E+03	2.8	12	40000	90.930	8.85E-12	82.6373	0.0517	11.3800	87.1394	4.5020	0.0133
	1.76E+03	2.8	12	40000	98.834	8.85E-12	82.6373	0.0562	11.3261	87.5540	4.9167	0.0144
	1.76E+03	2.8	12	40000	102.221	8.85E-12	82.6373	0.0581	11.3030	87.7329	5.0956	0.0150
	1.76E+03	2.8	12	40000	105.985	8.85E-12	82.6373	0.0602	11.2774	87.9325	5.2952	0.0155
	1.76E+03	2.8	12	40000	113.513	8.85E-12	82.6373	0.0645	11.2261	88.3345	5.6972	0.0167
	1.76E+03	2.8	12	40000	120.287	8.85E-12	82.6373	0.0683	11.1799	88.6995	6.0622	0.0177
	1.76E+03	2.8	12	40000	124.804	8.85E-12	82.6373	0.0709	11.1491	88.9445	6.3072	0.0184
	1.76E+03	2.8	12	40000	134.590	8.85E-12	82.6373	0.0765	11.0823	89.4800	6.8427	0.0199
	1.76E+03	2.8	12	40000	136.095	8.85E-12	82.6373	0.0773	11.0721	89.5630	6.9256	0.0201

	Table 5 Continued											
PDMS	1.76E+03	2.8	12	40000	141.741	8.85E-12	82.6373	0.0805	11.0336	89.8754	7.2381	0.0210
	1.76E+03	2.8	12	40000	147.386	8.85E-12	82.6373	0.0837	10.9951	90.1901	7.5527	0.0219
	1.76E+03	2.8	12	40000	148.892	8.85E-12	82.6373	0.0846	10.9848	90.2743	7.6370	0.0221
	1.76E+03	2.8	12	40000	163.194	8.85E-12	82.6373	0.0927	10.8873	91.0829	8.4456	0.0243
	1.76E+03	2.8	12	40000	177.496	8.85E-12	82.6373	0.1010	10.7898	91.9061	9.2688	0.0266
	1.76E+03	2.8	12	40000	184.648	8.85E-12	82.6373	0.1050	10.7410	92.3233	9.6860	0.0277
	1.76E+03	2.8	12	40000	206.101	8.85E-12	82.6373	0.1170	10.5948	93.5979	10.9606	0.0311
	1.76E+03	2.8	12	40000	227.554	8.85E-12	82.6373	0.1290	10.4485	94.9082	12.2709	0.0346
	1.76E+03	2.8	12	40000	249.008	8.85E-12	82.6373	0.1410	10.3022	96.2558	13.6184	0.0381
	1.76E+03	2.8	12	40000	291.915	8.85E-12	82.6373	0.1660	10.0097	99.0690	16.4316	0.0452
	1.76E+03	2.8	12	40000	334.821	8.85E-12	82.6373	0.1900	9.7171	102.0516	19.4142	0.0526
	1.76E+03	2.8	12	40000	377.728	8.85E-12	82.6373	0.2150	9.4246	105.2193	22.5820	0.0601
	1.76E+03	2.8	12	40000	420.635	8.85E-12	82.6373	0.2390	9.1320	108.5901	25.9527	0.0679
	1.76E+03	2.8	12	40000	463.542	8.85E-12	82.6373	0.2630	8.8395	112.1839	29.5465	0.0758

Table 6: Calculation of Change of Capacitance and Sensitivity of the Sensor For Polyimide

Dielectric Material Name	Young's Modulus(Kpa), PDMS	Relative Permittivity(εr)	Initial Gap do(μm)	Projected Plate area(μm2)	Applied Knee Pressure (Kpa)	Permittivity in vacuum,ε0 (Farad/meter)	Initial Capacitance(Co) (FemtoFarad)	Strains in PDMS, ε	Gap after applied stress,d1(μm)	Final Capacitance(C1)(FemtoFarad)	Change of capacitance(C1-Co)(FemtoFarad)	Voltage Ratio V0/Vin
	2.50E+06	3.5	12	40000	34.474	8.85E-12	103.29667	1.38E-05	11.99983453	103.29809	0.00142	0.0000034
	2.50E+06	3.5	12	40000	45.765	8.85E-12	103.29667	1.83E-05	11.99978033	103.29856	0.00189	0.0000046
	2.50E+0	3.5	12	40000	48.776	8.85E-12	103.29667	1.95E-05	11.99976587	103.29868	0.00202	0.0000049

	Table 6 Continued											
	2.50E+06	3.5	12	40000	55.927	8.85E-12	103.29667	2.24E-05	11.99973155	103.29898	0.00231	0.0000056
	2.50E+06	3.5	12	40000	57.056	8.85E-12	103.29667	2.28E-05	11.99972613	103.29902	0.00236	0.0000057
	2.50E+06	3.5	12	40000	63.078	8.85E-12	103.29667	2.52E-05	11.99969722	103.29927	0.00261	0.0000063
	2.50E+06	3.5	12	40000	68.348	8.85E-12	103.29667	2.73E-05	11.99967193	103.29949	0.00282	0.0000068
	2.50E+06	3.5	12	40000	77.381	8.85E-12	103.29667	3.10E-05	11.99962857	103.29986	0.00320	0.0000077
	2.50E+06	3.5	12	40000	79.639	8.85E-12	103.29667	3.19E-05	11.99961773	103.29996	0.00329	0.0000080
	2.50E+06	3.5	12	40000	90.930	8.85E-12	103.29667	3.64E-05	11.99956354	103.30042	0.00376	0.0000091
	2.50E+06	3.5	12	40000	98.834	8.85E-12	103.29667	3.95E-05	11.99952560	103.30075	0.00408	0.0000099
	2.50E+06	3.5	12	40000	102.221	8.85E-12	103.29667	4.09E-05	11.99950934	103.30089	0.00422	0.0000102
	2.50E+06	3.5	12	40000	105.985	8.85E-12	103.29667	4.24E-05	11.99949127	103.30105	0.00438	0.0000106
	2.50E+06	3.5	12	40000	113.513	8.85E-12	103.29667	4.54E-05	11.99945514	103.30136	0.00469	0.0000114
	2.50E+06	3.5	12	40000	120.287	8.85E-12	103.29667	4.81E-05	11.99942262	103.30164	0.00497	0.0000120
	2.50E+06	3.5	12	40000	124.804	8.85E-12	103.29667	4.99E-05	11.99940094	103.30182	0.00516	0.0000125
	2.50E+06	3.5	12	40000	134.590	8.85E-12	103.29667	5.38E-05	11.99935397	103.30223	0.00556	0.0000135
	2.50E+06	3.5	12	40000	136.095	8.85E-12	103.29667	5.44E-05	11.99934674	103.30229	0.00562	0.0000136
	2.50E+06	3.5	12	40000	141.741	8.85E-12	103.29667	5.67E-05	11.99931964	103.30252	0.00586	0.0000142
Polyim	2.50E+06	3.5	12	40000	147.386	8.85E-12	103.29667	5.90E-05	11.99929255	103.30276	0.00609	0.0000147

ide	Table 6 Continued											
	2.50E+06	3.5	12	40000	148.892	8.85E-12	103.29667	5.96E-05	11.99928532	103.30282	0.00615	0.0000149
	2.50E+06	3.5	12	40000	163.194	8.85E-12	103.29667	6.53E-05	11.99921667	103.30341	0.00674	0.0000163
	2.50E+06	3.5	12	40000	177.496	8.85E-12	103.29667	7.10E-05	11.99914802	103.30400	0.00733	0.0000178
	2.50E+06	3.5	12	40000	184.648	8.85E-12	103.29667	7.39E-05	11.99911369	103.30430	0.00763	0.0000185
	2.50E+06	3.5	12	40000	206.101	8.85E-12	103.29667	8.24E-05	11.99901072	103.30518	0.00852	0.0000206
	2.50E+06	3.5	12	40000	227.554	8.85E-12	103.29667	9.10E-05	11.99890774	103.30607	0.00940	0.0000228
	2.50E+06	3.5	12	40000	249.008	8.85E-12	103.29667	9.96E-05	11.99880476	103.30696	0.01029	0.0000249
	2.50E+06	3.5	12	40000	291.915	8.85E-12	103.29667	1.17E-04	11.99859881	103.30873	0.01206	0.0000292
	2.50E+06	3.5	12	40000	334.821	8.85E-12	103.29667	1.34E-04	11.99839286	103.31050	0.01384	0.0000335
	2.50E+06	3.5	12	40000	377.728	8.85E-12	103.29667	1.51E-04	11.99818690	103.31228	0.01561	0.0000378
	2.50E+06	3.5	12	40000	420.635	8.85E-12	103.29667	1.68E-04	11.99798095	103.31405	0.01738	0.0000421
	2.50E+06	3.5	12	40000	463.542	8.85E-12	103.29667	1.85E-04	11.99777500	103.31582	0.01916	0.0000464

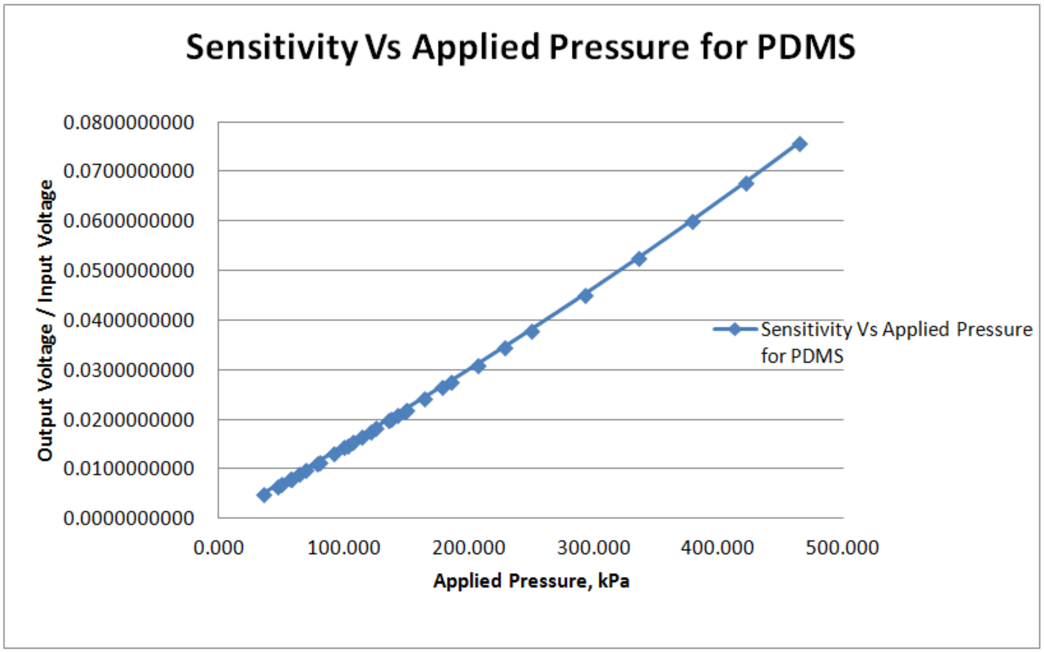

Figure 56: Plot of Sensitivity Vs Applied Pressure; Material PDMS

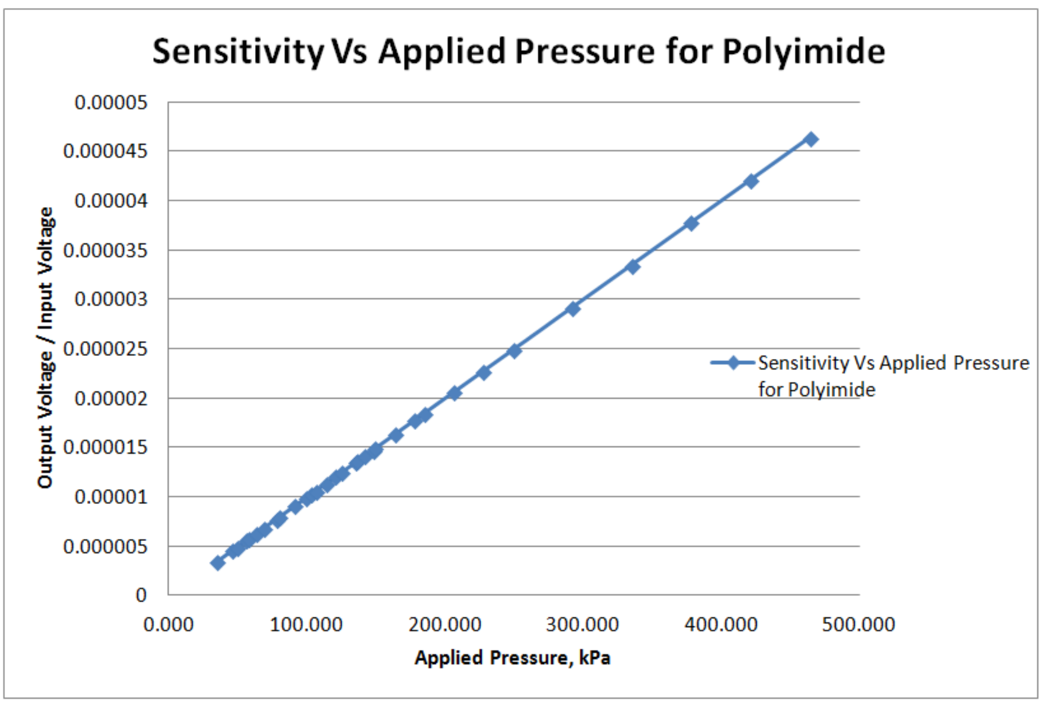

Figure 57: Plot of Sensitivity Vs Applied Pressure; Material Polyimide

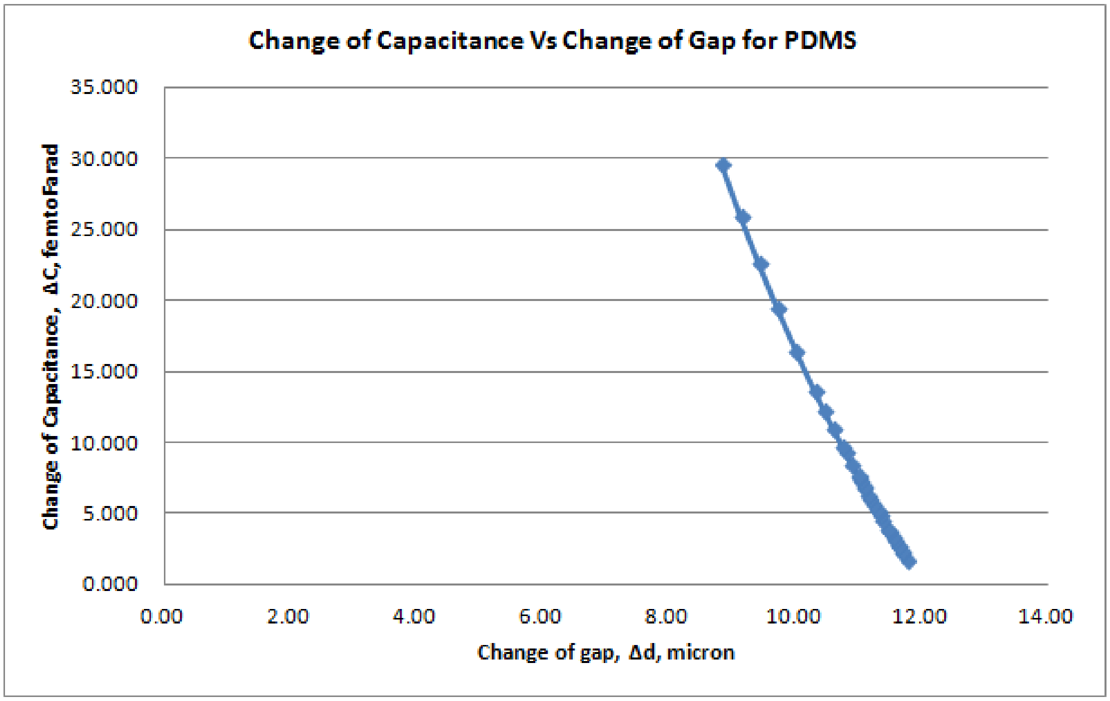

Figure 58: of Change of Capacitance Vs Change of Gaps; Material PDMS

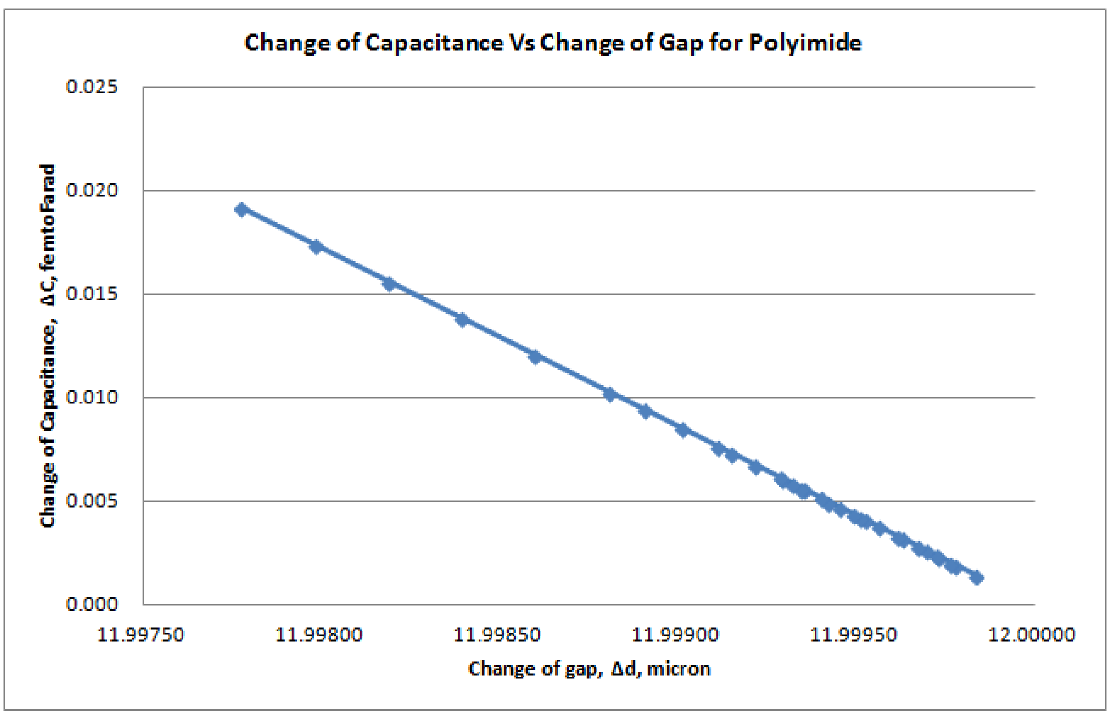

Figure 59: Plot of Change of Capacitance Vs Change of Gaps; Material Polyimide

Relative Comparison of the Sensitivity and Change of Capacitance

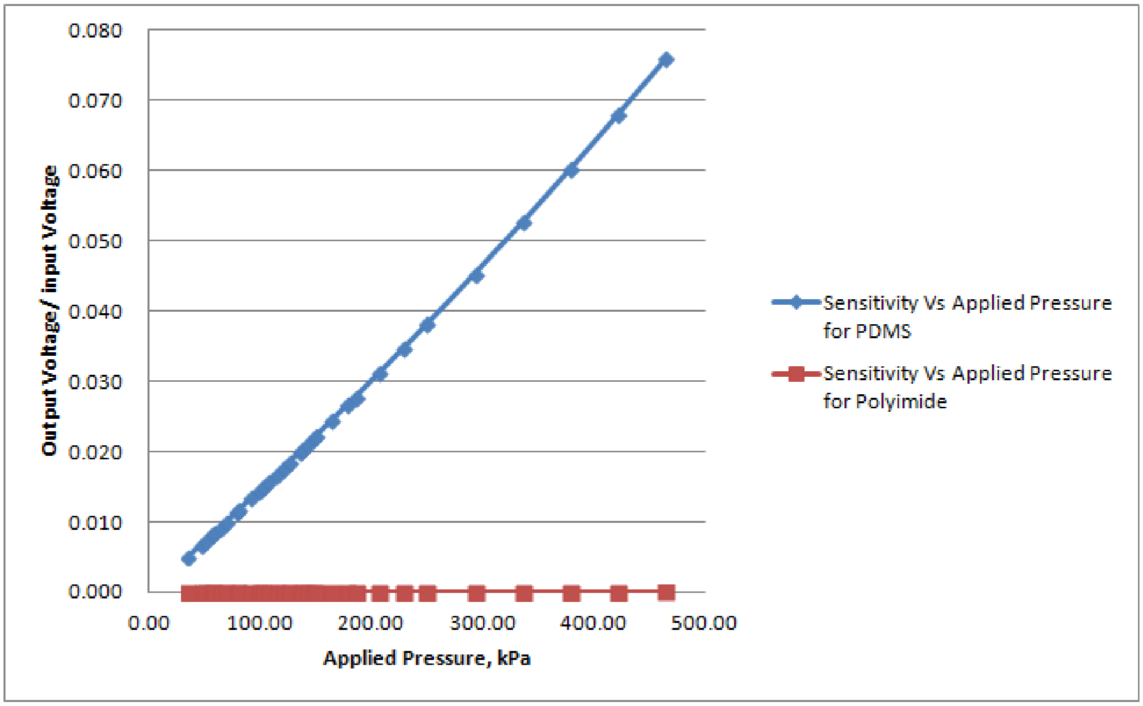

Figure 60: Sensitivity Vs Applied Pressure; Material PDMS and Polyimide

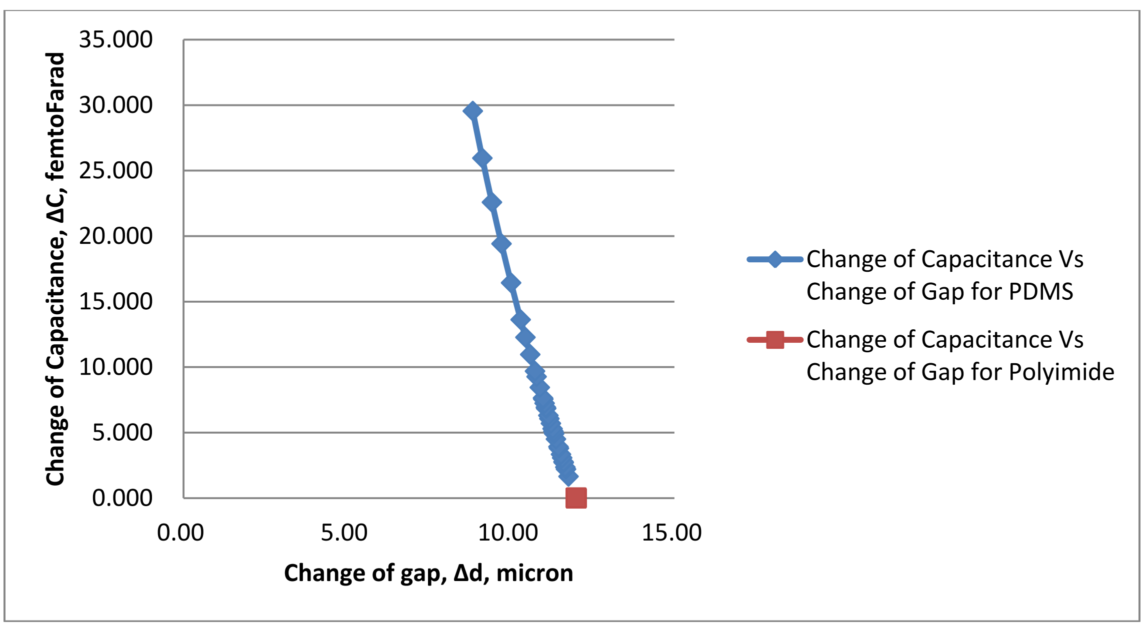

Figure 61: Change of Capacitance Vs Change of Gap; Material PDMS and Polyimide

From Figure 56 and 57 plots we can clearly see the sensitivity of the sensor increases almost linearly as the applied contact pressure rises inside the knee joint for both PDMS and polyimide as structural material. On the other hand from Figure 58 and 59 we can observe that the change of capacitance is going down as the gap between the parallel plate capacitors increases or in other words the change of capacitance increases as the gap between the parallel plates decreases with the applied pressure which is evident from Equation 4 where the capacitance is inversely proportional to the gap between the parallel plates. From figure: 60 and 61 we can see a relative comparison of sensitivity and change of capacitance of PDMS and polyimide. PDMS results in a more responsive capacitive sensor system compare to Polyimide where the magnitude of sensitivity was about 1648 times higher in PDMS than polyimide for an applied pressure of 463.54 kPa. The similar thing happened in case of change of capacitance which was 1541 times higher in PDMS than Polyimide. This was obvious since the stiffness of the polyimide was 1420 times higher than that of PDMS so PDMS resulted in a more flexible behavior than Polyimide. So for better structural integrity, rigidity and robustness polyimide would be a better structural material and on the other hand for greater flexibility, sensitivity and ease of fabrication PDMS will be a good selection as both dielectric and embedding substrate for the micro-pressure sensor.

Electrode Material

Gold and copper are most commonly used metallization materials in micro-electro fabrication process. Selection of metal type as electrode materials would solely depend on structural integrity, fracture/ micro crack resistance, higher yield point, electrical conductivity, ease of fabrication and better bonding/adhesion with the polymer substrate. For the capacitive type pressure sensors the sensitivity of the sensor would purely depend on the distance between the parallel plates and the overlapped area between the plates but not on their strength or conductivity. As the fabrication process established in earlier chapters, the metallization would be performed on the silicon wafer but not on the polymer substrates so it was not a matter of concern about bonding technique between the polymer materials and metal layers since the adhesion would be purely due to mechanically applied force and surface tension of the visco-elastic material when PDMS or Polyimide would be spin casted over the gold/copper metal layers. A metal layer thickness of 5-20 microns would be considered for the micro-pressure sensor. During the comparison and selection process of metals as electrode materials, it would be based on finite element analysis and stress analysis of the sensor within the operating pressure range of the sensor.

STRUCTURAL ANALYSIS

The primary objective of structural analysis is to ensure the structural integrity and reliability of Microsystems when they will be subjected to specific loading conditions at both normal and abrupt operating conditions (5). The micro pressure sensor for knee contact stress distribution would be subjected to bending load as well as surface contact pressure inside the tibiofemoral interface of mouse knee joint. Since the pressure sensor consisted of layers of polymers, thin films of metals, insulation layers and interconnection terminals, the stress concentrations inside the sensor at any points were analyzed if it would exceed the yield point of any of the constituent material. Finite element analysis (FEA) is an effective tool to analyze stress distribution, thermal stress concentration, fatigue and directional strain in different types of structures. FEA was utilized to determine optimal thickness of the polymer membranes, insulation layers and metal electrodes, to assure that there would be no plastic deformation occurring during the operation of the sensor and selection of the effective material as structural membrane and metal electrodes for the sensor.

Finite Element Analysis

Commercially available FEA software *ANSYS Workbench 14.0* was used to analyze the three dimensional computer assisted design model (CAD) of the micro-pressure sensor and *ANSYS Mechanical APDL 14.0* was used for a structural 2D analysis of the pressure sensor. The CAD models that had been used for the analysis was the model that had resulted from the third and final iteration of the design attempt for the sensor. Analyses were also performed on a PDMS embedded sensor with polyimide as the insulation/dielectric material to observe how it affected the overall strength of the structure. All the analyses were performed assuming linear elastic properties of the constituent material since it was evident from the material characteristics stress-strain curve of PDMS and polyimide that they would retain their elasticity within the actual operating pressure range of the sensor. Gold and copper were considered both as metal electrodes material.

<u>Properties Used for PDMS</u>

Modulus of Elasticity = 700 kPa (26)

Poisson's Ratio=0.5 (26)

Tensile Yield strength= 2.24 MPa (26)

<u>Properties Used for Polyimide</u>

Modulus of Elasticity=2.5 GPa (at 23 oC) (31)

Poisson's Ratio= 0.34 (at 23 oC) (31)

Tensile Yield strength= 231 MPa (31)

<u>Properties Used for Gold</u>

Modulus of Elasticity= 79 GPa (33)

Poisson's Ratio= 0.42 (33)

Tensile Yield Strength= 127 MPa (33)

Properties Used for Copper

Modulus of Elasticity= 110 GPa (34)

Poisson's Ratio= 0.34 (34)

Tensile Yield Strength= 252.3 MPa (34)

Properties of Tibia (bone material)

Modulus of Elasticity= 2GPa (Assumed)

Poisson's Ratio= 0.3 (Assumed)

Design Modeler Setup

The geometry of the pressure-sensor was built using the *ANSYS Workbench Design Modeler* which was the solid modeling section of *ANSYS*. Later the 3D model was converted and imported as *SolidWorks* assembly drawing for the convenience and ease of modification of the model geometry. During finite element analysis of the sensor the part of the sensor which contained the capacitive sensor arrays was analyzed only (1.2 by 4 mm rectangular area) and the rest of the geometry containing the interconnecting terminals and connection pads were omitted for the simplicity of analysis by using extruded plane cut feature of *SolidWorks*. After the necessary modification had been done, later the drawing file was imported back to *ANSYS Design Modeler* interface without any technical problem. The final geometry of the model consisted of a curved tibial bone support and the sensor assembly was resting on both end of the tibia as shown in Figure 62, In-order to simulate the flexing and surface pressure loading on the sensor close to the actual scenario. In the simulation the maximum depth of tibial curvature was assumed to be 1mm. So when surface load would be applied on the pressure sensor, the maximum deflection of this simply supported structure should not exceed beyond inner surface of the tibia which was at 1mm distance from the bottom surface of the pressure sensor in no load condition. The curved tibial support was built to provide a fixed/rigid support for the structure and restricted from rigid body motion. The properties of the tibia were assumed to have a stiffness of 2 GPa with poisons ratio of 0.3. The actual cartilage of tibia had much lower stiffness of 76-122 MPa (35) but the fixed rigid support was intended not to be deformed and provide a fixed support at the bottom for the time being to concentrate the analysis on the sensor assembly only to observe its deformation pattern. Once the full model was successfully imported back to *ANSYS Design Modeler* a symmetric cut of the model was taken to work with a half model of the drawing. The symmetric plane was applied for various reasons: To reduce number of nodes and elements while they would be generated during meshing operation since the educational license of *ANSYS Workbench* has a node limitation of 200,000. Other reasons were to reduce computation time and complexity of the analysis due to multiple layers of materials, different contact surfaces and bonding types. The half model analysis would exactly reduce the computation time by 50 percent compared to that of the full model and it would be possible to run the analysis within the specified node limitation of the software for academic license.

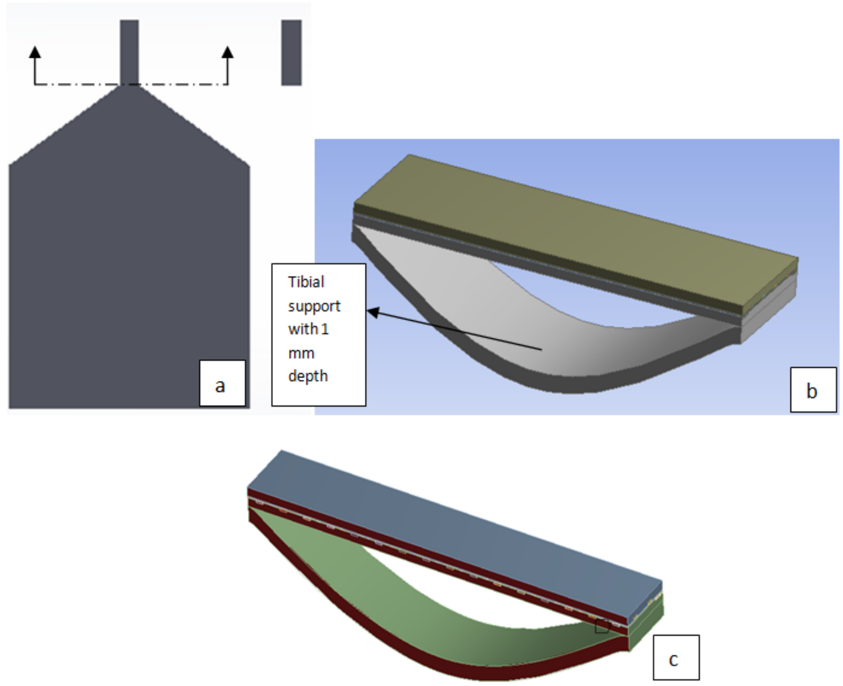

Figure 62: a) Extruded Cut operation of the model in *SolidWorks* b) Imported geometry in *ANSYS Design Modeler* c) half geometry with plane of symmetry (red color)

Static Structural Analysis Settings

After the material properties were properly defined in the preprocessor and the model was finalized in *Design Modeler* module then the design was updated in Mechanical application of *Workbench*. The *Workbench Mechanical* auto selected several hundred default contact regions immediately the model was updated from *Design Modeler*. Most of the automatic contacts were redundant and unnecessary as well as inaccurately defined. As a result the auto generated contacts were removed from the model and connections of different faces and layers were manually defined. The detailed descriptions of the different connections are given below. Before describing the various connections made within the model, the concepts of defining contact and target surfaces and their bonding types are described below.

Defining Contact and Target Surfaces

The contact elements are constrained from penetrating the target elements but target elements can penetrate through the contact surface (36). When the connection is between a rigid and flexible surface, the target surface should always be the rigid surface and the contact surface is generally the one which is deformable (36). A general rule of thumb is that the stiffer surface should be defined as target and the softer surface should be defined as contact surface (36). During the solution *Workbench* will check the status of the contact for each point (typically a node or an integration point) on the contact faces against the target faces (37). Once the target and contact surfaces are defined the contact type needs to be defined as either symmetric or asymmetric. Asymmetric contacts are defined as having all contact elements on one surface and target elements on the other surface and sometimes known as “One-pass contact” (36). On the other hand if each surface is defined to be both a target and a contact then two sets of contact pairs could be generated between the contacting surfaces (36). This is known as symmetric contact or two-pass contact (36). If the behavior type is selected as Symmetric then *Workbench* will check the status of each point on contact surface against each point on target surface and vice versa (37). But if the behavior type is set to Asymmetric then the checking will be only one sided and in that case the proper selection of contact and target becomes important (37). Symmetric contacts are usually selected if the distinction between the contact and target is unclear and if both surfaces have vey coarse mesh. If the meshes on the both surfaces are refined sufficiently and identical then asymmetric contact algorithm will significantly improve the performance of the solution (36). Basically two types of contacts were defined during the pressure sensor analysis which was “Bonded” and “Frictionless”. When two faces are in bonded contact they are coupled with each other in both tangential and normal direction and no contact nonlinearities occur (37). On the other hand frictionless contact faces are free to separate in their normal direction and slide in their tangential direction without the absence of any frictional forces and it introduces non-linearity (37).

Contact Region 1 and 2

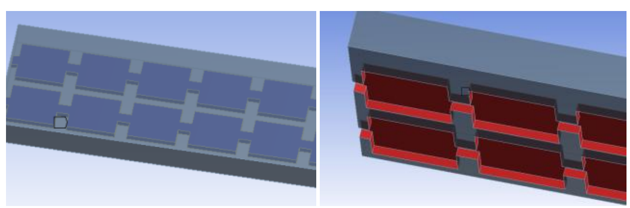

Figure 63: Bonded contact between 2 (due to symmetry plane) Upper Electrodes (blue) and Upper Polymer layer (red)

256 faces of upper electrodes (highlighted in blue color) were defined as target faces with bonded contact to 256 contact faces of inner grooves in the polymer shown in Figure 63. Similarly 296 faces of lower electrodes (In blue color) were defined as target faces assuming perfectly bonded to 296 contact faces of inner groves inside lower polymer layer shown in Figure 64.

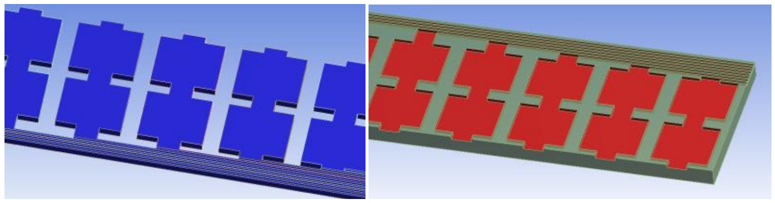

Figure 64: Bonded contact between 16 lower Electrodes (blue) and Lower Polymer layer (red grooves)

In both upper and lower electrodes the bonding were defined as "program controlled" by *Workbench* so that the program itself would select the best contact behavior between the surfaces. Since the quality of the mesh on both surfaces was kept coarse to reduce computation time at the beginning, Symmetric behavior was also used in the later analyses with these connections which resulted in good convergence of the solution.

Contact Region 3 and 4

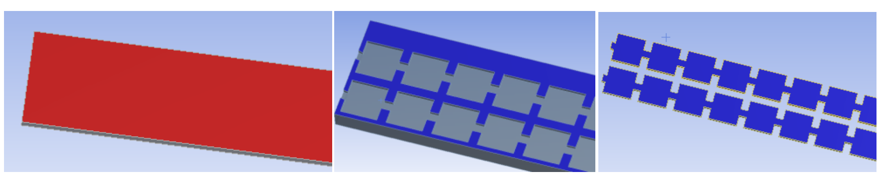

Figure 65: Bonded contact between thin insulation layer of polymer (Red) and three faces in the Upper Polymer Layer (Blue)

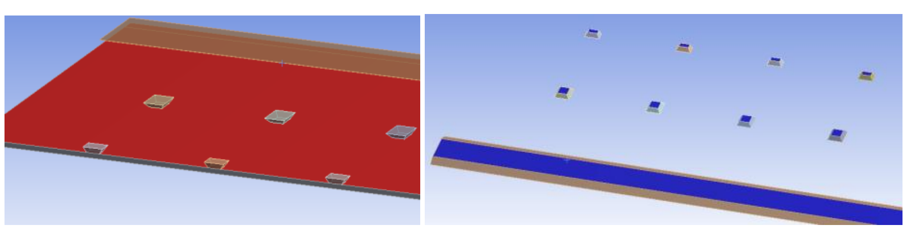

Figure 66: Bonded contact between thin insulation layer of polymer (Red) and surfaces of bumps (Blue)

A thin insulation layer of polymer was designed in the original sensor to act as a dielectric medium for the capacitive sensors. It was placed in between the upper and lower electrodes where the upper electrodes as well as upper Polymer surface were in contact with the insulation layer on one side (Figure 65) and the faces of the bumps protruding from lower PDMS layer were in contact with the insulation layer on the other side (Figure 66). Bonded contacts were defined in both cases of connection and the contacts were defined as perfectly bonded so that the layers will not experience any separation or rigid body motion within each other and the contact behavior was again selected as program controlled by *Workbench*.

Contact Region 5 and 6

Since one side of the small bumps and the continuous bump was connected to the face of thin insulation layer the other side of the bumps (blue) were assumed perfectly bonded with lower Polymer layer (red) as shown in Figure 67. The figures are flipped to show the mating surfaces in two different colors of blue and red respectively. Once again the bonded behavior was left to "Program controlled". It is safe to assume a perfect bonding between the faces since both of the layers are made of similar type of polymers.

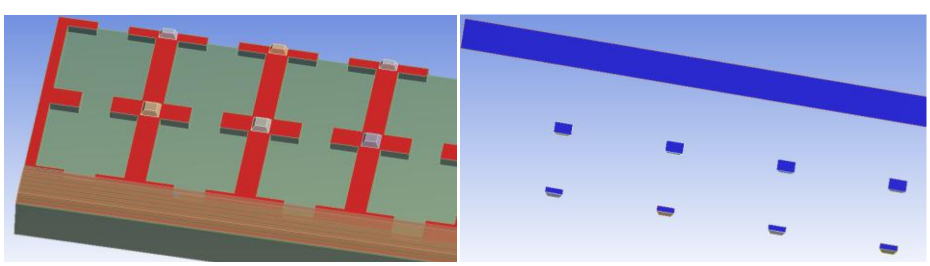

Figure 67: Bonded contact between lower polymer face (red) and bumps layer (blue)

The final contact pair was defined between the bottom surface of lower polymer layer and the upper surface of the tibia as shown in Figure 68.

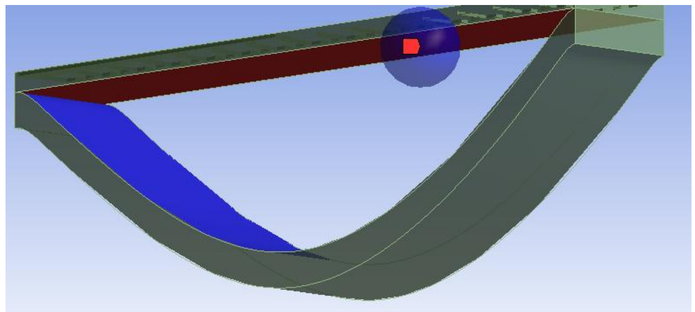

Figure 68: Frictionless contact pair between lower polymer layer (red) and tibial support (blue) with pinball region

The lower polymer layer was resting at two end of the curved support at the two edges about 1mm above the inner surface of the curved support. When the structure would be under surface pressure the polymer layer is predicted to bend and began to touch the curved surface. As a result the contact between the pair was defined as frictionless. The rigid tibial support was defined as target surface and relatively softer lower polymer layer was defined as contact surface. A pinball region of 0.2mm radius was defined for this particular frictionless contact. A contact element was considered to be in near-field contact when its integration points (gauss points or nodal points) were within a program defined or user defined distance to the corresponding target surface and that distance was defined as Pinball Region (36). The 0.2mm sphere was indicating the pinball region which would start calculating for the status of contact elements of the whole polymer contact surface (red) as soon as the sphere was about to touch the target elements. If the radius of the pinball was set too large it would immediately start the contact algorithm which would be computationally expensive since the near-field calculations (for contact elements that were nearly or actually in contact) were usually slower and more complex (36). The most complex calculation would begin when the contact and target elements were actually in contact (36).

The Augmented lagrange formulation was used as the contact formulation of the above frictionless contact and for the rest of the bonded contacts it was left as program controlled in *Workbench*. These formulations were to ensure contact compatibility i.e. to prevent the penetration of the contacting point into the target faces (37). Whenever a contacting point penetrated a target face by an amount xn it would be pushed back by a normal force Fn which was given by

$$F_n = K_n \cdot X_n \qquad \text{Equation 6}$$

Where k_n is the normal stiffness having no physical meaning other than a numerical parameter for the contact algorithm (37). Higher normal stiffness (k_n) usually results in a less penetration and vice versa (37). In Augmented Lagrange formulation an extra term is added in the above formulation which is,

$$F_n = K_n \cdot X_n + \lambda \qquad \text{Equation 7}$$

Where λ is the contact pressure or also known as Lagrange multiplier (37). Whenever a contact surface is in touch with the target surface the contact pressure λ is being calculated which prevents further penetration. This formulation is less sensitive to normal stiffness Kn because of the contact pressure λ and suitable for general frictional or frictionless contact in large deformation problem (37).

Generation of Mesh

The basic idea of finite element methods is to divide the entire geometric domain into smaller and simpler domains which are known as finite elements (37). These elements are connected to their neighboring elements by nodes (37). The governing equation for each individual element can be established and solved simultaneously by the finite element solver (37). The method of dividing a geometric model into finite number of elements is called meshing or sometimes called finite element meshing (37).

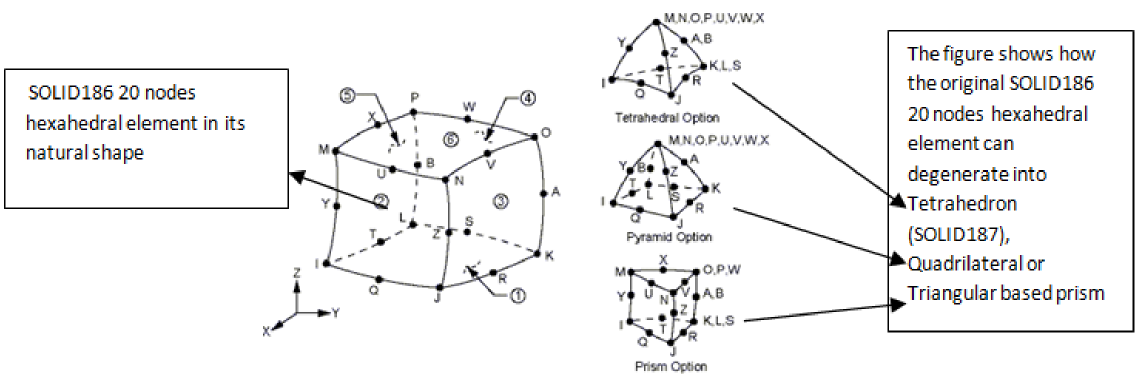

Figure 69: SOLID186 Element type with homogeneous Structural Solid Geometry; Image borrowed from *ANSYS* help documentation

Since *ANSYS Workbench* was used as the FEA modeler and solver it was required to identify what type of elements *Workbench* generated for the 3D solid bodies. For a 3D solid body *Workbench* meshes the geometry with SOLID186 elements which is a 20 node 3D second order structural solid element and it is a hexahedral in its natural shape (37) shown in Figure 69. After deformation the element can degenerate into a triangle based prism, quadrilateral based pyramid or tetrahedron as shown in Figure 69. If a body is specifically meshed with SOLID187 element it is called tetrahedral dominated mesh since that element is a 3D 10 node tetrahedral second order structural solid elements which is a degenerated version of the element SOLID186 (37). *Workbench* has an option to drop midside nodes of the elements which turns the edges of the elements straight (37). Each node of The SOLID186 has three degrees of freedom which are: translations in x,y and z directions (38). The element also supports plasticity, hyper-elasticity, creep, stress stiffening, large deflection and large strain capabilities (38).

The half symmetric model of the sensor was meshed with a combination of SOLID186 and SOLID187 elements in *Workbench*. "Body sizing" control method was used to mesh upper and lower polymer layer and the tibial support at the bottom. An element size of 80 microns was defined for the above mentioned meshing operation of the solid bodies. Next another "body sizing" control of the mesh was defined for small and solid bumps, upper and lower electrodes and the thin insulation layer of polymer. For the bump layer the element size was defined as 20 microns and for the electrodes and insulation layer it was defined as 50 microns and 80 microns respectively.

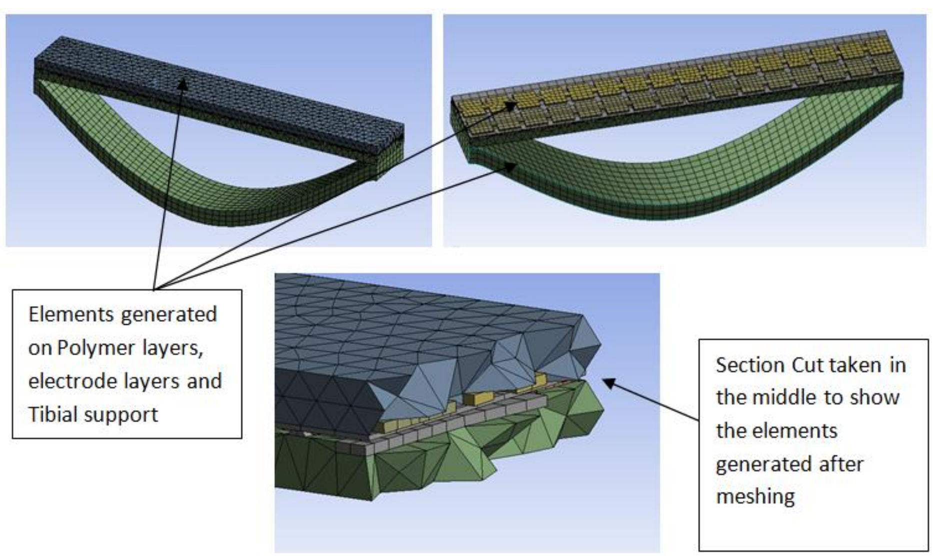

Figure 70 Continued: Mesh Generation

The mesh statistics were: total 66147 nodes and 17784 elements were generated after the meshing operation. The whole mesh elements were a combination of hexahedrons, tetrahedron and quadrilateral elements as shown in Figure 70. which is also evident from the section plane cut view in the middle of the geometry in Figure 70.

Boundary Conditions and Loading Condition

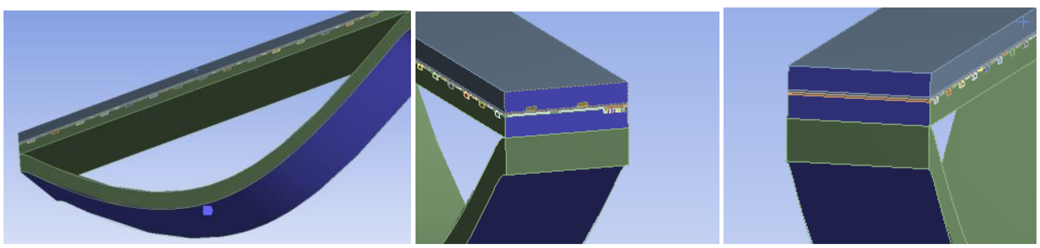

Figure 71: Boundary conditions of the analysis; blue shaded zones were the fixed supports

We assumed simplified boundary conditions for the analysis of the sensor. The bottom of the tibia was set as fixed support as shown in Figure 71 with the blue shaded region. Fixed support meant it was restricted to move along any direction and rotation. Four other faces were defined as fixed support as well which were located opposite to each other and they were along the width side of upper and lower Polymer layer. After the boundary conditions were properly set a surface pressure was applied ranging from 1kPa to 400 kPa depending on the type of polymer material on the top surface of upper polymer layer as indicated by the red shaded region in Figure 72.

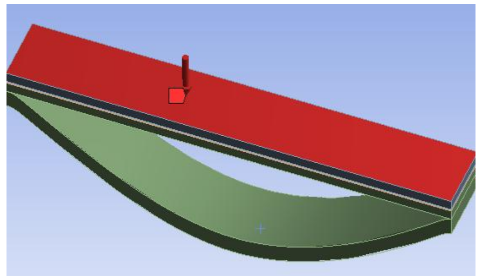

Figure 72: Applying Surface Pressure on top of Polymer

RESULTS AND DISCUSSIONS

A varied range of pressure has been applied over the pressure sensor to observe the structural behavior in terms of total equivalent stress, maximum principal stress, minimum principal stress and maximum shear stress. Basically two loaded condition of the sensor would be discussed. One would be the state where the equivalent stress stayed below the yield point of the metal electrodes and the other state would be where the equivalent (von-mises) stress exceeded the yield point of metal electrodes. In both cases maximum and minimum stress level of each individual polymer layer was observed as well to check whether they exceed their individual material yield point too.

A special failure criterion was utilized to analyze the stress developed in the structure which was Von Mises yield criterion and its relation to the principal stresses. Stress can be expressed as a pair of normal and shear stress (σ,T) at any arbitrary direction. The collections of these stress pairs form a circle in the σ-T space which is known as Mohr's Circle which represents stress state at any given condition (37). The point of maximum normal stress is called maximum principal stress which is located at the right most location of the Mohr's Circle and the point of minimum normal stress is located at the left-most location of the Mohr's Circle which is also known as minimum principal stress (37). The corresponding directions are known as principal directions and there are three principal directions and three principal stresses for a 3D solid (37). The point of maximum and minimum shear stresses is located at the top and bottom of the Mohr's Circle respectively.

The Von Mises yield criterion is generally a commonly used failure criterion in plasticity models for a wide range of materials (38). It is a good first approximation of failure for metals, ductile and polymer materials. The criterion characteristic is isotropic and independent of hydrostatic pressure, which occasionally can limit its applicability to micro-structured materials and materials that exhibit plastic dilatation (38). Before the criterion could be explained it is required to clarify two kinds of stress which are hydrostatic stress and deviatoric stress. The hydrostatic stress (p) is defined as the average of the three principal stresses where

$$p = \frac{(\sigma_1 + \sigma_2 + \sigma_3)}{3} \qquad \text{Equation 8}$$

And the total stress state can be written as,

$$\{\sigma\} = \{\sigma_p\} + \{\sigma_d\} \qquad \text{Equation 9}$$

Where the first part, σ_p is the hydrostatic stress and the second part, σ_d is called deviateric stress which is deviating from the hydrostatic stress (37). Von-Mises proposed a theory for predicting the failure or yielding of ductile material. The theory states that yielding occurs when the deviatic strain energy reaches a critical value which is the yield strength of the corresponding material (37). The criterion can be stated as: yielding occurs when $\sigma_e \geq \sigma_y$ whereσe is the von Mises equivalent stress and σ_y is the yield strength and corresponds to the yield in uniaxial stress loading. Equivalent stress (or von mises stress) is related to the principal stresses by the equation:

$$\sigma_e = \left[\frac{(\sigma_1 - \sigma_2)^2 + (\sigma_2 - \sigma_3)^2 + (\sigma_3 - \sigma_1)^2}{2}\right]^{\frac{1}{2}} \qquad \text{Equation 10}$$

Von Mises found that, even though none of the principal stresses exceeds the yield stress of the material, it is possible for yielding of the material resulting from the combination of stresses. The Von Mises criterion is a formula for combining these 3 stresses into an equivalent stress, which is then compared to the yield stress of the material.

Finite element analyses on the sensor structure were conducted with PDMS and Polyimide as the structural and insulation material, gold as the electrode material and a curved solid body as the tibial support. A linear static structural analysis of the sensor were run assuming all the material properties linear elastic since it was shown that the material properties would stay linear within the operating pressure range of the sensor. It was possible to get a force convergence up to 65 kPa of pressure for PDMS as structural material. Any loading above 65kPa was resulting in a solution of non convergence for PDMS structure. The results were tabulated in the following tables:

Table 7: Results obtained with PDMS and Gold as structural materials

Electrode thickness (mm)	Electrode material	Insulation Material	Applied Surface Pressure (kPa)	Equivalent (Von-mises) Stress (Mpa)	Maximum Principal Stress (Mpa)	Minimum Principal Stress(Mpa)	Maximum Shear Stress (Mpa)	Directional Deformation (z-axis) (mm)
0.02	Gold	PDMS	1	75.663	75.557	14.563	38.438	0.079
0.02	Gold	PDMS	5	368.63	308.13	161.74	203.64	0.2679
0.02	Gold	PDMS	10	921.58	618.92	344.62	529.07	0.4428
0.02	Gold	PDMS	15	1492.7	977.52	520.8	859.21	0.595
0.02	Gold	PDMS	20	1997.9	1287	666.49	1151.3	0.7342
0.02	Gold	PDMS	25	2461.6	1564.7	794.32	1419.3	0.8647
0.02	Gold	PDMS	30	2903.2	1826.2	917.64	1674.4	0.9895
0.02	Gold	PDMS	35	3126.9	1953.4	985.2	1803.7	1.0358

Table 7 Continued									
0.02	Gold	PDMS	40	3260.8	2028.2	1025.3	1881.1	1.043
0.02	Gold	PDMS	45	3388.8	2099.1	1065.3	1955.1	1.049
0.02	Gold	PDMS	50	3502.3	2161.9	1101.1	2020.7	1.053
0.02	Gold	PDMS	55	3605.3	2219.4	1133.5	2080.2	1.058
0.02	Gold	PDMS	60	3697.2	2271.1	1162.6	2133.3	1.061
0.02	Gold	PDMS	65	3782	2319	1189.7	2182.3	1.065

Table 8: Results obtained with PDMS and Copper as structural materials

Electrode thickness (mm)	Electrode material	Insulation Material	Applied Surface Pressure (kPa)	Equivalent (Von-mises) Stress (Mpa)	Maximum Principal Stress (Mpa)	Minimum Principal Stress(Mpa)	Maximum Shear Stress (Mpa)	Directional Deformation (z-axis) (mm)
0.02	Copper	PDMS	1	84.322	83.288	10.893	43.263	0.067
0.02	Copper	PDMS	5	357.82	324.86	151.27	200.05	0.22612
0.02	Copper	PDMS	10	863.34	646.12	354.02	492.66	0.37433
0.02	Copper	PDMS	15	1472	1012.9	541.88	843.82	0.5
0.02	Copper	PDMS	20	2047.1	1387.4	719	1176.2	0.6159
0.02	Copper	PDMS	25	2569.6	1721.2	866.18	1478.4	0.72364
0.02	Copper	PDMS	30	3063.8	2031.5	1008.3	1764.1	0.82623
0.02	Copper	PDMS	35	3539.1	2326.6	1147	2039	0.92534
0.02	Copper	PDMS	40	3975.5	2594.7	1275.9	2291.4	1.0156
0.02	Copper	PDMS	45	4144.3	2690.8	1332.8	2389.2	1.0342
0.02	Copper	PDMS	50	4281.8	2770	1374.6	2468.8	1.0405
0.02	Copper	PDMS	55	4415.4	2845.4	1416.1	2546.1	1.0463
0.02	Copper	PDMS	60	4540.3	2916	1456.7	2618.4	1.0515
0.02	Copper	PDMS	65	4564.8	2981.6	1494.9	2684.7	1.0569

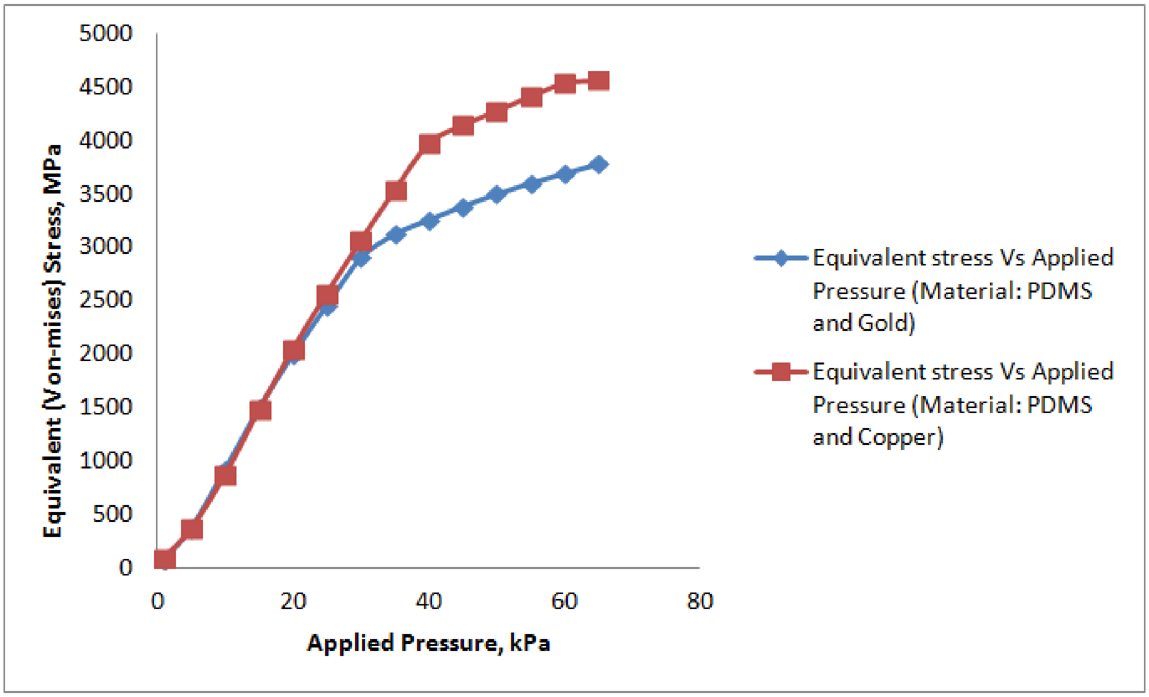

Figure 73: Comparison of equivalent stress for same thickness of Gold and Copper alternatively embedded in PDMS; electrode thickness 20 microns

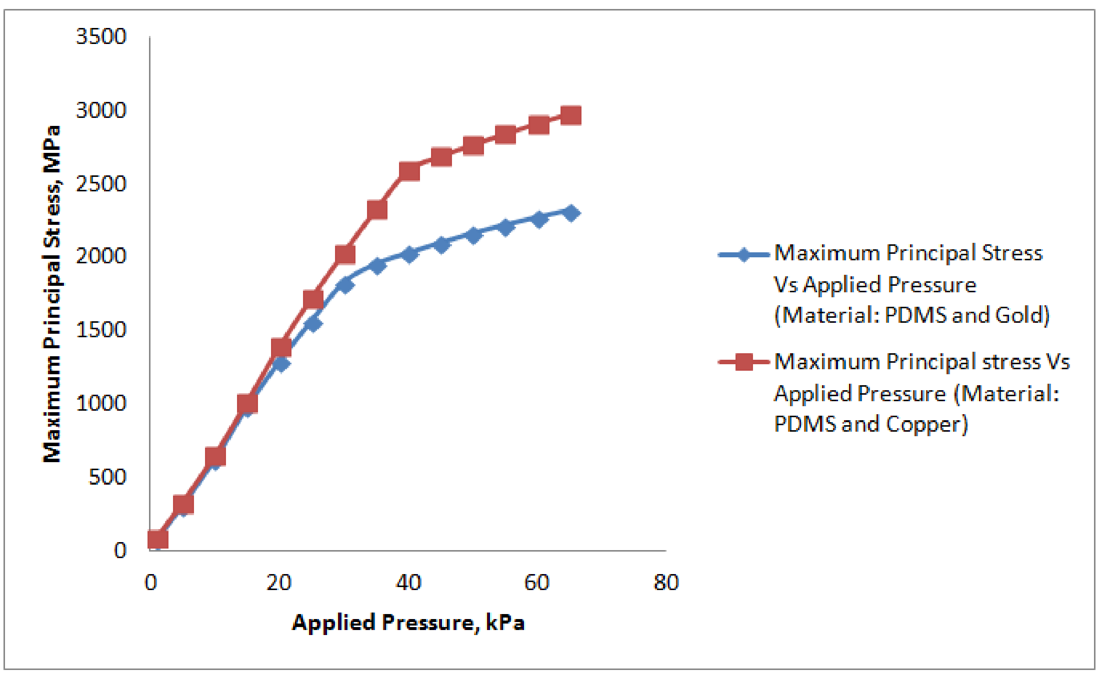

Figure 74 Continued: Comparison of equivalent stress for same thickness of Gold and Copper alternatively embedded in PDMS; electrode thickness 20 micron

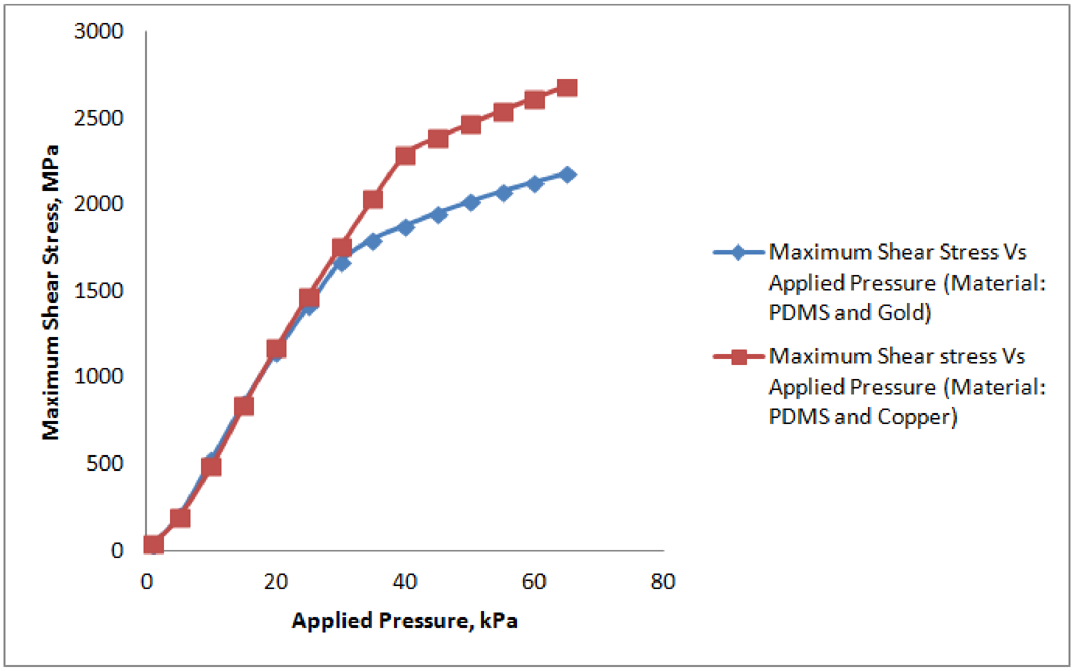

Figure 75: Comparison of Maximum shear stress for same thickness of Gold and Copper alternatively embedded in PDMS; electrode thickness 20 microns

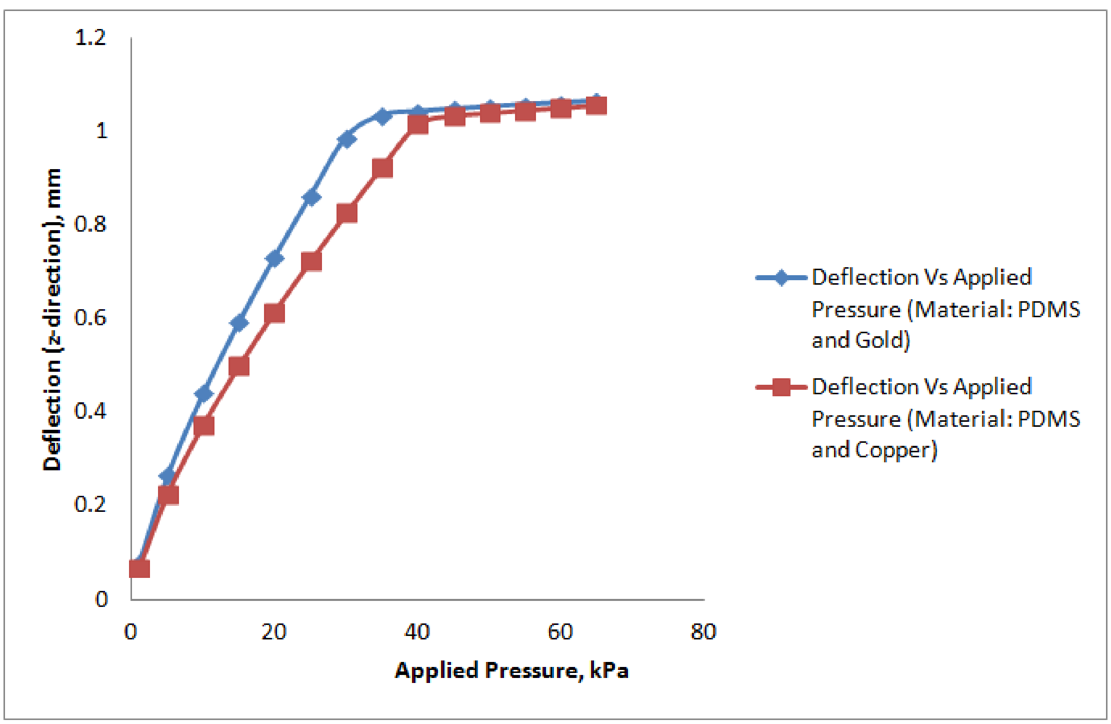

Figure 76: Comparison of Maximum deflection (Z-axis) for same thickness of Gold and Copper alternatively embedded in PDMS; electrode thickness 20 microns

The FEA analysis of the pressure sensor with PDMS as structural material has been tabulated. Two different types of electrode materials were trialed: Gold and Copper, considering the other parameters such as thickness and applied pressure being same on each condition. The contour plots showing the deformed shape of the solid body, location of maximum and minimum equivalent stresses, principal stresses and z-directional deformation has been included in Appendix-A. Only z-directional deformation was chosen to be included among the 3 directional deformations (x, y and z) since the external transverse load was applied along that direction. If the results between Gold and Copper as electrode material was compared it could be seen that the equivalent stress, maximum principal stress and shear stress values remained very comparable in both cases up-to 20 kPa of applied pressure. Those stresses increased very rapidly above 20 kPa applied pressure and significantly higher in the copper structure than gold with same thickness. On the other hand the maximum z-directional deformation value had been always higher in the gold embedded structure compared to copper electrodes. Finally both deflection curve approached near each other at about 1mm deflection of the sensor as the sensor was limited to deflect no more than 1mm due to a solid curved support of 1mm depth at the bottom. The bottom surface of the polymer layer started to touch the tibial support at about 35kPa with gold as the electrode material and at 40 kPa pressure it touched the support completely with copper as electrode material embedded inside the structure evident from Table 7 and 8, Figure 101, Appendix: A. From the material properties defined in the earlier chapter it was visible that the stiffness of copper was 110GPa and that of gold was 79 GPa. From the above tabulated results it could be seen that the stiffer material (copper) has resulted in higher average equivalent stress inside the model of the pressure sensor solid body and the higher stiffness has reduced the flexibility of the sensor as evident from the reduction of z-directional deformation in case of copper. Since the equivalent (Von-Mises) stress is a function of all three principal stresses it is easily comprehensible that the increments of the maximum and minimum principal stresses were also due to the added stiffness in the structure. If less equivalent stress concentration and higher flexibility was desired then PDMS embedded with gold electrodes was the optimum combination. The applied pressure range during the FEA analysis of the PDMS based pressure sensor was limited to 1-65 kPa because it was really challenging to get a force convergence above that pressure range with *ANSYS Workbench* analysis settings due to PDMS stiffness being 7900 times lower than gold and 12000 times lower than that of copper. The graphical representation of Equivalent stress vs. Applied pressure, Maximum shear stress vs. Applied pressure, Maximum principal stress vs. Applied pressure and Deflection vs. Applied pressure for PDMS based pressure sensor considering both copper and gold as electrodes were shown in Figure 73, 74 and 75.

From the above tabulated data of different types of stresses developed inside the pressure sensor with PDMS, gold and copper as structural material, the failure analysis of the sensor was also performed. This analysis was necessary because it would forecast whether the sensor in the above configuration would survive within the operating pressure range and keep the structural integrity of the sensor with the selected material types. According to Von-Mises failure criteria yielding of the structure will occur if the equivalent stress exceeds the yield strength of the material. From the stress table above and from the contour plots and color gradient of equivalent stresses and directional deformation (Z- axis) in appendix: A, it can be seen that the color varies from blue to red corresponding to the minimum and maximum equivalent stresses and maximum and minimum deflection along Z-axis. The negative value of the deformation indicated a downward deflection and positive value indicated upward deflection of the sensor along Z- axis. By hiding some of geometry entities one by one *Workbench* also allowed to inspect the location of maximum and minimum equivalent stresses developed on each individual body parts of the solid assembly. By inserting a special 'stress probe' tool of equivalent stress in the solution tree of the *ANSYS Workbench*, the maximum and minimum individual stresses could be seen on each solid parts of the 3D sensor assembly. The maximum and minimum equivalent stress results corresponding to some selected external pressures on each component of the sensor were tabulated and given below.

Table 9: Equivalent Stress developed in Each Individual Layer: Material PDMS and Gold (20 Microns thickness) at 1kPa

Name of Solid Part	Material	Yield Strength ,MPa	Applied Pressure, kPa	Electrode Thickness, µm	Maximum Equivalent Stress developed, Mpa	Minimum Equivalent Stress developed, Mpa
Upper Polymer Layer	PDMS	2.24	1	20	5.0489e-002	2.2727e-004
Lower Polymer layer	PDMS	2.24	1	20	9.4911e-002	2.8026e-004
Upper Electrodes	Gold	127	1	20	75.663	0.25763
Lower Electrodes	Gold	127	1	20	48.313	0.15086
Bump	PDMS	2.24	1	20	0.37722	3.429e-004

Table 9 Continued

Layer						
Insulation Layer	PDMS	2.24	1	20	4.8612e-002	4.8612e-002

Table 10: Equivalent Stress developed in Each Individual Layer: Material PDMS and Gold (20 Microns thickness) at 2 kPa

Name of Solid Part	Material	Yield Strength ,MPa	Applied Pressure, kPa	Electrode Thickness, μm	Maximum Equivalent Stress developed, Mpa	Minimum Equivalent Stress developed, Mpa
Upper Polymer Layer	PDMS	2.24	2	20	8.4723e-002	4.5454e-004
Lower Polymer layer	PDMS	2.24	2	20	0.15901	5.6053e-4
Upper Electrodes	Gold	127	2	20	135.74	0.51525
Lower Electrodes	Gold	127	2	20	104.01	0.30171
Bump Layer	PDMS	2.24	2	20	0.73982	6.858e-004
Insulation Layer	PDMS	2.24	2	20	0.10297	2.1538e-004

Table 11: Equivalent Stress developed in Each Individual Layer: Material PDMS and Gold (20 Microns thickness) at 3 kPa

Name of Solid Part	Material	Yield Strength ,MPa	Applied Pressure, kPa	Electrode Thickness, μm	Maximum Equivalent Stress developed, Mpa	Minimum Equivalent Stress developed, Mpa
Upper Polymer Layer	PDMS	2.24	3	20	0.11254	6.7578e-004
Lower Polymer layer	PDMS	2.24	3	20	0.1982	8.3336e-004
Upper	Gold	127	3	20	204.44	0.76605

Table 11 Continued

Electrodes						
Lower Electrodes	Gold	127	3	20	168.16	0.44857
Bump Layer	PDMS	2.24	3	20	1.123	1.0196e-003
Insulation Layer	PDMS	2.24	3	20	0.14924	3.2022e-004

Table 12: Equivalent Stress developed in Each Individual Layer: Material PDMS and Gold (20 Microns thickness) at 7 kPa

Name of Solid Part	Material	Yield Strength ,MPa	Applied Pressure, kPa	Electrode Thickness, µm	Maximum Equivalent Stress developed, Mpa	Minimum Equivalent Stress developed, Mpa
Upper Polymer Layer	PDMS	2.24	7	20	0.19877	1.4812e-3
Lower Polymer layer	PDMS	2.24	7	20	0.29217	1.8266e-003
Upper Electrodes	Gold	127	7	20	566.72	1.679
Lower Electrodes	Gold	127	7	20	426.44	0.98318
Bump Layer	PDMS	2.24	7	20	2.5518	2.2348e-003
Insulation Layer	PDMS	2.24	7	20	0.29476	7.0185e-004

Table 13: Equivalent Stress developed in Each Individual Layer: Material PDMS and Gold (20 Microns thickness) at 65 kPa

Name of Solid Part	Material	Yield Strength ,MPa	Applied Pressure, kPa	Electrode Thickness, µm	Maximum Equivalent Stress developed, Mpa	Minimum Equivalent Stress developed, Mpa
Upper Polymer Layer	PDMS	2.24	65	20	0.484	1.0028e-002

Table 13 Continued

Lower Polymer layer	PDMS	2.24	65	20	0.7972	2.1387e-002
Upper Electrodes	Gold	127	65	20	3782	13.657
Lower Electrodes	Gold	127	65	20	1768.8	9.7333
Bump Layer	PDMS	2.24	65	20	13.529	6.3054e-002
Insulation Layer	PDMS	2.24	65	20	0.76477	8.1028e-003

From the Table 9, it was clearly evident that at 1 kPa pressure the equivalent stress generated at each individual layer of the sensor stayed below their corresponding yield strength of the constituent materials. The components would undergo only linear elastic deformation and the stress was within their elastic limit at that pressure. However at 2 kPa pressure from Table 10, the equivalent stress developed in the upper gold electrodes of 20 micron thickness slightly exceeded the yield strength of the material which might led to plastic deformation (Figure 102, Appendix A) at some of the points. That means some part of upper electrodes would experience permanent deformation without returning to its original state. The other part of the sensor stayed below their corresponding yield point. At 3 kPa pressure both upper and lower electrodes of gold material experienced plastic deformation and yielding since the equivalent stress at certain points of their structure exceeded the yield strength (Figure 103, Appendix A). The stress built up in the PDMS encapsulation at this pressure range was also significant in this case but it was below its yield point. At 7 kPa external pressure the equivalent stress developed in the bumps reached to a value of 2.55 MPa which was slightly higher than the yield strength of PDMS. This was the first time when the PDMS made bump structures was experiencing plastic deformation (Figure 104, Appendix A) inside the sensor and these bumps were suffering from some degree of permanent deformation once the sensor was subjected to that amount of external pressure. Instead of elastic recovery of the bumps some of them will be plastically deformed after the sensor will be used for measurement of pressure distribution inside the knee joint. The other PDMS made bodies like upper and lower polymer layer and thin insulation layer experienced a very small amount of equivalent stress which was well below the yield point of PDMS as shown in the above Table 9,10 11,12 and 13.

Similarly PDMS with copper as electrode material with same thickness similar to gold electrodes underwent plastic deformation at about 4 kPa external pressure. An equivalent stress of 271.96 MPa was developed at upper copper electrodes which exceeded the yield strength of copper of 252.3 MPa. The lower electrodes experienced a maximum equivalent stress of 228.33 MPa which was still less than its yield point. The yielding continued as the pressure was increased subsequently over the pressure sensor. At 7 kPa pressure the PDMS made bumps started to experience plastic deformation because the equivalent stress of 2.25 MPa just exceeded its yield strength.

It was possible to get a force convergence with PDMS and Gold as sensor materials up-to 65 KPa and the PDMS made upper and lower encapsulation layers still remained linear elastic at that pressure range. Among the PDMS layers the lower polymer layer experienced the highest equivalent stress of 0.7972 MPa shown in Table 13 for 65 kPa of applied pressure which is still much lower than the yield stress of 2.24 MPa for

PDMS. The thin insulation layer developed the maximum equivalent stress of 0.829 MPa when copper was used as electrodes.

Another iteration of FEA analyses were ran with the same geometrical configuration but this time it was Polyimide as the structural and insulation material. Both gold and copper were considered as electrode material in the analyses. For Polyimide the force convergence pressure range achieved was much higher compared to PDMS. The analyses were run in between 10-100 kPa range at an increment of 10 kPa and from 100-400 kPa at an increment of 50 kPa. The results are tabulated below:

Table 14: Results obtained with Polyimide and Gold as structural materials

Electrode thickness (mm)	Electrode material	Insulation Material	Applied Surface Pressure (kPa)	Equivalent (Von-mises) Stress (Mpa)	Maximum Principal Stress (Mpa)	Minimum Principal Stress(Mpa)	Maximum Shear Stress (Mpa)	Directional Deformation (z-axis) (mm)
0.02	Gold	Polyimide	10	12.856	13.122	1.1597	6.4671	0.0056
0.02	Gold	Polyimide	20	25.229	25.744	21.363	12.69	0.011
0.02	Gold	Polyimide	30	37.186	37.937	3.3864	18.702	0.0163
0.02	Gold	Polyimide	40	48.831	49.81	4.4608	24.557	0.02141
0.02	Gold	Polyimide	50	60.076	61.279	5.5075	30.211	0.02632
0.02	Gold	Polyimide	60	70.947	72.368	6.5335	36.461	0.03105
0.02	Gold	Polyimide	70	81.701	83.11	8.5205	45.996	0.035616
0.02	Gold	Polyimide	80	98.843	93.561	11.526	55.558	0.04
0.02	Gold	Polyimi	90	115.89	103.81	14.658	65.956	0.0444

Table 14 Continued

		de						
0.02	Gold	Polyimide	100	137.32	113.88	17.874	79.023	0.04866
0.02	Gold	Polyimide	150	261.81	162.53	33.584	151.05	0.069213
0.02	Gold	Polyimide	200	385.52	208.5	47.319	222.55	0.089
0.02	Gold	Polyimide	250	501.02	264.67	58.322	289.25	0.10812
0.02	Gold	Polyimide	300	612.76	319.51	69.339	353.77	0.1267
0.02	Gold	Polyimide	350	721.49	373.11	78.89	416.54	0.14561
0.02	Gold	Polyimide	400	827.46	425.4	89.336	477.73	0.164

Table 15: Results obtained with Polyimide and Copper as structural materials

Electrode thickness (mm)	Electrode material	Insulation Material	Applied Surface Pressure (kPa)	Equivalent (Von-mises) Stress (Mpa)	Maximum Principal Stress (Mpa)	Minimum Principal Stress(Mpa)	Maximum Shear Stress (Mpa)	Directional Deformation (z-axis) (mm)
0.02	Copper	Polyimide	10	16.26	16.497	1.1576	8.1737	0.005517
0.02	Copper	Polyimide	20	31.953	32.417	2.2838	16.061	0.010887
0.02	Copper	Polyimide	30	47.151	47.832	3.3818	23.7	0.016111
0.02	Copper	Polyimide	40	61.996	62.89	4.4556	31.16	0.02118
0.02	Copper	Polyimide	50	76.363	77.468	5.5	38.378	0.026
0.02	Copper	Polyimide	60	90.172	91.484	6.522	45.319	0.03
0.02	Copper	Polyimide	70	103.53	105.04	7.9971	52.033	0.0352
0.02	Copper	Polyimide	80	116.57	118.28	10.904	58.589	0.04
0.02	Coppe	Polyimi	90	129.38	131.29	13.943	65.028	0.04383

Table 15 Continued

	r	de						9
0.02	Copper	Polyimide	100	141.98	144.08	17.072	75.906	0.048038
0.02	Copper	Polyimide	150	253.39	206.08	32.576	146.18	0.0683
0.02	Copper	Polyimide	200	375.71	265.24	46.352	216.88	0.0877
0.02	Copper	Polyimide	250	490	321.93	57.432	282.88	0.10673
0.02	Copper	Polyimide	300	600.42	378.06	68.331	346.64	0.12536
0.02	Copper	Polyimide	350	708.04	433.79	77.977	408.78	0.14376
0.02	Copper	Polyimide	400	812.41	489.13	87.859	469.04	0.16194

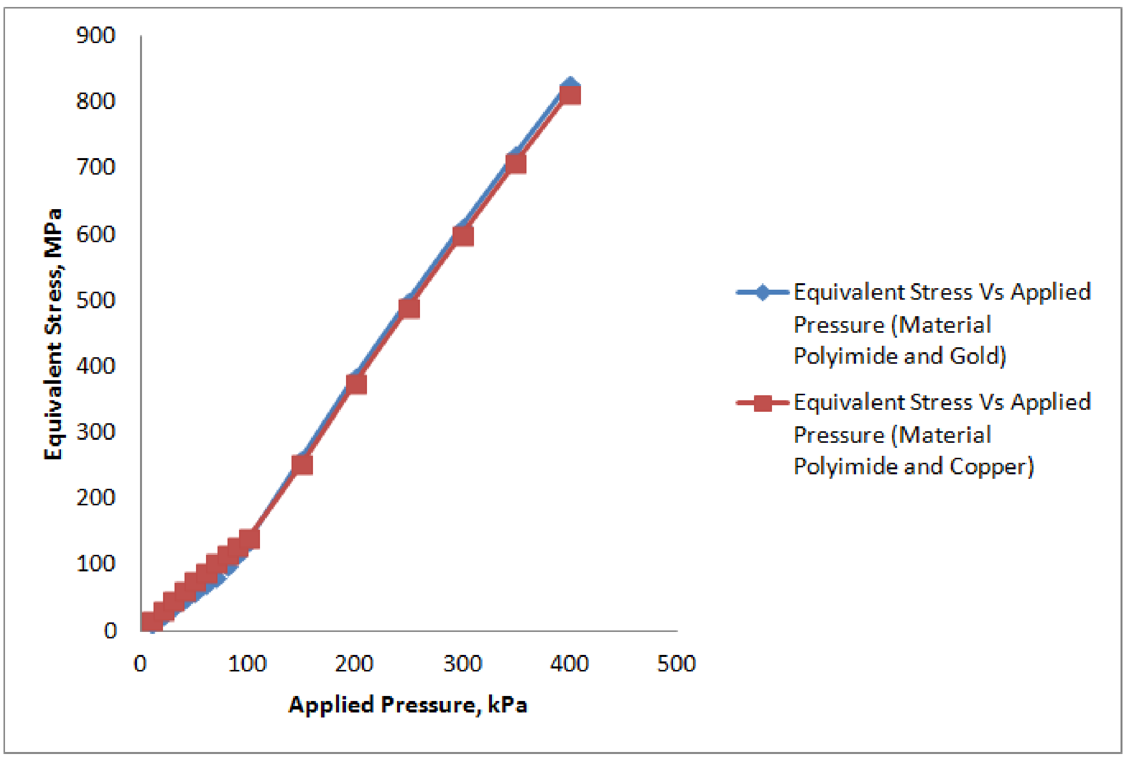

Figure 77: Comparison of equivalent stress for same thickness of Gold and Copper alternatively embedded in Polyimide; electrode thickness 20 microns

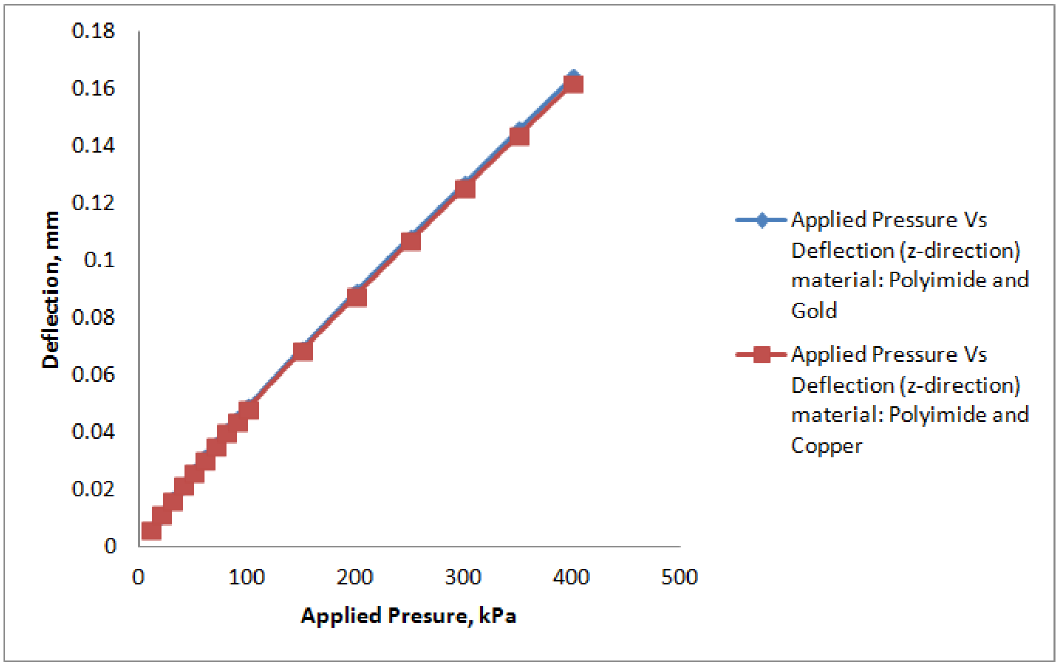

Figure 78 Continued: Comparison of Deflection (Z-direction) for same thickness of Gold and Copper alternatively embedded in Polyimide; electrode thickness 20 microns

With Polyimide as structural material the sensor now behaved more rigidly compared to PDMS. The equivalent stress developed with copper stayed higher than gold in the polyimide structure up-to an applied pressure of 150 kPa. When the external pressure exceeded 150 kPa range the equivalent stress concentration was higher in the polyimide structure containing gold than copper as evident from Figure 77 and in each case electrode thickness was kept at 20 microns. Once again better flexibility was achieved by using gold electrodes than copper as evident from the Figure 78. But in both cases the deflection was very low in Polyimide compare to PDMS structure and at a given applied pressure of 60 kPa the deflection in PDMS was 34 times higher than Polyimide.

Table 16: Equivalent Stress developed in Each Individual Layer: Material Polyimide and Gold (20 Microns thickness) at 100 kPa

Name of Solid Part	Material	Yield Strength ,MPa	Applied Pressure, kPa	Electrode Thickness, μm	Maximum Equivalent Stress developed, Mpa	Minimum Equivalent Stress developed , Mpa
Upper Polymer Layer	Polyimide	231	140	20	24.788	9.8731e-002
Lower Polymer layer	Polyimide	231	140	20	93.356	0.23439
Upper Electrodes	Gold	127	140	20	115.61	0.4108
Lower Electrodes	Gold	127	140	20	149.97	0.45375
Bump Layer	Polyimide	231	140	20	236.12	7.108e-2
Table 16 Continued						
Insulation Layer	Polyimide	231	140	20	20.244	4.202e-002

The equivalent stress developed in the polyimide structures were not significant until 140 kPa external pressure was applied shown at Table 16. At that pressure the stress concentration at some point of the polyimide bumps and lower gold electrodes were high enough to surpass their yield strengths and caused plastic deformation. The contour plot of the locations of the plastic deformations was given at Figure 105, Appendix: A. and at 170 kPa pressure the upper electrodes also started to plastically deform inside Polyimide-Gold structure by 136.26 MPa of equivalent stress which surpassed its yield point of 127 Mpa shown in Figure 106, Appendix: A. Similarly In Polyimide-Copper Structure, the Polyimide bumps and Lower electrodes started to undergo plastic deformation at 137 kPa pressure and lower copper electrodes experienced the yielding at about

Thickness Effect

FEA analyses were run again on polyimide structure to observe the thickness effect of metal electrodes. Two different thicknesses of metal electrodes were compared which were 5 and 20 microns embedded inside the same thickness of Polyimide to observe the effect. The results are tabulated below:

Table 17: Results obtained with Polyimide and Gold (thickness of 5 microns) as structural materials

Electrode thickness (mm)	Electrode material	Insulation Material	Applied Surface Pressure (kPa)	Equivalent (Von-mises) Stress (Mpa)	Maximum Principal Stress (Mpa)	Minimum Principal Stress(Mpa)	Maximum Shear Stress (Mpa)	Directional Deformation (z-axis) (mm)
0.005	Gold	Polyimide	10	17.633	15.149	1.5621	9.0576	0.0062717
0.005	Gold	Polyimide	20	32.33	28.218	2.9356	16.632	0.0121
0.005	Gold	Polyimide	30	44.576	39.394	4.1322	22.971	0.017521
0.005	Gold	Polyimide	40	54.657	48.765	5.1077	28.215	0.0225
0.005	Gold	Polyimide	50	63.329	56.954	5.98	32.745	0.027216
0.005	Gold	Polyimide	60	72.352	64.085	7.0794	41.003	0.0317
0.005	Gold	Polyimide	70	89.906	69.671	8.9931	50.951	0.03601
0.005	Gold	Polyimide	80	107.39	75.817	11.965	60.865	0.04
0.005	Gold	Polyimide	90	124.73	88.4	14.974	70.708	0.04433
0.005	Gold	Polyimide	100	144.58	100.75	18.067	83.159	0.04838

Table 18: Results obtained with Polyimide and Copper(thickness of 5 microns) as structural materials

Electrode thickness (mm)	Electrode material	Insulation Material	Applied Surface Pressure (kPa)	Equivalent (Von-mises) Stress (Mpa)	Maximum Principal Stress (Mpa)	Minimum Principal Stress(Mpa)	Maximum Shear Stress (Mpa)	Directional Deformation (z-axis) (mm)
Table 18 Continued								
0.005	Copper	Polyimide	10	20.488	18.207	1.6286	10.485	0.0062
0.005	Copper	Polyimide	20	37.483	33.918	3.0457	19.209	0.01195
0.005	Copper	Polyimide	30	51.77	47.513	4.2857	26.574	0.01733
0.005	Copper	Polyimide	40	63.582	59.05	5.2923	32.693	0.022286
0.005	Copper	Polyimide	50	73.788	69.239	6.16	38.001	0.02698
0.005	Copper	Polyimide	60	82.597	78.198	7.098	42.602	0.031457
0.005	Copper	Polyimide	70	90.585	85.458	8.576	49.924	0.03575
0.005	Copper	Polyimide	80	105.29	92.09	11.492	59.697	0.04
0.005	Copper	Polyimide	90	122.4	98.247	14.416	69.417	0.044
0.005	Copper	Polyimide	100	139.91	104.06	17.412	80.46	0.048085

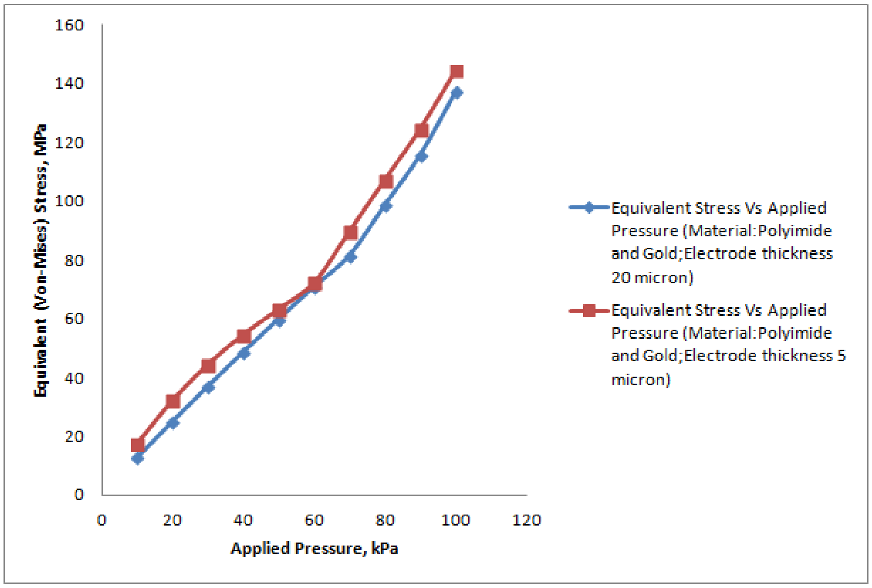

Figure 79: Equivalent Stress in the Polyimide Structure considering Gold Electrodes of 5 and 20 microns thickness alternatively

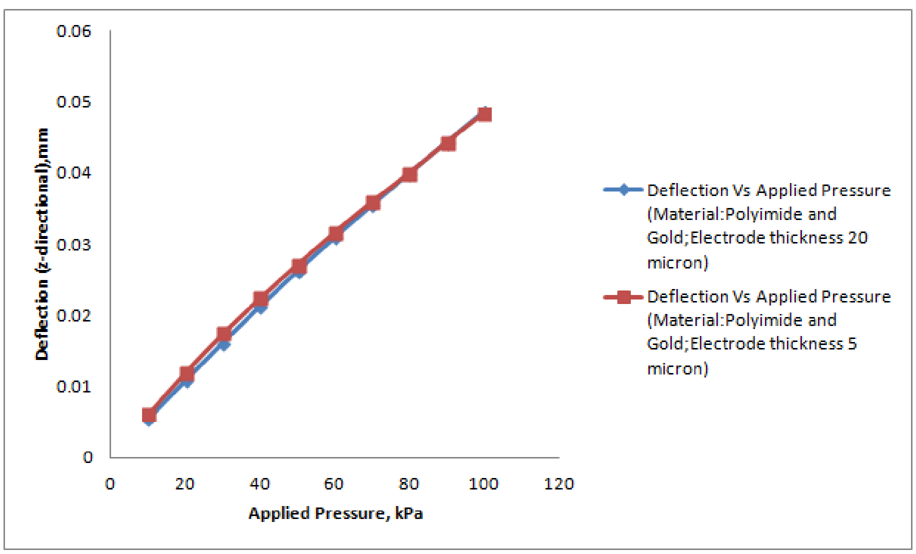

Figure 80: Deflection (Z-directional) in the Polyimide Structure considering Gold Electrodes of 5 and 20 microns thickness alternatively

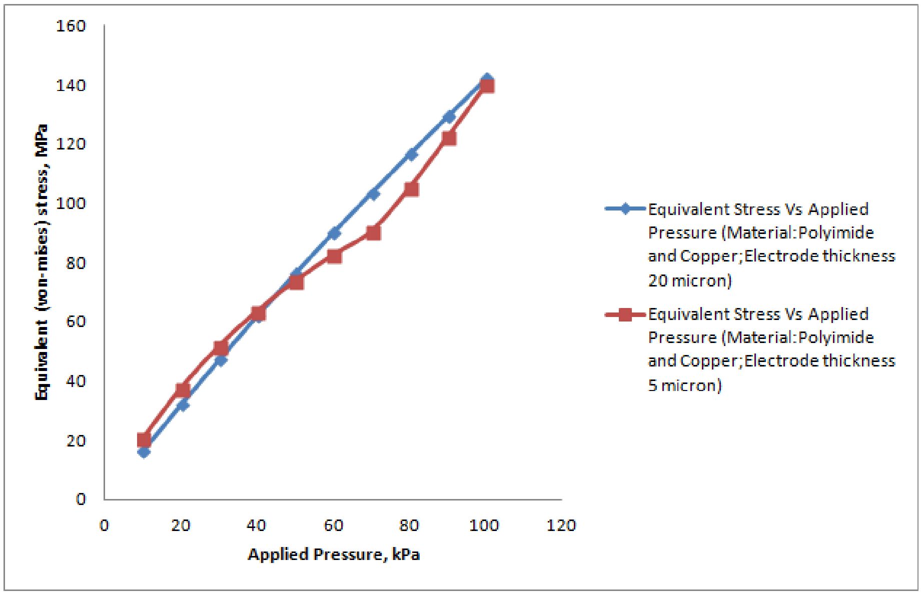

Figure 81: Equivalent Stress in the Polyimide Structure considering Copper Electrodes of 5 and 20 microns thickness alternatively

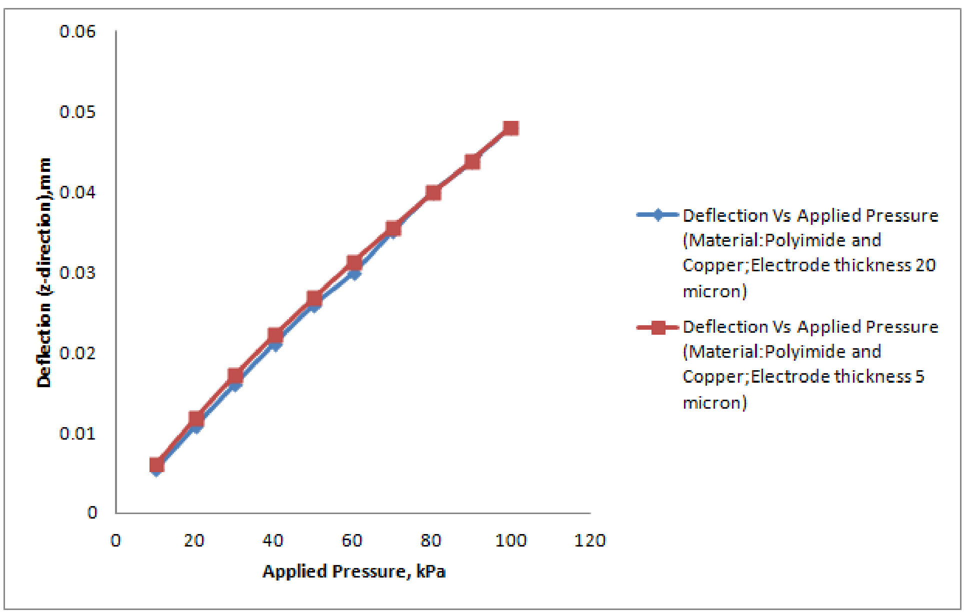

Figure 82: Deflection (Z-directional) in the Polyimide Structure considering Copper Electrodes of 5 and 20 microns thickness alternatively

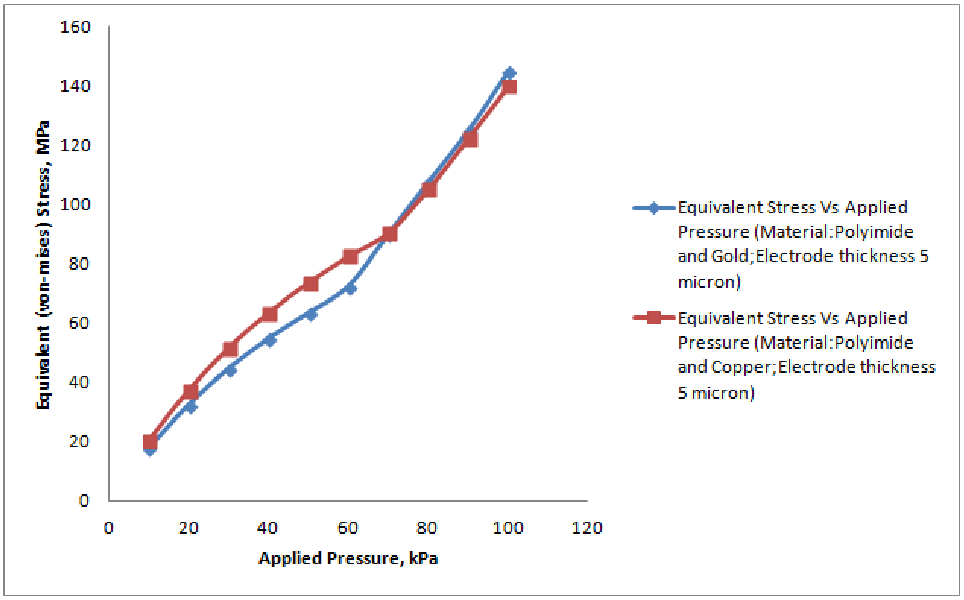

Figure 83: Comparison of Equivalent Stress in the Polyimide Structure considering both Copper and Gold Electrodes of 5 microns thickness

From the above graphical representation it was clearly evident that lower thickness of gold electrodes produced more stress concentration in the polyimide structure than the higher thickness of the same material shown in Figure 79. On the other hand the thinner metal film of gold resulted in more deflection or flexibility in the structure than thicker film shown in Figure 80. However the thickness variation of copper as electrode material exhibited somewhat different behavior than gold material. The lower thickness of copper electrodes produced higher stress concentration in the polyimide structure upto 50 kPa of applied pressure but the stress concentration went down compared to higher thickness of copper electrodes after 50 kPa applied pressure as shown in Figure 81. So in case of copper material, higher thickness of electrodes would be beneficial upto a low range of applied pressure (1-50kPa). As the contact stress would rise, thinner copper electrodes would produce less stress concentration in the structure.

The deflection characteristics curve with copper was found similar as gold shown in Figure 82. Overall gold as electrodes material would produce lesser stress concentration in the polyimide structure than copper of similar thickness evident from Figure 83 due to copper stiffness being 1.4 times higher than gold material.

VERIFICATION OF FE MODELING

To verify the FE model built in this article a simplified geometry of the model was constructed for the ease of hand calculation and verifying with software simulation results. The boundary conditions were kept similar as the FE model of the pressure sensor i.e. both ends fixed support. Except multiple material layers inside the structure, only polyimide was considered as the isotropic and homogeneous constituent material. The geometry was similar to the actual sensor dimensions of 1.2 by 4 mm with a total thickness of 0.212 mm shown in Figure 84.

The following linear elastic material properties were considered for Polyimide:

Modulus of Elasticity, E= 2.5 GPa= 2500 MPa

Poisson's Ratio= 0.34

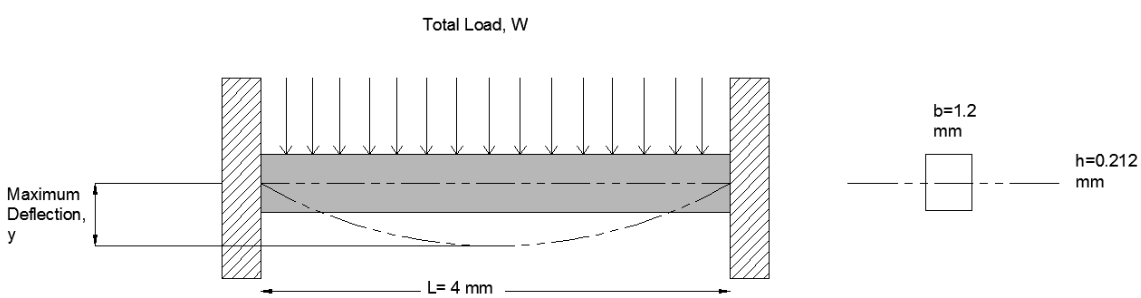

Figure 84: A both End fixed beam under uniformly distributed load W

For a surface pressure of 10 kPa , Pressure= 10 kPa= 0.01 MPa = 0.01 $\frac{\text{Newton}}{\text{mm}^2}$

Total Surface area of the Pressure sensor = (1.2*4) mm^2 = 4.8 mm^2

Moment of Inertia for rectangular section (39),

$$I = \frac{b \cdot h^3}{12} \qquad \text{Equation 11}$$

$$= \frac{1.2\ mm*0.2123mm^3}{12}$$

$$= 9.528E\text{-}4\ mm^4$$

Section modulus of Cross section of beam (39),

$$Z = \frac{b \cdot h^2}{6} \qquad \text{Equation 12}$$

$$= \frac{1.2mm*0.2122mm^2}{6}$$

$$=0.00898\ mm^3$$

So, total surface load, W= Total Surface Pressure * Total Surface Area

= (0.01*4.8) (mm^2 * Newton/mm^2)

= 0.048 Newton

For a Both End Fixed beam, maximum deflection equation from (40) for a 0.048 Newton force will be,

$$Y = \frac{W \cdot L^3}{384 \cdot E \cdot I} \qquad \text{Equation 13}$$

$$= \frac{0.048\ Newton*(4)^3 mm^3}{384*2500(Newton/mm^2)*(9.528E\text{-}4mm^4)}$$

$$= 0.003358\ mm$$

Maximum Stress at fixed ends (40),

$$\sigma = \frac{W \cdot L}{12 \cdot Z} \qquad \text{Equation 14}$$

$$= \frac{0.048\ Newton*4mm}{12*0.00898\ mm^3}$$

$$= 1.7817\ MPa$$

Workbench Simulation Results for both end Fixed beam:

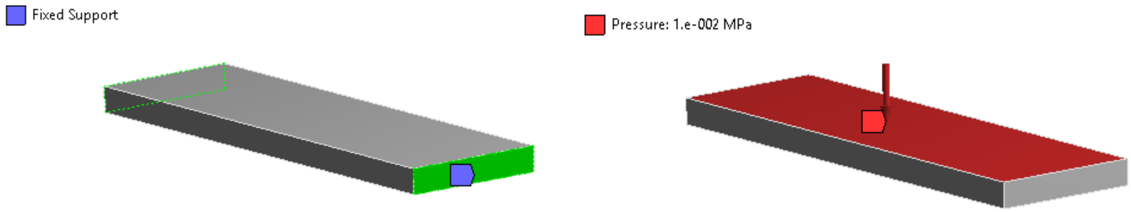

Figure 85: Both end Fixed Polyimide beam with surface pressure of 10 kPa

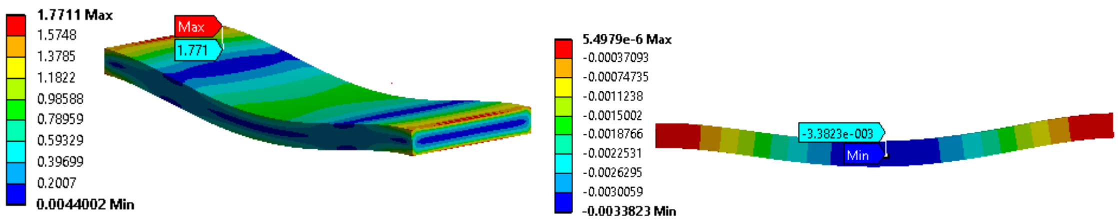

Figure 86: Location of Maximum Stress at Fixed end and Maximum downward deflection at 10 kPa pressure

From *Workbench* simulation a maximum z directional deflection derived for 10 kPa pressure was 0.00338mm and hand calculated maximum deflection value derived from Equation 13 was 0.003358mm with a percentage error of 0.65% between them. Value of Maximum stress found at the fixed ends by hand calculation using Equation 14 was 1.78 MPa and maximum equivalent stress from *Workbench* simulation was 1.771 MPa shown in Figure 86 with a percentage error of 0.5% between them.

So from the above evaluation it would be safe to assume that the Finite element model of the pressure sensor were relevant and verified simulation results.

THERMAL STRESS

Thermal stresses are induced in microsystems operating at higher temperature due to mechanical constraints or mismatch of coefficient of thermal expansion of the mating parts. Since most microdevices are made of components having different materials such as deposited thin films, so mismatch of coefficient of thermal expansion (CTE) should be considered during the design process since excessive stress could be a cause of the failure of the device (5).

Since the temperature during Electrochemical deposition range from room temperature to 1000C (42) so due to mismatch of coefficient of thermal expansion for metal and polymer materials some thermal stress will develop in the structure when they will be cooled down to room temperature due to contraction. A 2D analysis of the sensor structure was performed considering both PDMS and Polyimide as polymer membrane alternatively and trialed both gold and copper as electrode material to verify if the stress developed due to difference of CTE was significant enough or not. The analysis would only be applicable if the polymer casting over silicon wafer started immediately after the metallization process so that it would result in good adhesion between polymer and metal layer. If the casting of polymer was performed after the metal layer cooled down to room temperature than this analysis would not be significant. The temperature difference would induce thermal load inside the structure and produce residual thermal stress when cooled down to room temperature. Our point of interest was to verify if the residual stress would create any plastic deformation in the structure.

The thermal material properties used were:

Coefficient of thermal expansion of PDMS = 310E-6 $\frac{1}{\text{Kelvin}}$ (26)

Coefficient of thermal expansion of Polyimide = 20E-6 $\frac{1}{\text{Kelvin}}$ (32)

Coefficient of thermal expansion of Gold = 14.2E-6 $\frac{1}{\text{Kelvin}}$ (33)

Coefficient of thermal expansion of Copper = 17E-6 $\frac{1}{\text{Kelvin}}$ (44)

In the simulation the model was cooled down from 1000C to room temperature of 220C and the effect was observed if the cooling process induced any residual stress inside the structure. The analysis was performed using *ANSYS* parametric design language (APDL) and the code was included in the appendix B section. The results are tabulated below:

Table 19: Total Equivalent stress and Total thermal and mechanical Strain Considering different materials

Material	Total Maximum Equivalent Stress Developed, MPa	Total Minimum Equivalent Stress Developed, MPa	Total Maximum Mechanical and Thermal Strain	Total Minimum Mechanical and Thermal Strain
PDMS and Gold	0.338435	0.579E-05	0.094743	0.342E-07
PDMS and Copper	0.334705	0.572E-05	0.095092	0.231E-07
Polyimide and Gold	18.7359	0.406E-03	0.007494	0.162E-06
Polyimide and Copper	19.5259	0.334E-03	0.00781	0.134E-06

From the above results of Table 19 for only thermally applied load on a 2D sensor model it could be observed that a maximum residual stress of 0.338 MPa and 0.334 MPa were developed at the interface of PDMS with gold/copper layers alternatively shown in Figure 107 and 109, Appendix A. Similarly A maximum equivalent stress of 18.7359 MPa and 19.5259 MPa were developed with polyimide and gold/copper interface shown in Figure 111 and 113, Appendix A. PDMS structure underwent about 12 times more thermal and mechanical strain compared to polyimide shown in Figure 108 and 110, Appendix A. It was due to PDMS having very large coefficient of thermal expansion/contraction which was 16 times higher than that of Polyimide and mechanical stiffness was much higher in Polyimide. PDMS structure containing gold electrodes had very comparable residual stress with PDMS containing copper electrodes which were due to the fact that gold and copper had very similar coefficient of thermal expansion. As a result the residual stress was largely dominated by contraction of the PDMS membrane and it was well below yield stress of any of the constituent material. Similarly the residual stress in the polyimide structure was also below yield limit of any of the constituent material but releasing the stress would be a better solution to confirm accuracy and precision of reading form the sensor.

READOUT CIRCUIT SCHEMATIC

Any typical capacitance readout circuit consists of a scanning circuitry in the form of row and column decoder or a set of multiplexers providing the driving signals (Source voltage) to either row or column electrodes. For a target sensing element (Cs), a sinusoidal input voltage (Vs) would be applied to the capacitor and corresponding output voltage Vowould be measured by the relation:

$$V_o = -V_s \cdot \frac{C_s}{C_f} \qquad \text{Equation 15}$$

Where Cf is the feedback capacitance and Rf is the feedback resistance shown in Figure 87. When the sinusoidal input voltage Vswould be switched to the pressure sensing capacitive cell element by row/column multiplexer sub-circuits, the electric charge stored in the capacitance due to polymer surface deflection would be transferred to the capacitance measurement circuit feedback capacitance Cf which would be converted into a DC signal Vo as given by Equation 15 by a peak value detector and detected by analog-to-digital converter (ADC). A data acquisition system on a chip would be used as controller of the scanning circuit. Two multiplexer would require for selecting row and column electrodes and an operational amplifier (Op amp) would be used for signal conditioning. Scanning request could be made from a computer through universal serial bus or parallel port interface and scanned data could be transferred back to the computer again for visualization and data analysis purpose shown in the schematic diagram in Figure 88.

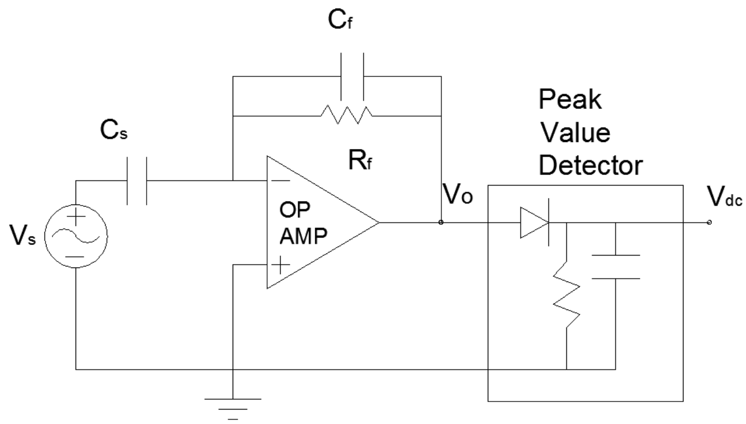

Figure 87: Typical Read-Out Circuit for Capacitive sensor

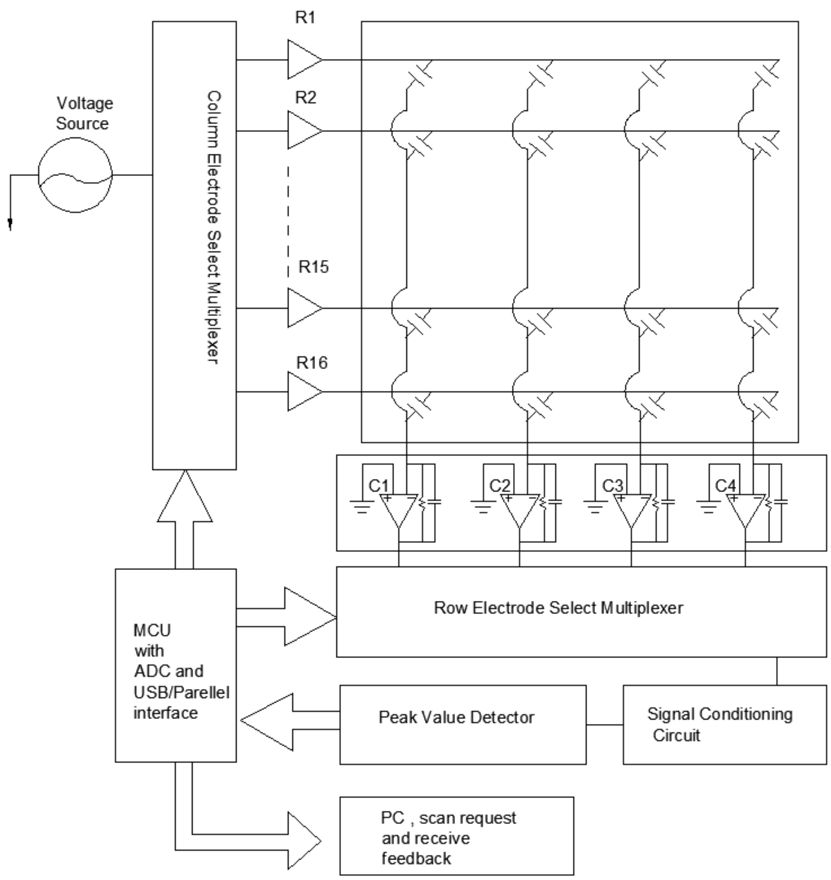

Figure 88: Capacitive Row and Column Senor Array with Scanning Circuits using Multiplexers; R 1, R2.. R16 and C1, C2.. C16 represents Row and Column respectively; Image and Idea inspired from (41)

FUTURE WORK AND CONCLUSION

There is still a lot of improvement scope for this work. The future work of this pressure sensor would be to go for the actual clean-room fabrication of the sensor. Once the constituent materials and designs would be finalized a distinct and precise fabrication steps would reduce the cost and raise the efficiency of the fabrication greatly. The current design would allow fabricating two sensors at a time within a single silicon wafer with same process steps and materials but minor tweaking in the design might allow more to fabricate at a time. Because these silicon micro-fabrication process requires multiple attempts to achieve a successful product on a trial and error basis. An extensive research need to be made on the bonding techniques and success of different materials to avoid delamination of different layers during the actual fabrication of the sensor. This work was an effort to start the design of this unique pressure sensor from scratch and highlight various design aspects of the sensor model from electromechanical and structural perspective. Since it was a micro-electro mechanical device a solid readout circuit design with high gain and signal to noise ratio would be paramount for accurate and precise reading from the sensor. Construction of such a precise circuit would be challenging but possible since there have been many sensitive readout circuits already made for capacitance measurements found in various relevant literatures. Calibration of the sensor would be of utmost importance because in order to have a functional pressure sensor and to get readings from it, the sensor should be properly calibrated. Micro force gauge with force transducers could be utilized in calibration of this type sensor by pressing the force probe against each sensitive cell and plotting the response Vs force graph.

This pressure sensor was intended to be used inside a mouse knee and there had been no such pressure sensor array fabricated yet to measure contact stress distribution of geometry in such a small scale. There had been some attempt made to prototype the sensor with flexible printed circuits on kapton polymer (polyimide) but the minimum feature size achievable by flexible Circuit board printing didn’t meet the requirements of minimum feature size for our specific requirement. The flexible PCB printing required reducing the number of sensing elements from the sensor to prototype which would greatly reduce sensitivity and pressure mapping area inside knee joint. So the best solution would be to invest in a clean-room micro-fabrication of the pressure sensor where submicron feature sizes would be possible to make with greater precision on a silicon wafer.

REFERENCES CITED

1. Ko WH, Min-Hang B, Yeun-Ding H, editors. *A high-sensitivity integrated-circuit capacitive pressure transducer*1982: IEEE.

2. Narducci M, Yu-Chia L, Fang W, Tsai J. *CMOS MEMS capacitive absolute pressure sensor*. JOURNAL OF MICROMECHANICS AND MICROENGINEERING. 2013;23(5).

3. Goldring MB, Goldring SR. *Osteoarthritis. Journal of cellular physiology*. 2007;213(3):626-34.

4. Segal NA, Anderson DD, Iyer KS, Baker J, Torner JC, Lynch JA, et al. *Baseline articular contact stress levels predict incident symptomatic knee osteoarthritis development in the MOST cohort. Journal of orthopaedic research* : official publication of the Orthopaedic Research Society. 2009;27(12):1562-8.

5. *MEMS and MICROSYSTEMS*, 2nd Edition by Tai-Ran Hsu

6. Eaton WP, Smith JH. *Micromachined pressure sensors: review and recent developments*. Smart Materials and Structures. 1997;6(5):530-9.

7. A. Heidary, "*A Low-Cost Universal Integrated Interface for Capacitive Sensors*"promotor: prof.dr.ir. G.C.M. Meijer;2010, 150p. ISBN: 978-94-6113-

8. Hunter DJ. Osteoarthritis. *Best practice & research Clinical rheumatology*. 2011;25(6):801-14.

9. Vincent C. Hascall, Klaus E. Kuettner. *The many faces of Osteoarthritis*, Pg-383

10. Leena Sharma, Francis Berenbaum. *A Companion to Rheumatology Osteoarthritis*.

11. Segal NA, Kern AM, Anderson DD, Niu J, Lynch J, Guermazi A, et al. *Elevated tibiofemoral articular contact stress predicts risk for bone marrow lesions and cartilage damage at 30 months. Osteoarthritis and cartilage* / OARS, Osteoarthritis Research Society. 2012;20(10):1120-6.

12. Teeple E, Jay GD, Elsaid KA, Fleming BC. *Animal Models of Osteoarthritis: Challenges of Model Selection and Analysis*. The AAPS Journal. 2013;15(2):438-46.

13. Kamekura S, Nakamura K, Kawaguchi H, Hoshi K, Shimoaka T, Chung U, et al. *Osteoarthritis development in novel experimental mouse models induced by knee joint instability*. Osteoarthritis and cartilage / OARS, Osteoarthritis Research Society. 2005;13(7):632-41.

14. Rose T.J, MSME Thesis, "*Static Loading Apparatus for Mouse and Rat Knees*" May 2013

15. Goldring MB. Do *mouse models reflect the diversity of osteoarthritis in humans*? Arthritis and rheumatism. 2012;64(10):3072-5.

16. Hyung-Kew L, Sun-Il C, Yoon E, Yoon E. A Flexible Polymer Tactile Sensor: *Fabrication and Modular Expandability for Large Area Deployment. Journal of Microelectromechanical Systems*. 2006;15(6):1681-6.

17. Dagamseh AMK, Wiegerink RJ, Lammerink TSJ, Krijnen GJM.*Towards a high-resolution flow camera using artificial hair sensor arrays for flow pattern observations*.Bioinspiration&biomimetics. 2012;7(4):046009.

18. Cheng MY, Huang XH, Ma CW, Yang YJ. *A flexible capacitive tactile sensing array with floating electrodes.Journal of Micromechanics and Microengineering*. 2009;19(11):115001.

19.http://www.amicusvisualsolutions.com/cgibin/big_image.cgi?image=05009_01X&orientation=H. [Online]

20. *Introduction to Microelectronic Fabrication*, 2nd Edition by Richard C. Jaeger

21. Bean KE, Bean KE. *Anisotropic etching of silicon*. IEEE Transactions on Electron Devices. 1978;25(10):1185-93.

22. Schneider F, Draheim J, Kamberger R, Wallrabe U. *Process and material properties of polydimethylsiloxane (PDMS) for Optical MEMS*. Sensors & Actuators: A Physical. 2009;151(2):95-9

23. Satoshi S, Sawano S, Keisuke N, Naka K, Werber A, Werber A, et al., editors. *Sealing method of PDMS as elastic material for MEMS*2008: IEEE.

24. Larsen AL, Hansen K, Sommer-Larsen P, Hassager O, Bach A, Ndoni S, et al. *Elastic properties of nonstoichiometric reacted PDMS networks*. MACROMOLECULES. 2003;36(26):10063-70.

25. Lei KF, Lee KF, Lee MY. *Development of a flexible PDMS capacitive pressure sensor for plantar pressure measurement*. MICROELECTRONIC ENGINEERING. 2012;99:1-5.

26. http://www.mit.edu/~6.777/matprops/pdms.htm [Online]

27. Hasenkamp W, Forchelet D, Pataky K, Villard J, Lintel HV, Bertsch A, et al. *Polyimide/SU-8 catheter-tip MEMS gauge pressure sensor. Biomedical Microdevices*. 2012;14(5):819-28.

28. Hubbard RL, Fathi Z, Ahmad I, Matsutani H, Hattori T, editors. *Low temperature curing of polyimide wafer coatings*2004.

29. Damaceanu MD, Rusu RD, Bruma M, Muller A, editors. *Thin polyimide films for dielectric interlayer application*2009.

30. http://www.arl.army.mil/arlreports/2009/ARL-TR-5031.pdf [Online]

31.http://www2.dupont.com/Kapton/en_US/assets/downloads/pdf/summaryofprop.pdf [Online]

32. http://www2.dupont.com/Packaging_and_Circuits/en_US/assets/downloads/pdf/HD-7000_ProcessGuide.pdf [Online]

33. http://www.mit.edu/~6.777/matprops/gold.htm [Online]

34. Xiang Y, Tsui TY, Vlassak JJ. *The mechanical properties of freestanding electroplated Cu thin films*. JOURNAL OF MATERIALS RESEARCH. 2006;21(6):1607-18.

35. Ding M, Dalstra M, Linde F, Hvid I. Mechanical properties of the normal human tibial cartilage-bone complex in relation to age. Clinical Biomechanics. 1998;13(4):351-8.

36. http://www1.*ANSYS*.com/customer/content/documentation/120/ans_ctec.pdf [Online]

37. "*Finite Element Simulation with ANSYS Workbench 13*" by Huei-Huang Lee

38. *ANSYS*. Documentation for *ANSYS Workbench*

39. "*Vector Mechanics for Engineers*", 9th Edition by Beer,Johnston et al.

40. *Machinery's Handbook*, 28th Edition by Oberg E, Jones F. et al. 2008.

41.Cheng M-Y, Lin C-L, Lai Y-T, Yang Y-J. *A polymer-based capacitive sensing array for normal and shear force measurement. Sensors* (Basel, Switzerland). 2010;10(11):10211-25.

42. "*Introduction to Microfabrication*" By Sami Franssila

43. Van den Noort JJC, van der Esch M, Steultjens MPM, Dekker J, Schepers MHM, Veltink PH, et al. *Ambulatory measurement of the knee adduction moment in patients with osteoarthritis of the knee*. Journal of biomechanics. 2013;46(1):43-9.

44. Thermal Expansion. *Wikipedia.* [Online] http://en.wikipedia.org/wiki/Thermal_expansion.

APPENDICES

APPENDIX A:

CONTOUR PLOTS

For all images with Isometric view, the following axis orientations were used:

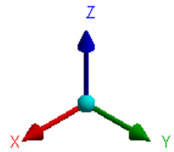

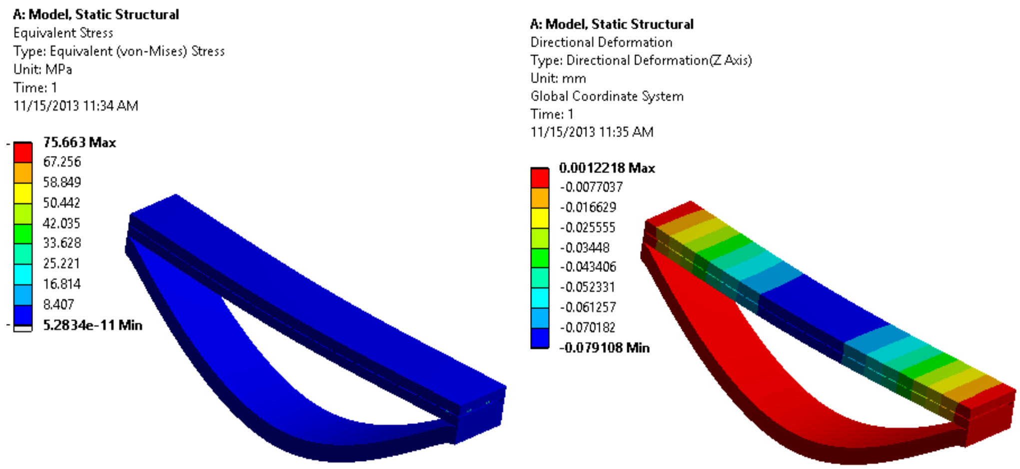

Figure 89: Equivalent (Von-mises) stress and directional deformation at any point in the structure at 1 kPa pressure; material PDMS and Gold

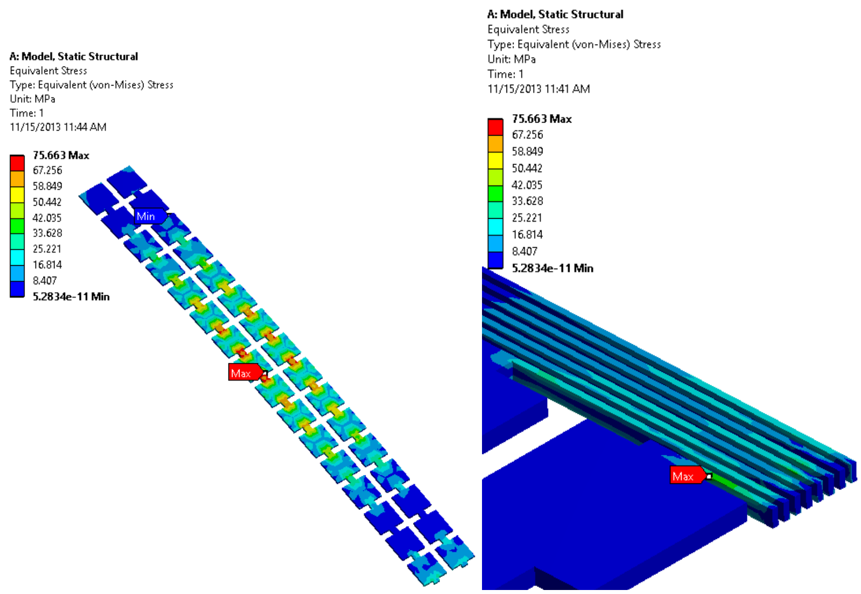

Figure 90: At 1 kPa,Von-mises Stress distribution on Upper and lower electrodes and location of max stress; material PDMS and Gold

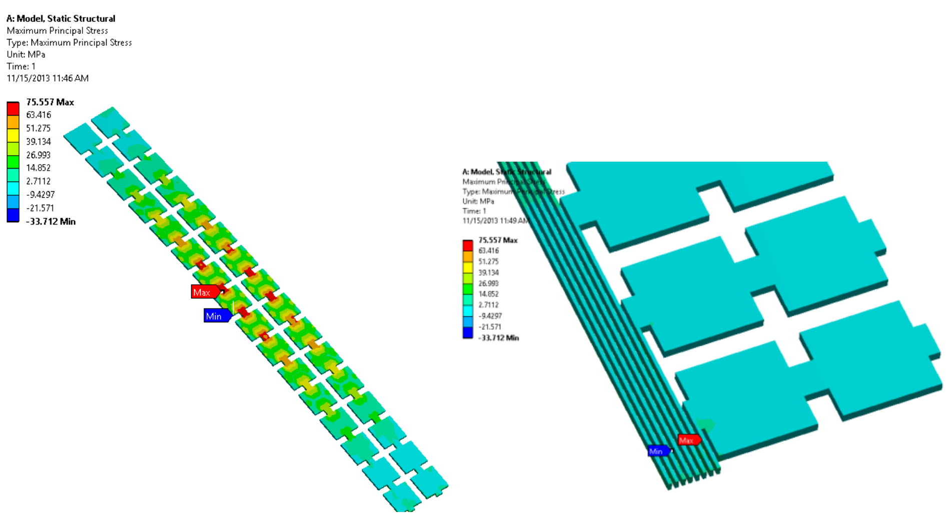

Figure 91: At 1 kPa ,Maximum Principal Stress on Upper and lower electrodes and location of max stress; material PDMS and Gold

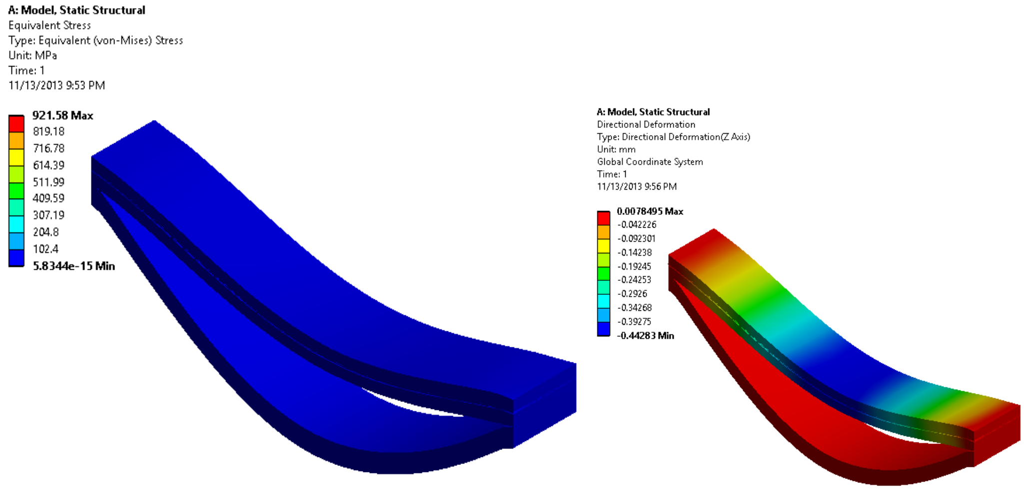

Figure 92: At 10kPa, Equivalent (Von-mises) stress and z-deformation at any point in the structure at 10KPa pressure; material PDMS and Gold

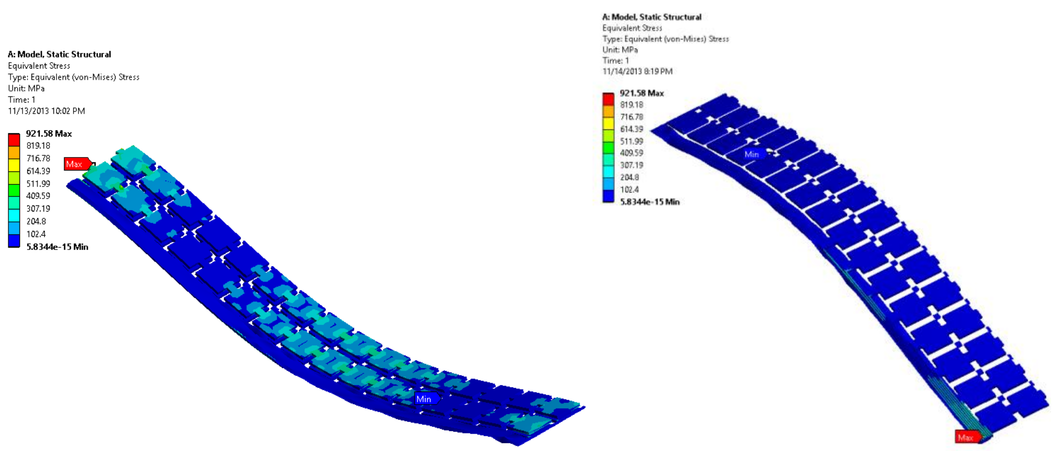

Figure 93: At 10 kPa,Stress distribution on Upper and lower electrodes and location max stress; material PDMS and Gold

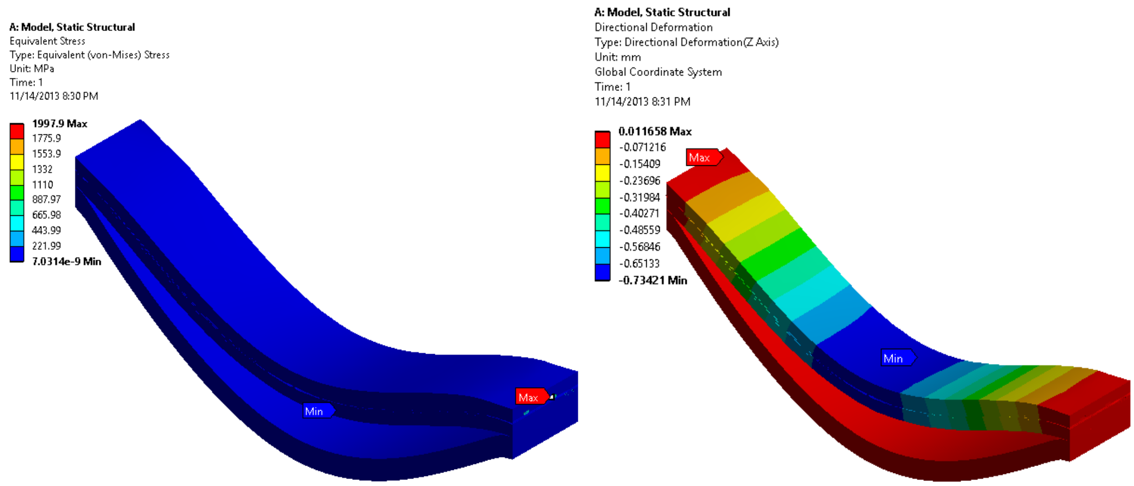

Figure 94: At 20KPa Equivalent (Von-mises) stress and z-directional deformation at any point in the structure at 20kPa pressure; material PDMS and Gold

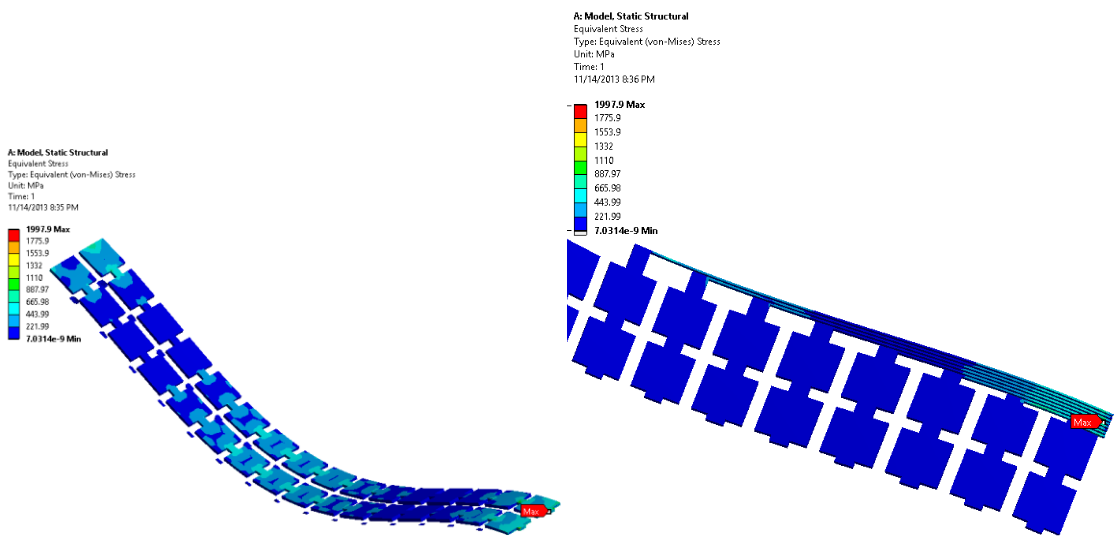

Figure 95: At 20 kPa ,Stress distribution on Upper and lower electrodes and location of max stress; material PDMS and Gold

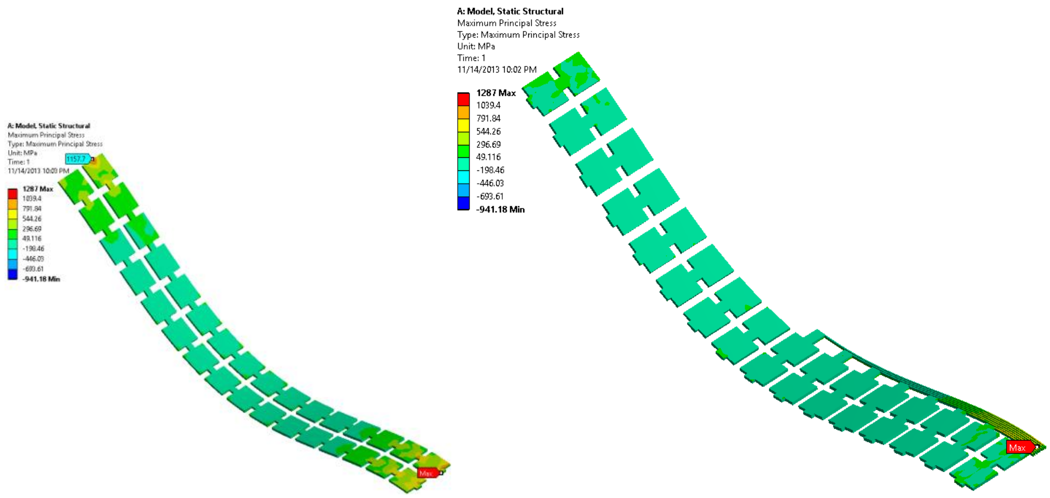

Figure 96: At 20 kPa ,Maximum Principal Stress on Upper and lower electrodes and location of max stress; material PDMS and Gold

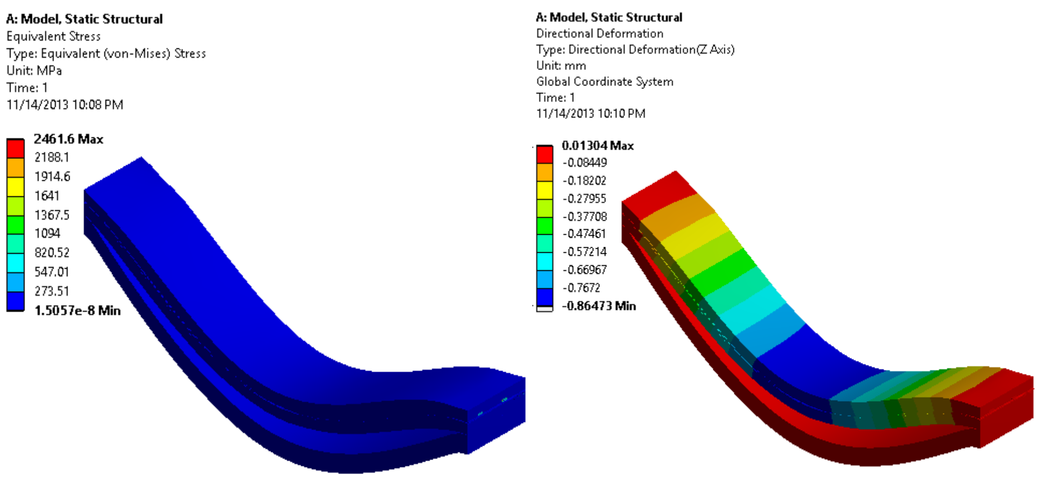

Figure 97: Equivalent (Von-mises) stress and directional deformation at any point in the structure at 25KPa pressure; material PDMS and Gold

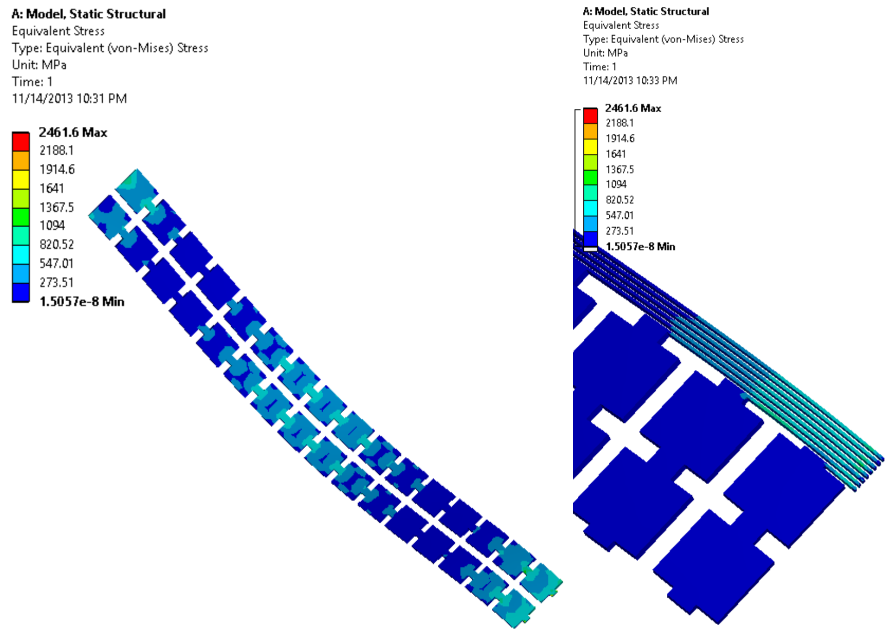

Figure 98: At 25 kPa ,Stress distribution on Upper and lower electrodes and location of max stress; material PDMS and Gold

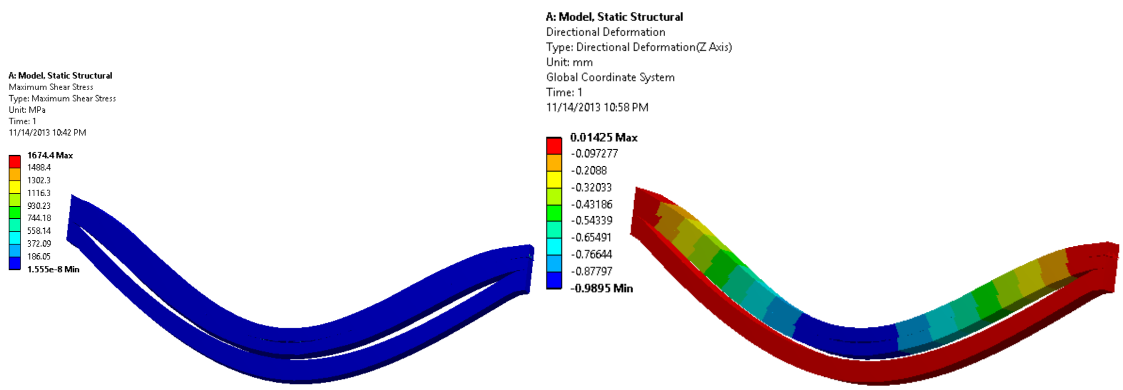

Figure 99: At 30 kPa pressure the sensor structure is in near contact with tibial support: material PDMS and Gold

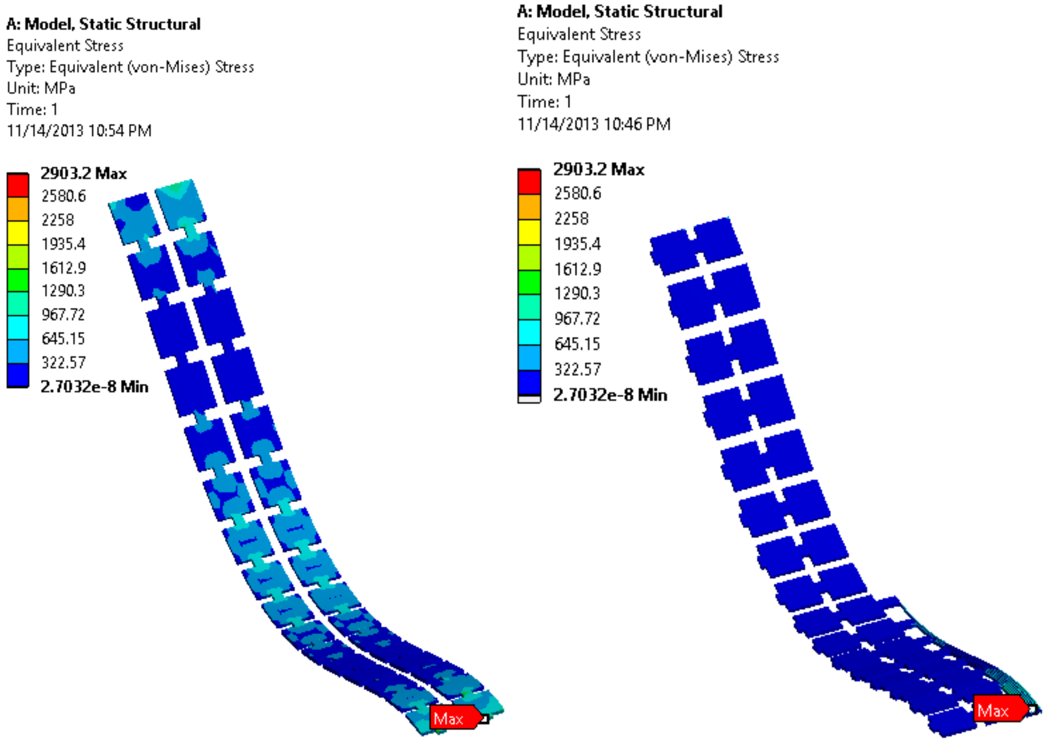

Figure 100: At 30 kPa ,Stress distribution on Upper and lower electrodes and location of maximum stress; material PDMS and Gold

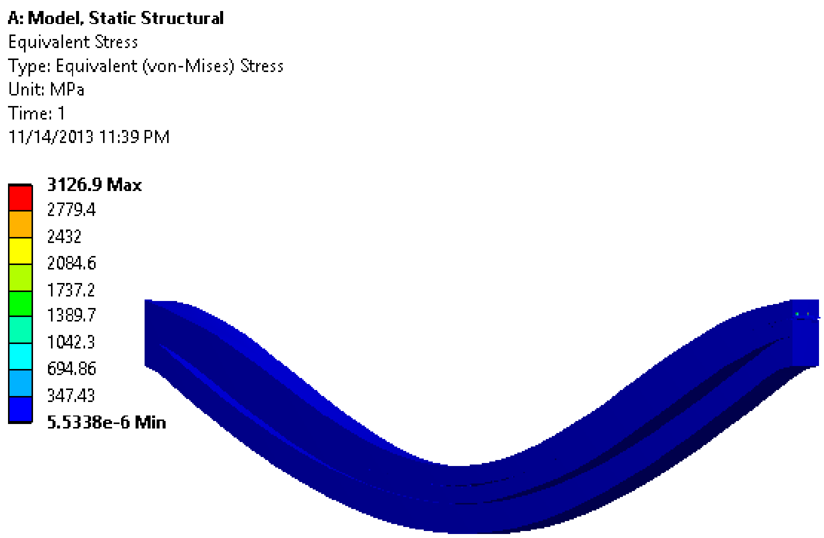

Figure 101: At 35 kPa , The sensor touches the tibial support ; material PDMS and Gold

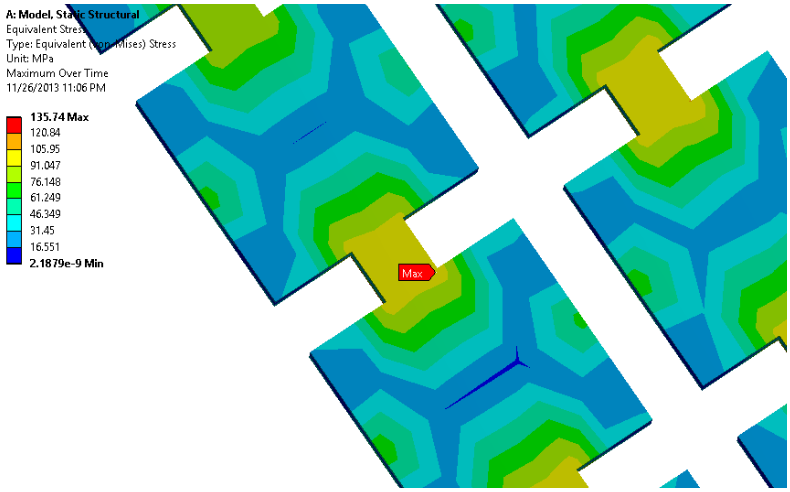

Figure 102: Location of Plastic deformation of Upper Gold electrodes at 2 kPa pressure with PDMS; electrodes thickness 20 microns

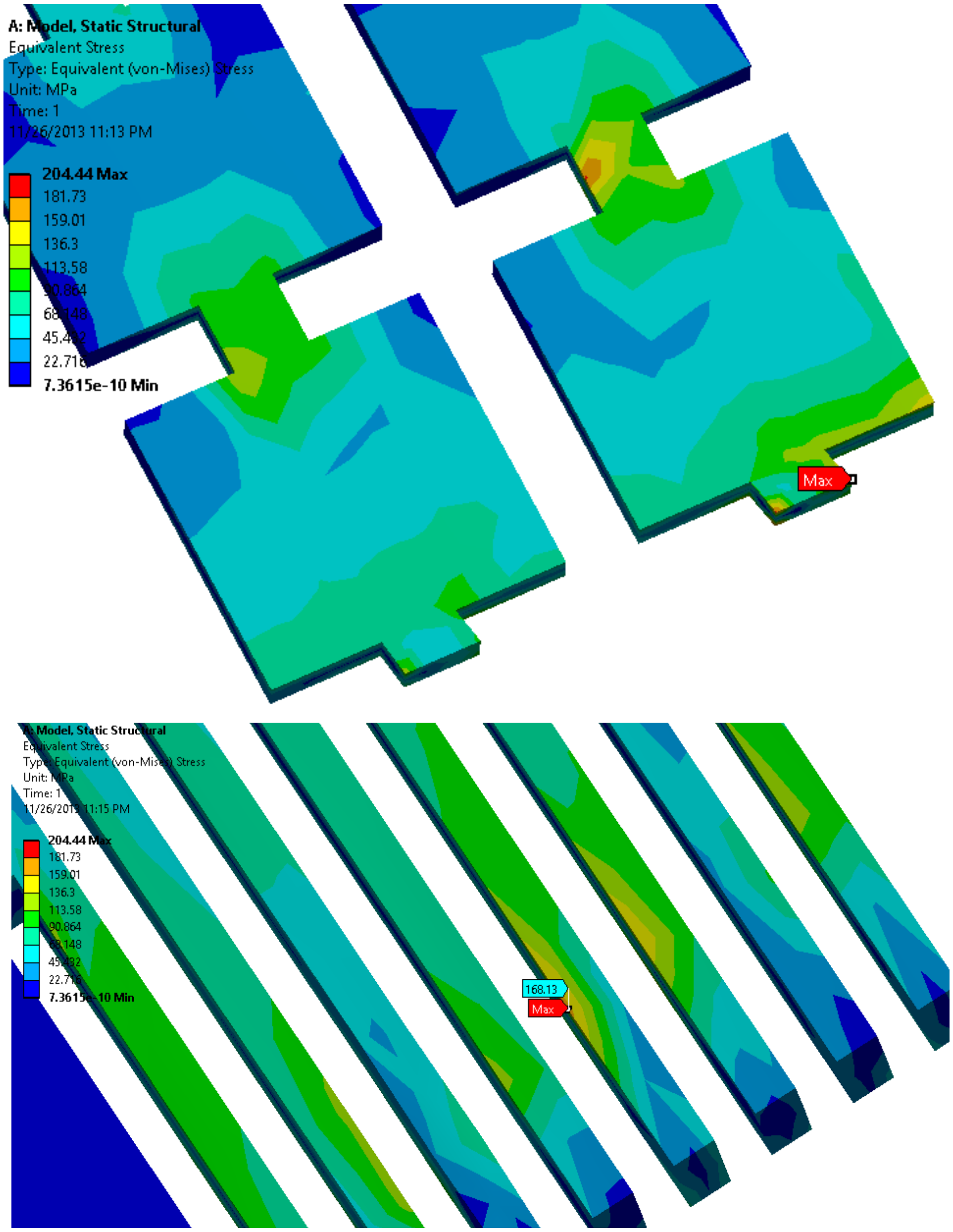

Figure 103: Location of Plastic deformation of Upper (left) and Lower (Right) Gold electrodes at 3 kPa pressure with PDMS; electrodes thickness 20 microns

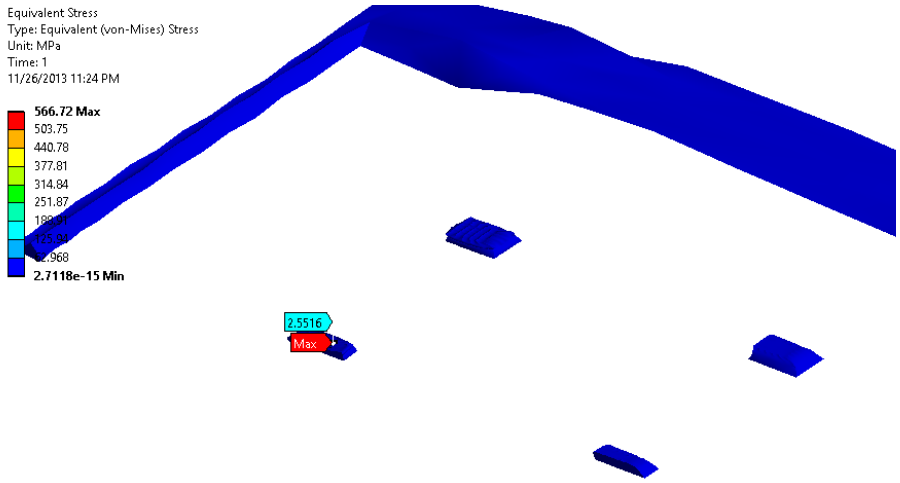

Figure 104: Location of the beginning of Plastic deformation of Bumps at 7 kPa pressure with PDMS and Gold; electrodes thickness 20 microns

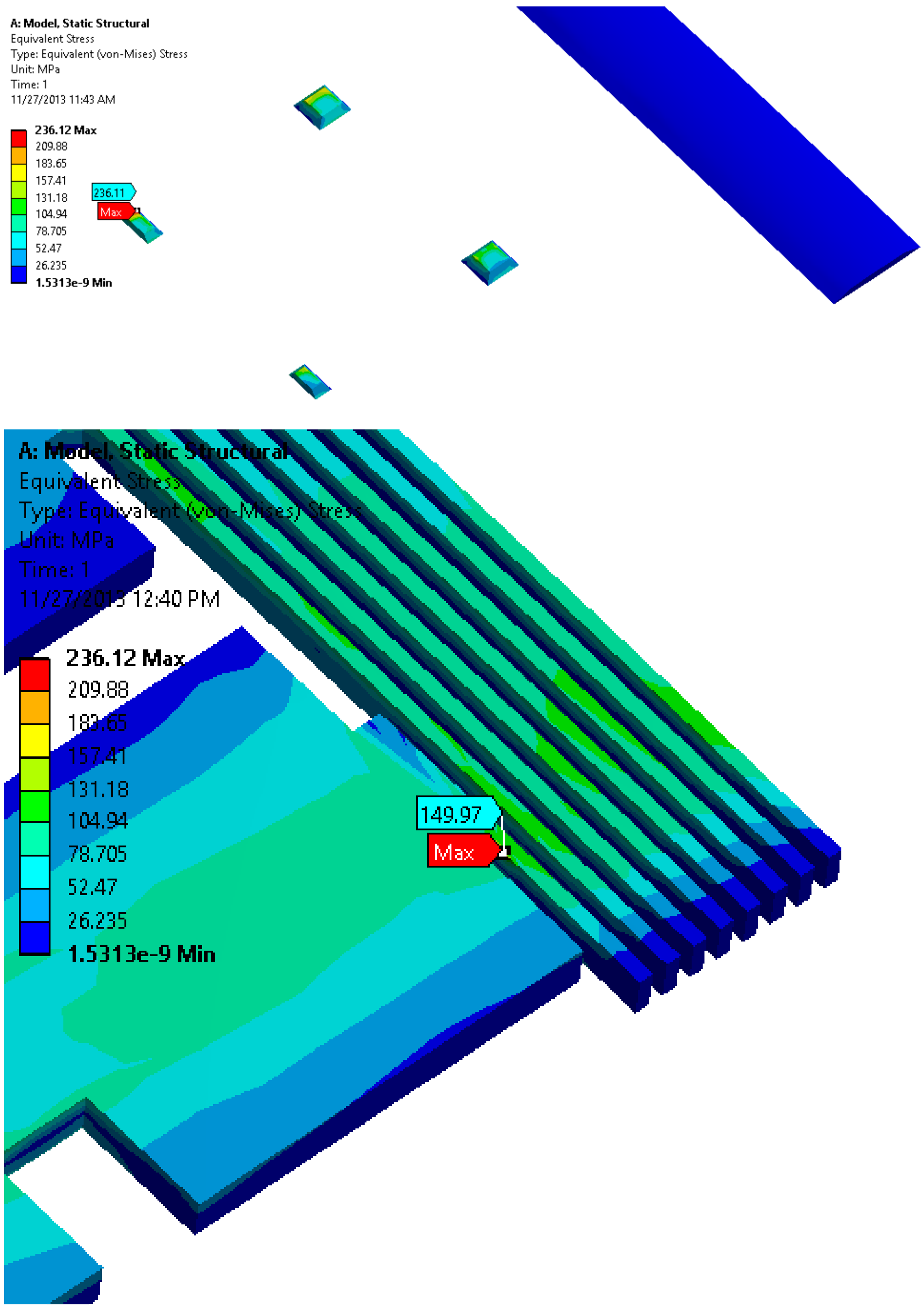

Figure 105: Location of the beginning of Plastic deformation of Bumps and lower electrodes at 140 kPa pressure with Polyimide and Gold; electrodes thickness 20 microns

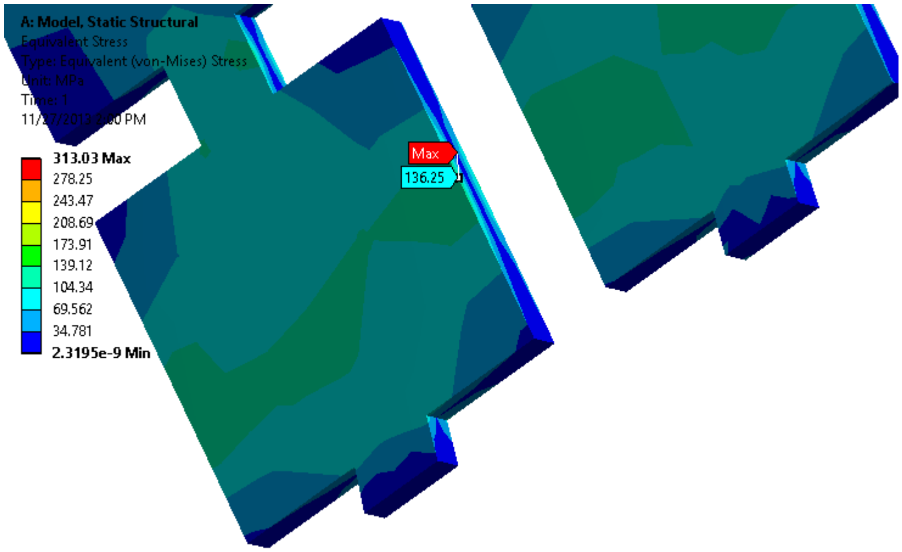

Figure 106: Location of the beginning of Plastic deformation of upper electrodes at 170 kPa pressure with Polyimide and Gold; electrodes thickness 20 microns

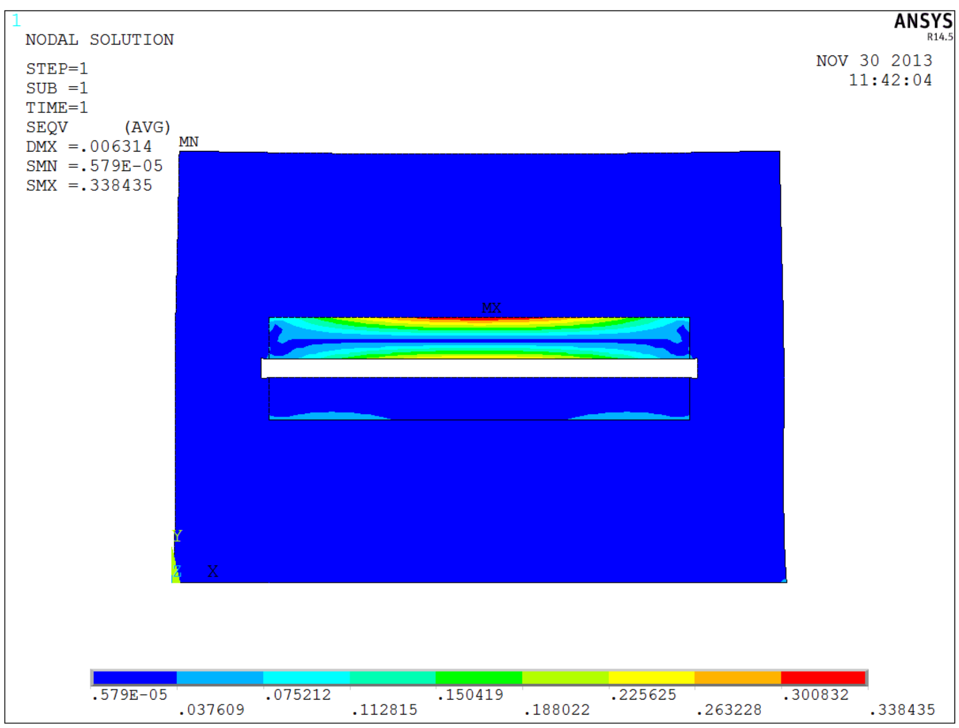

Figure 107: Max Equivalent Thermal Stress; Material:PDMS and Gold

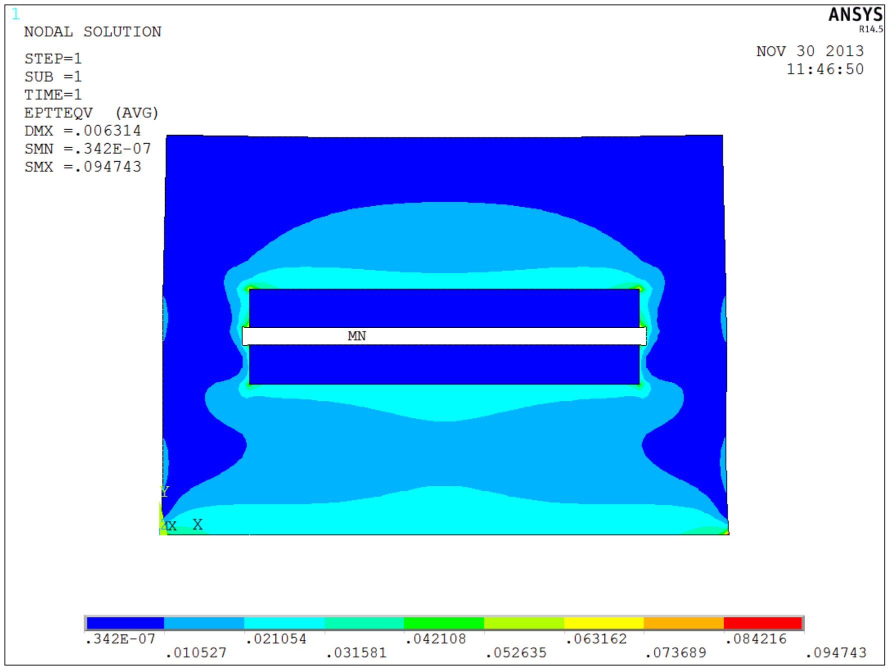

Figure 108: Maximum Equivalent Thermal and Mechanical Strain; Material: PDMS and Gold

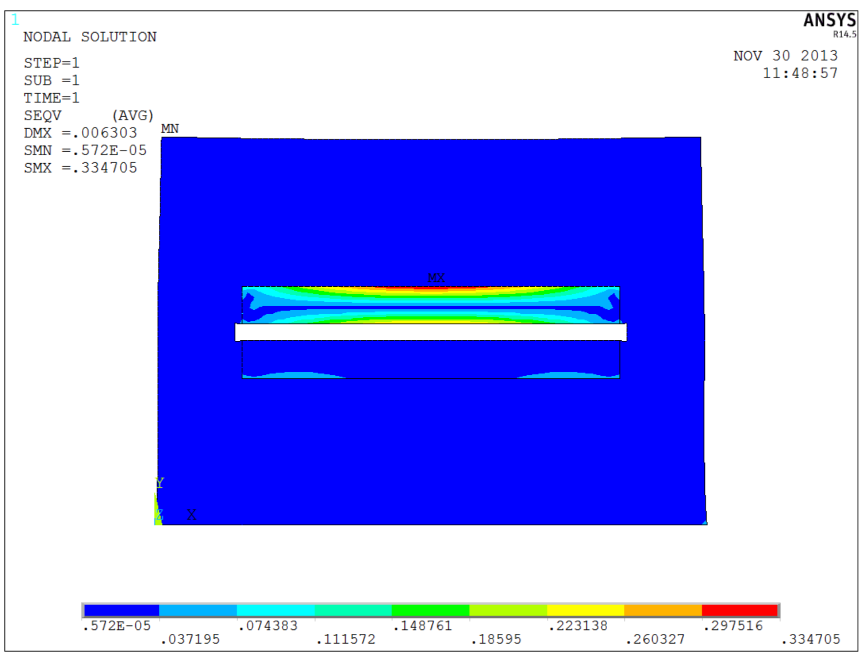

Figure 109: Max Equivalent Thermal Stress; Material: PDMS and Copper

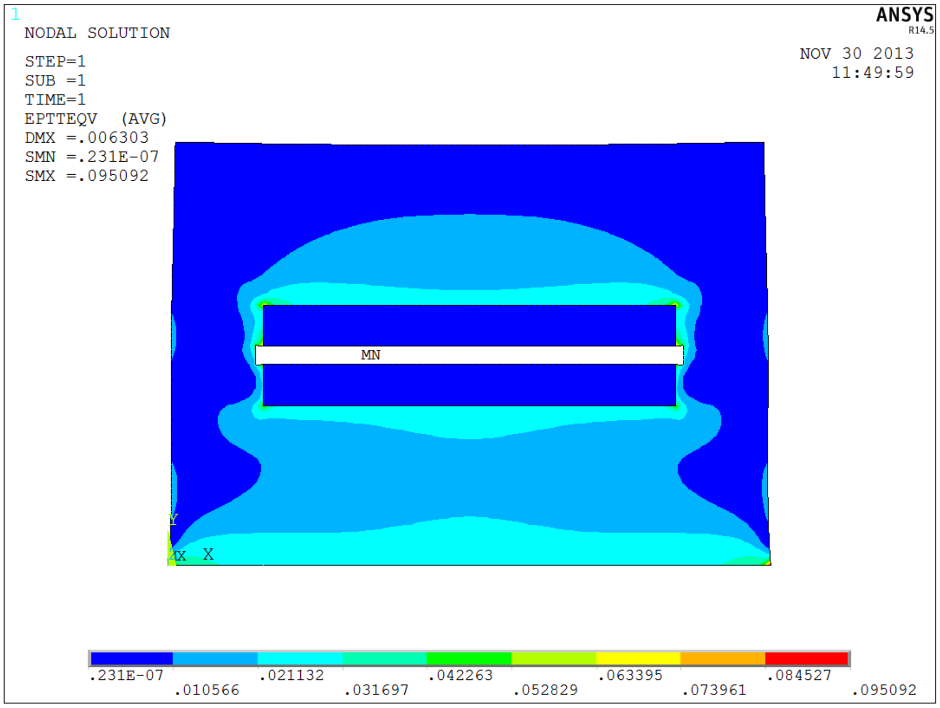

Figure 110: Maximum Equivalent Thermal and Mechanical Strain; Material: PDMS and Copper

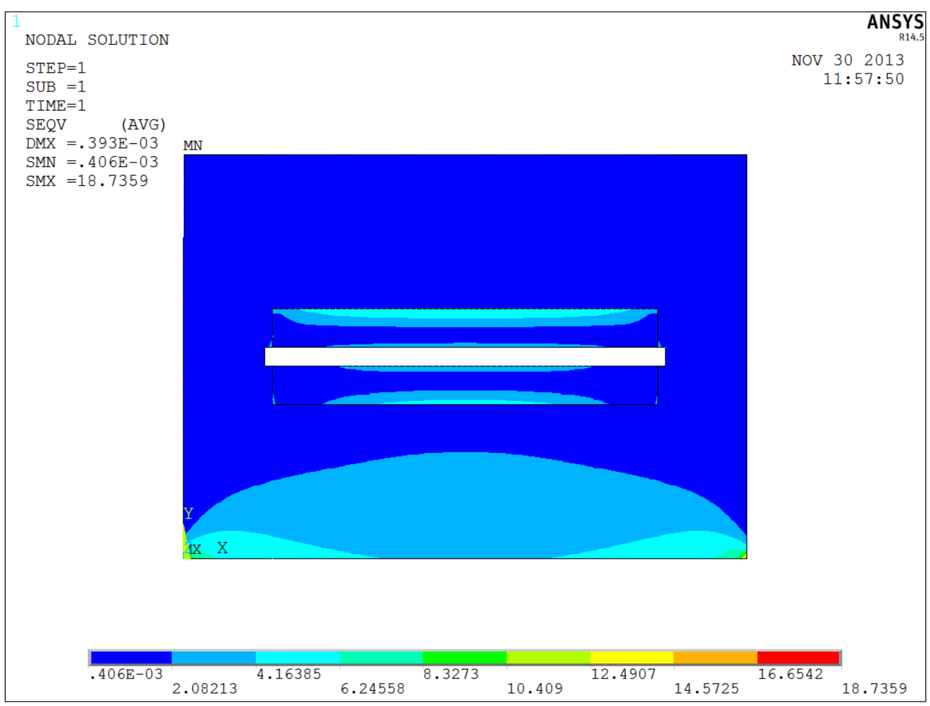

Figure 111: Max Equivalent Thermal Stress ; Material: Polyimide and Gold

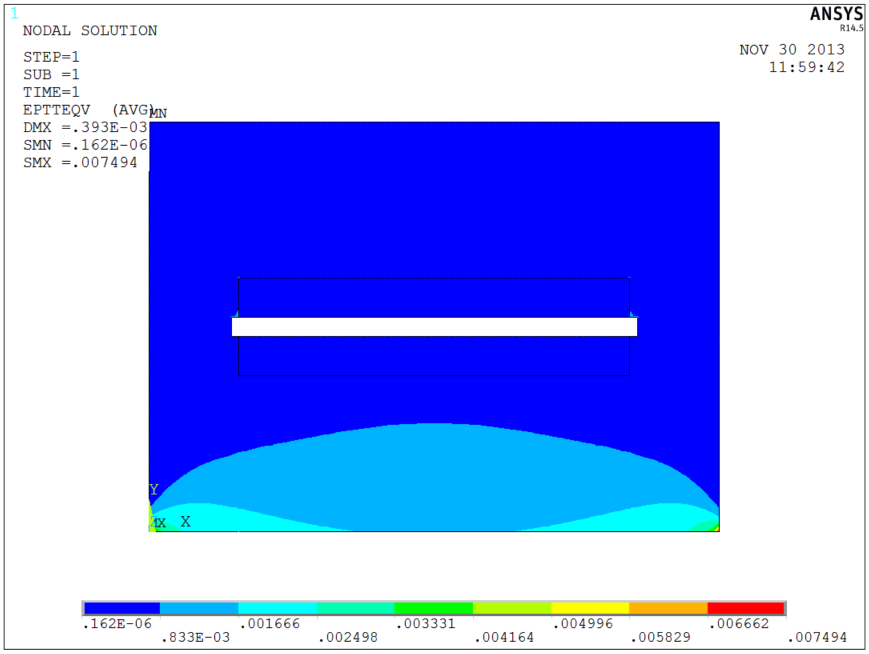

Figure 112: Maximum Equivalent Thermal and Mechanical Strain; Material: Polyimide and Gold

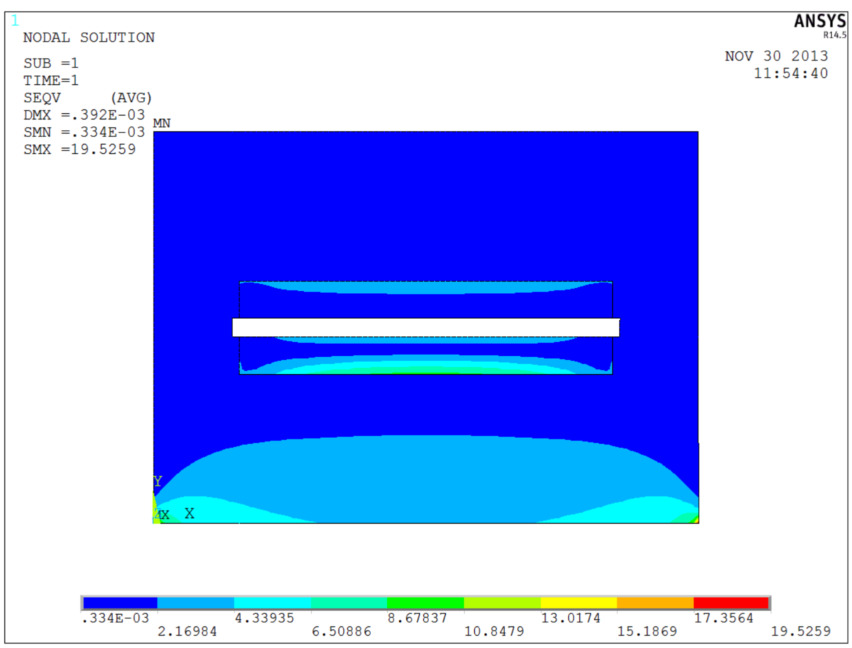

Figure 113: Max Equivalent Thermal Stress; Material: Polyimide and Copper

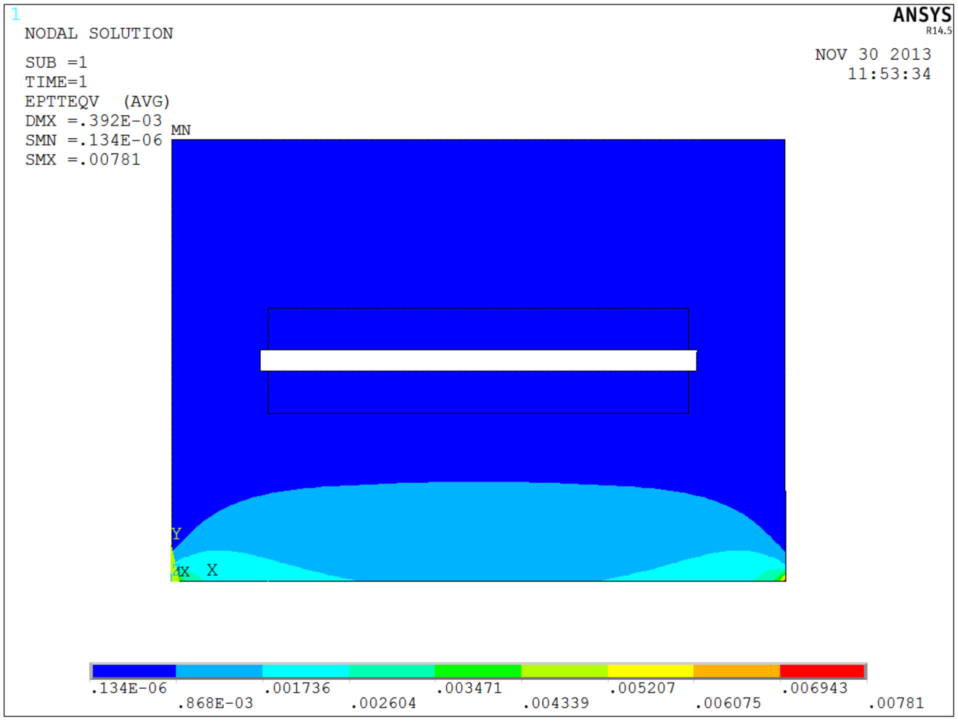

Figure 114: Maximum Equivalent Thermal and Mechanical Strain; Material: Polyimide and Copper

APPENDIX B:

ANSYS MECHANICAL APDL CODE

```
finish
/clear
/prep7
ET,1,182,,,0            ! Element Type 1 is 182 ;keyopt(3)=0 is defined as 'plane stress'
condition

MP,ex,1,7e-1            !defining PDMS properties
MP,NUXY,1,0.49999
MP,ALPX,1,310E-6        ! Coefficient of thermal extension for PDMS, 310
                        !MICRO_STRAIN/kELVIN

MP,ex,2,2500            !defining Polyimide properties
MP,NUXY,2,0.34
MP,ALPX,2,20E-6         ! Coefficient of thermal extension for Polyimide,20
                        !MICRO_STRAIN/kELVIN

MP,ex,3,7.9e4           !defining Gold Properties
MP,NUXY,3,0.42
MP,ALPX,3,14.2E-6       !Coefficient of thermal extension for Gold, 14.2
                        !MICRO_STRAIN/KELVIN

!!MP,ex,3,1.1e5                          !defining Copper Properties
!!MP,NUXY,3,0.34
!!MP,ALPX,3,17E-6                        !Coefficient of thermal extension for
                                         !Copper, 17 MICRO_STRAIN/KELVIN
!!Tensile Yield strength of PDMS is 2.24 MPa
!!gold yield strength is 127 Mpa
!!Copper yield strength is 252.3Mpa
!!Polyimide yield strength is 231Mpa (tensile) and 150 Mpa (compressive)
!!Creating Geometry
lepdms=0.292                             !length of pdms substrate 500 micron
leelec=0.2                               ! length of electrodes are 200 micron
welec=0.02                               ! width of electrodes 20 micron initial
bumpl=.042                  ! Bump Length is 42 micron
bumpw= 0.01                              ! Bump height 10 micron
wpdms=0.1                                ! width of upper and lower pdms is 100
micron
!!wgap=0.01                              ! air gap width 10 micron
!!wpoly=0.01                             ! pdms spacer thickness 10 micron
blc4,0,0,lepdms,wpdms                    ! lowerpdms
blc4,0,wpdms,bumpl,bumpw          ! left pillar
blc4,.046,wpdms-welec,0.2,welec          ! lower electrodes
blc4,0.25,wpdms,bumpl,bumpw              ! right pillar
!!!!!!!blc4,0,wpdms,lepdms,wgap           ! air gap
```

```
!!! Temporarily deactivating blc4,0,wpdms+wgap,lepdms,wpoly              !! Polyimide
!!!solid layer
blc4,0.046,wpdms+bumpw,0.2,welec          ! Upper electrodes
blc4,0,wpdms+bumpw,lepdms,wpdms           ! Upper pdms
blc4,0.042,wpdms,0.208,bumpw              ! Middle air gap
!!a,21,8,5,4
!!a,22,3,14,15
!!a,7,16,13,6


allsel,all
aovlap,all
aglue,all
aplot
allsel,all

sys_num=11
local,sys_num,0,0.042,,,,,90          !arbitrary reference number greater than
                                      !10 that's why sys_num=11
wpcsys,-1,sys_num
asbw,all,,delete
sys_num=sys_num+1          !increment numbering by 1 each time
local,sys_num,0,.046,,,,,90   !create new coordinate system (translated and rotated)
wpcsys,-1,sys_num          !define working plane at that new coordinate system
asbw,all,,delete           !divide areas along working plane (basically cutting
geometry at                !intersection with plane)
sys_num=sys_num+1
local,sys_num,0,.246,,,,,90
wpcsys,-1,sys_num
asbw,all,,delete

sys_num=sys_num+1
local,sys_num,0,.35,,,,,90
wpcsys,-1,sys_num
asbw,all,,delete
sys_num=sys_num+1
local,sys_num,0,0.25,,,,,90
wpcsys,-1,sys_num
asbw,all,,delete
sys_num=sys_num+1
local,sys_num,0,,wpdms-welec,,,90,
wpcsys,-1,sys_num
asbw,all,,delete
sys_num=sys_num+1
```

```
local,sys_num,0,,wpdms+bumpw+welec,,,90,
wpcsys,-1,sys_num
asbw,all,,delete
csys,0
wpcsys,-1,0
!!!!!!!!!!!!!!!!!!!!!!!!!!!!!!!!!!!!!!!!!!!!!!!!!!!!!!!!
!!!!!!!!!!!!!!!!!!!!!!!!!!!!!!!!!!!!!!!!!!!!!!!!!!!!!!!!
/pnum,line,0
/pnum,area,1
type,1
mshkey,1                        !!mapped meshing is turned on
mshape,0                        !Specifying element shape, triangular element


asel,s,area,,5
asel,a,area,,3
cm,electrodes,area              ! Groups Geometry Items into components
asel,s,area,,8
asel,a,area,,9
cm,bump,area
asel,s,area,,7
asel,a,area,,4
asel,a,area,,10
cm,airgap,area
allsel,all
asel,u,area,,airgap             !unselecting airgap and electrodes from all areas
asel,u,area,,electrodes

esize,0.003
mat,2                           ! Meshing with material type 2 (Polyimide) and 1
                                !(PDMS) alternatively
amesh,all                       ! Meshed all areas except airgap and electrodes
                                !with Element size 0.003mm or 3 micron
mshkey,1                        ! Mapped meshing turned on
mshape,0                        !use quad elements
esize,0.002
asel,s,area,,electrodes
mat,3                           ! Selected electrode material is Gold or copper
amesh,all
allsel,all
nsel,s,loc,y,0
d,all,ux,0                      ! Defining Boundary Conditions at the base
d,all,uy,0
!!allsel,all
```

```
!!nsel,s,loc,x,0
!!nsel,a,loc,x,lepdms
!!d,all,ux,0

!!et,2,targe169                    ! Element type 2 is a target element 169
!!et,3,conta171                    ! Element type 3 is a contact element 171
!!keyopt,3,12,0
!!allsel,all
!!lsel,s,loc,x,0.042,0.25
!!lsel,r,loc,y,wpdms
!!nsll,r,1
!!type,2
!!esurf,,                          !Generates elements overlaid on the free faces of
existing                           !selected elements
!!allsel,all
!!lsel,s,loc,x,0.042,0.25
!!lsel,r,loc,y,wpdms+bumpw
!!nsll,r,1                         !Selects those nodes associated with the selected
                                   !lines
!!type,3
!!esurf,,
finish
/SOLU
nlgeom,on
antype,static
outres,all
!nropt,full,,off
!neqit,100
nsel,all
allsel,all
TREF,100                  !Defines the reference temperature of thermal strain
                          !calculation
TUNIF,22                  !Assigns a uniform temperature to all nodes
allsel,all
solve
FINISH
/post1
```